Energetic Beam Processing of Silicon to Engineer Optoelectronically Active Defects

Thesis advisor: Professor Michael J. Aziz Daniel Recht

Energetic Beam Processing of Silicon to Engineer Optoelectronically Active Defects

Abstract

This thesis explores ways to use ion implantation and nanosecond pulsed laser melting, both energetic beam techniques, to engineer defects in silicon. These defects are chosen to facilitate the use of silicon in optoelectronic applications for which its indirect bandgap is not ideal. Chapter 2 develops a kinetic model for the use of point defects as luminescence centers for light-emitting diodes and demonstrates an experimental procedure capable of high-throughput screening of the electroluminescent properties of such defects. Chapter 3 discusses the dramatic change in optical absorption observed in silicon highly supersaturated (*i.e.*, hyperdoped) with the chalcogens sulfur, selenium, and tellurium and reports the first measurements of the optical absorption of such materials for photon energies greater than the bandgap of silicon. Chapter 4 examines the use of silicon hyperdoped with chalcogens in light detectors and concludes that while these devices display strong internal gain that is coupled to a particular type of surface defect, hyperdoping with chalcogens does not lead directly to measurable sub-bandgap photoconductivity. Chapter 5 considers the potential for silicon to serve as the active material in an intermediate-band solar cell and reports experimental progress on two proposed approaches for hyperdoping silicon for this application. The main results of this chapter are the use of native-oxide etching to control the surface evaporation rate of sulfur from silicon and the first synthesis of monocrystalline silicon hyperdoped with gold.

For three great mentors:
Paul Bianchi, Craig Arnold, and Michael Aziz.

Contents

Acknowledgments

Financial support for this thesis was provided by several sources. Portions of this work were funded by contracts with the US Army Armament Research Development and Engineering Center. The Nd:YAG laser was purchased using a Defense University Research Instrumentation Program grant. I was supported for three years by a National Defense Science and Engineering Graduate Fellowship.

Two large donations of substrate material made this thesis possible. Mitsutaka Takemura and Ken Kaufmann arranged for Hamamatsu to provide an uncut wafer of silicon photodiodes. Heyun "Henry" Yin of Varian Semiconductor supplied a set of 12-inch silicon wafers implanted with various doses of sulfur and selenium and worked closely with us to ensure that the implants met our specifications.

Work included in this thesis made use of a number of shared facilities. Device fabrication, ellipsometry, and most scanning electron microscopy were performed at the Harvard Center for Nanoscale Systems. Additional scanning electron microscopy

took place at the Australian National University Center for Advanced Microscopy and the University of Technology Sydney Microstructural Analysis Unit. Most secondary ion mass spectroscopy (SIMS) measurements were performed at the University of California Santa Barbara Materials Research Laboratory. A number of ion implanted samples were prepared in the Australian National University Department of Electronic and Materials Engineering Ion Implantation Facility. Additional samples of silicon implanted with gold were prepared at the College of Nanoscale Science and Engineering at the State University of New York Albany.

I am thankful for the contributions of my many talented collaborators.

At the Australian National University: Supakit Charnvanichborikan supplied a number of ion implants and worked side-by-side with me on light emitting diode (LED) measurements, Rutherford backscattering (RBS), and metal implantation during my six weeks at ANU; Patrick Parkinson performed several additional rounds of LED measurements; Daniel Pyke provided assistance with the RBS system and my social life in Canberra; Jennifer Wong-Leung offered important suggestions for the characterization of surface defects in photodiodes; Frank Brink assisted me in the ANU Electron Microscopy Unit; and Professor Jim Wiliams provided financial support for my visit to Australia and was a source of invaluable ion-beam expertise throughout my Ph.D.

At the Massachusetts Institute of Technology: Mark Winkler and Joe Sullivan were my closest collaborators throughout my work on hyperdoping and provided more intellectual and experimental contributions than can easily be listed here; Christie Simmons offered useful discussions of my work on silicon as an intermediate band material; Bonna Newman was an early advocate for collaboration between the Aziz and Buonassisi groups; Professor Tonio Buonassisi served on my thesis committee, opened his lab to me as if I

were one of his students, and was a source of guidance and experimental inspiration for both the entire collaboration and me in particular; Matt Smith of Professor Silvija Gradecak's group prepared and imaged a staggering number of cross-section transmission electron microscopy samples as part of the transition metals experiment; Elif Ertekin of Professor Jeffrey Grossman's group performed careful and provocative density functional theory calculations.

At the National Renewable Energy Laboratory: Robert Reedy performed SIMS measurements for the evaporation experiment.

At the Rensselaer Polytechnic Institute: Dave Hutchinson built the apparatus for and contributed extensively to measurements of external quantum efficiency (EQE), photoconductivity, and light beam induced current (LBIC); Thomas Cruson collected substantial amounts of the microwave photoconductivity data; Andrew McAllister performed modeling work critical to interpreting the microwave measurements; The many REU students of the Persans group contributed early EQE and LBIC measurements; Professor Peter Persans frequently hosted me in his lab and provided useful advice throughout my Ph.D.

At SiOnyx: Jim Carey and Martin Pralle suggested device fabrication and characterization strategies.

At the University of California Santa Barbara: Tom Mates performed SIMS measurements for several experiments and trained me in the use of the SIMS system he maintains.

At the University of Technology Sydney: Mark Lockrey and Professor Matthew Phillips hosted me for an important day of electron beam induced current measurements.

At the US Army ARDEC Benet Labs: Jeff Warrender arranged financial support for this project, coordinated the New York arm of the collaboration, and provided substrate ma-

terials and advice throughout my Ph.D; Jay Matthews assisted with the Nd:YAG melting of silicon implanted with gold.

At Harvard: Taeseok Kim trained me to use the Aziz group's laser melting setup; Aurore Said produced a vast collection of hyperdoped silicon photodiodes during her Fulbright year in our lab; Athena Pan performed transmission and ellipsometry measurements of silicon on insulator samples; Edy Cardona and Shauna Gordon-Mckeon worked with me to automate the melting apparatus; Alex Ratner helped me clean the lab for the first time in more than five years and worked with me to get the laser melting system running after six months of down time; Brandon Piercy assisted with early characterization of the Nd:YAG laser; Ikurou Umezu and Atsushi Kohno taught me the fundamentals of optical property measurements of hyperdoped materials; Jing Yang performed some early silicon on insulator thinning experiments; Jiming Bao showed me how to fabricate and characterize an LED; Professor Federico Capasso helped supervise the luminescence work; Jacob Krich provided theoretical guidance on the physics of intermediate band materials. Renee Sher and Yu-Ting Lin kept me up to date on their own laser material processing efforts; Professor Eric Mazur served on my thesis committee and offered useful advice on several occasions; and, last but not least, Professor Michael Aziz was my Ph.D advisor for which I cannot thank him enough.

I AM DEEPLY GRATEFUL FOR THE SUPPORT OF MY FAMILY, FRIENDS, AND COWORKERS. Although acknowledging everyone who has provided moral or practical support for this thesis would take longer than reporting its scientific results, I would like to highlight a few indiviudals who made particularly important contributions. My fellow students in the Aziz group— Taeseok Kim, Charbel Madi, Jason Rugolo, Brian Huskinson, and Joy Perkinson— were always ready with ideas, tools, and good cheer. Barbara Sewall

kept our research group running in the face of constant confusion. Raji Shankar was my partner for a microphotoluminescece experiment that was incredibly educational even though it did not happen to produce a publishable result. Dexter Eames repaired the excimer laser control board. Emma Shoucair proofread the final manuscript of this thesis. Kate Jensen was everything I could have hoped for in a roommate, officemate, sounding board, problem set buddy, designated spatial reasoner, and friend. My parents parented superlatively even when I made doing so challenging and my sister assisted me with graphic design on several occasions. Finally, Emily Eames agreed to marry me and then kept me fed and sane during the writing of this thesis.

List of Figures

List of Tables

1

Introduction

Silicon is an indirect-bandgap semiconductor; the maximum energy point of its valence band occurs at a different momentum from the minimum energy point of its conduction band. An important consequence of this is that in order for an electron to transition from the valence band maximum to the conduction band minimum or vice versa, a phonon must be emitted or absorbed. The fact that an extra particle, the phonon, is required for these transitions reduces their probability relative to those, such as the equivalent excitation in direct bandgap semiconductors, that require

only an electron to occur.

Two technologically important applications for inter-band transitions are light emission via radiative recombination of conduction band electrons and valence band holes and photocarrier generation via light absorption by valence band electrons that are optically excited into the conduction band. Having an indirect bandgap means that silicon is not an ideal material for either of these uses. Silicon light detectors and solar cells must be roughly 100 times thicker than their direct-gap counterparts to absorb the same amount of light. Similarly, whereas gallium arsenide and other direct-gap semiconductors can be readily made into commercial-quality light emitting diodes using inter-band radiative recombination, bandgap luminescence in silicon is so weak as to be detectable only by sensitive instruments.

Nevertheless, the numerous advantages of silicon— it is low cost, earth abundant, and non-toxic; it is the focus of the extensive and continuously improving infrastructure of the microelectronics industry; and it is by far the most extensively studied and well-understood semiconductor material— make it worth considering even in applications for which it would not otherwise be ideal. Indeed, despite its indirect bandgap, silicon is the dominant semiconductor used by the solar photovoltaics industry. There is thus a tension in the study of materials for optoelectronic applications between discovering and improving direct-gap materials and finding ways to coax the desired performance out of silicon. Declarations that the days of silicon as the leading material in a particular field are numbered have been common for more than a decade [1–3]. Yet despite the failure of these dire early predictions, it is not at all certain what the future will hold.

The fundamental motivation for this thesis is that the advantages of silicon are too great to ignore even in optoelectronic applications for which its properties are not ideal. With that as a premise, this thesis presents an exploration of how carefully chosen defects

introduced in controlled quantities can be used to engineer the optoelectronic properties of silicon in order to overcome its limitations as an indirect-gap semiconductor without sacrificing its other advantages. The key tools used for producing these defects are energetic (*i.e.*, ion and laser) beams, a choice made because of the ability of such techniques to process large areas of material at high speed and relatively low cost while creating far-from-equilibrium structures and compositions. This thesis is organized as follows.

Chapter 2 considers silicon as a light emitting material. It presents a theoretical and experimental exploration of the use of point defects as luminescence centers in silicon. Section 2.1 describes a kinetic model of luminescence by neutral point defects in silicon, which yields design criteria for devices exploiting such luminescence. Section 2.2 outlines a new experimental procedure for rapidly screening the electroluminescence of potentially interesting point defects and, as a proof of concept, demonstrates this procedure using the well-known W-line luminescent defect. It is hoped that this chapter will lay the ground work for future high-throughput studies of point-defect luminescence in silicon.

Chapter 3 considers silicon as a light absorbing material. It begins a discussion, lasting for the remainder of this thesis, of single-crystal silicon doped to high supersaturations (*i.e.*, hyperdoped) with non-traditional dopants. Section 3.1 surveys the history of silicon hyperdoped with the chalcogens sulfur, selenium, and tellurium, as a class of materials capable of strongly absorbing photons with energies less than the bandgap of silicon. It begins with the discovery of black silicon and proceeds to the initial production of flat, monocrystalline silicon hyperdoped with sulfur by ion implantation followed by nanosecond pulsed laser melting. Section 3.2 details the standard experimental procedure used by the Aziz group (and thus in this thesis) to produce single-crystal hy-

perdoped silicon. Section 3.3 reports the first measurement of the optical properties of silicon hyperdoped with sulfur, selenium, or tellurium for photon energies above the band gap of silicon.

Chapter 4 considers silicon as a light detecting material. Section 4.1 reports internal gain (multiple electrons collected per incident photon) and a somewhat extended response spectrum in photodiodes made from silicon hyperdoped with sulfur and selenium. Section 4.2 describes an experiment using photoinduced changes in microwave reflectivity to probe whether the sub-bandgap absorption of silicon hypderdoped with sulfur or selenium leads to photocarrier generation. This experiment also yields an upper bound on the carrier lifetime in these materials. Section 4.3 explores the mechanism by which the photodiode performance discussed in Section 4.1 occurs and concludes that surface structure is necessary for gain.

Chapter 5 moves beyond the simple distinction between direct and indirect-gap semiconductors and considers silicon as a potential intermediate band photovoltaic material. Section 5.1 summarizes collaborators' investigations into the band structure of silicon hyperdoped with chalcogens. This section concludes by detailing two potential strategies for turning silicon into a useful intermediate band material: co-doping silicon with a chalcogen and an acceptor and hyperdoping silicon with a single element that induces both a filled state and an empty state near mid-gap. In pursuit of the first strategy, Section 5.2 demonstrates the use of native oxide etching to modulate the rate of surface evaporation of sulfur during pulsed laser melting. This technique allows both the creation of buried hyperdoped layers and fine control of the concentration depth and lateral profiles of sulfur in silicon. Section 5.3 reports the first major experimental step toward the second strategy: an attempt to create single-crystal silicon hyperdoped with each of nine different transition metals. Although this study found that hyperdoping silicon

with transition metals is substantially more challenging than working with traditional dopants or chalcogens, this section concludes with the fabrication of monocrystalline silicon containing gold, a particularly promising element for the creation of an intermediate band in silicon, at a concentration of 10^{19} /cm^3.

2

Point-defect luminescence: a potential route to room-temperature silicon light emitting diodes

Because of its indirect bandgap, bulk silicon cannot be used as the active material of efficient, room-temperature light emitting diodes (LEDs) or lasers. Despite this, the potential cost and scale benefits to developing an all-silicon light source makes the search for such a device an active area of research [4]. An efficient silicon LED would find immediate application in optical computing, telecommunications, and medical devices. An efficient silicon laser could revolutionize any or all of those fields.

One approach to producing such a device is to use point defects as light emission centers [5–7]. Recently, light emitting diodes (LEDs) have been produced using two different zero-phonon emission lines originating at point defects: the W line at 1.018 eV and the G line at 969 meV. The G line arises from the presence of carbon in silicon [6,7], the W line from a small self-interstitial complex [5,8].

Point-defect luminescence devices are not yet practical because a point defect capable of efficient room temperature light emission has not been identified. In the case of the W and G line defects, the intensity of emitted light decreases to a small fraction of its maximum value as the temperature is raised from 4 to 77 K and is undetectable at room temperature [5,6,8]. This chapter describes the development of an approach, combining experiment and theory, that could lead to a device that overcomes this challenge.

2.1 A model of point-defect-mediated luminescence

In order to search effectively for a point defect suitable for room temperature device operation, one must first establish a set of physically motivated criteria that such a defect should satisfy. Successfully defining such criteria requires a detailed model of point-defect luminescence. Previous to this work, the leading phenomenological model of the temperature dependence of point-defect luminescence in silicon was developed by Davies *et al.* to describe G line photoluminescence [9]. This model is not based on specific physical mechanisms; it relies on two unknown energies: an unspecified trap level and an energy barrier for a general non-radiative process [9]. While this model was able to fit experimental observations, it does not provide a rich enough picture of point-defect luminescence to allow for the comparison of candidate defects. This section builds on the work of Davies *et al.* by describing observations of G and W line luminescence using familiar concepts from semiconductor physics. Employing this approach is

an initial step toward addressing questions of defect selection and materials design for point-defect luminescence in silicon.

Previous experiments have suggested that G line luminescence is due to a two energy level system whose upper level is slightly below the conduction band [9]. These levels likely arise from bound exciton formation at the neutral carbon complex responsible for the G line. Because the data are qualitatively similar, we hypothesize that the same is true of the neutral self-interstitial complex responsible for the W line. A neutral point defect capable of binding excitons can be in one of three states[1]: it can have no carriers bound to it, one bound carrier (in which case it is charged), or two bound carriers of opposite sign (a bound exciton). These will be referred to as states 0, 1, and 2 respectively. It must be true that

$$n_D = n_0 + n_1 + n_2 \tag{2.1}$$

where n_D is the total concentration of defects and n_0, n_1, and n_2 are the concentrations of defects in states 0, 1, and 2. The defect is capable of transitioning between any pair of these states. It is thus possible to define transition rates between the three states per unit volume such as R_{20} for the transition from state 2 to state 0 (*e.g.*, by radiative recombination). The intensity of luminescence will be proportional to n_2 and thus the goal of this model is to determine n_2 as a function of temperature. Under steady state conditions n_0 , n_1 , and n_2 must be constant. For n_2 this implies that $R_{02} + R_{12} = R_{20} + R_{21}$. Similar consideration of n_0 and n_1 yields a total of two independent equations.

Table 2.1 lists all the physical processes that can occur in this system and ties each of them to one of the transition rates. Several processes are ignored based on the following assumptions. 1) The concentration of free excitons is negligible compared to the

[1]This assumes that the defect binds carriers in a definite order, *e.g.* a hole and then an electron.

Rate	Process	Δn_0	Δn_1	Δn_2	$\Delta n_{\text{free } e^-}$	$\Delta n_{\text{free } h^+}$	$\Delta n_{\text{free exciton}}$	In model? (Reason neglected)
R_{01}	h^+ capture	-1	+1	0	0	-1	0	Yes
R_{01}	Bound h^+ / free e^- generation	-1	+1	0	+1	0	0	No (3)
R_{12}	e^- capture	0	-1	+1	-1	0	0	Yes
R_{12}	Bound e^- / free h^+ generation	0	-1	+1	0	+1	0	No (3)
R_{02}	Free exciton capture	-1	0	+1	0	0	-1	No (1)
R_{02}	Bound exciton generation	-1	0	+1	0	0	0	No(3)
R_{10}	h^+ emission	+1	-1	0	0	+1	0	Yes
R_{10}	Bound h^+ / free e^- recombination	+1	-1	0	-1	0	0	No(2)
R_{21}	e^- emission	0	+1	-1	+1	0	0	Yes
R_{21}	Bound e^- / free h^+ recombination	0	+1	-1	0	-1	0	No(2)
R_{20}	Non-radiative bound exciton recombination	+1	0	-1	0	0	0	Yes
R_{20}	Radiative bound exciton recombination	+1	0	-1	0	0	0	Yes
R_{20}	Bound exciton emission	+1	0	-1	0	0	+1	Yes

Table 2.1: Physical processes contributing to each transition rate, associated changes in concentrations of all species, and inclusion/neglect of process in the model. For clarity in this table it is assumed that the defect captures a hole and then an electron even though the model makes no distinction. Processes listed as not in the model are excluded based on the three numbered assumptions given in the text.

concentration of free carriers. This is reasonable because the purpose of the model is to describe an electrically or optically pumped device. 2) The rate of recombination of a bound carrier with a free carrier is small relative to the rates of capture and emission of free carriers. This assumption reflects the notion that a localized state and a delocalized state have a small interaction probability. Finally, 3) pair generation processes localized at a defect can be ignored. In the case of electrical pumping this is a modest assumption because the only carrier generation is thermal and so all pair generation events can be neglected relative to the electrical pumping. For optical pumping, this assumption is essentially equivalent to stating that the rate at which pump photons generate carriers at the luminescent defects is small relative to the rate at which the defects capture free carriers.

Assumption 1) means that it is not necessary to track the number of free excitons. Similarly, if the concentration of defects is small relative to the concentrations of free electrons and free holes, applying charge neutrality[2] allows for free carriers to be removed from the bookkeeping according to

$$n_{\text{freee}-} \approx n_{\text{freeh}+} \equiv n_c \tag{2.2}$$

which is independent of temperature and of the concentrations of other species and is controlled independently by the experimenter using the pump intensity. Consequently, n_0 , n_1 , and n_2 are the only temperature-dependent concentrations in this model. Under these assumptions and assuming linear kinetics, Table 2.1 translates into the following equations:

$$\begin{aligned} R_{01} = n_0 n_c c_{01}; \quad R_{12} = n_1 n_c c_{12}; \quad R_{02} \approx 0; \\ R_{10} = n_1 e_{10}; \quad R_{21} = n_2 e_{21}; \quad R_{20} = n_2 e_{20} \end{aligned} \tag{2.3}$$

[2]This is consistent with electrically or optically pumped luminescence and an undoped active region.

where the c_{ij}'s and e_{ij}'s are capture and emission coefficients respectively. Detailed balance (see, *e.g.*, Reference 10) eliminates the emission coefficients according to

$$e_{10} = c_{01} n_0^* n_c^* / n_1^* = c_{01} K_{01} \tag{2.4}$$

and

$$e_{21} = c_{12} n_1^* n_c^* / n_2^* = c_{12} K_{12} \,, \tag{2.5}$$

where * denotes an equilibrium value and the K_{ij}'s are calculable equilibrium constants for their respective processes. Making these substitutions and solving the steady-state problem for n_2 yields

$$n_2 = \frac{\beta n_D n_C^2}{\beta(K_{01}K_{12} + K_{12}n_C + n_C^2) + \alpha(K_{01} + n_C) + \alpha\beta n_C} \tag{2.6}$$

in which $\alpha \equiv e_{20}/c_{01}$ and $\beta \equiv c_{12}/c_{01}$ are fitting parameters with units of concentration and no units respectively. Assuming that the defect always binds a hole from the valence band (set to $E = 0$) and then an electron from the conduction band[3], Equation 2.6 becomes

$$n_2 = \frac{\beta n_D n_c^2}{\beta\left(\frac{N_V}{g_h}\frac{N_C}{g_e} e^{(E_e - E_h - E_g)/k_B T} + n_c \frac{N_C}{g_e} e^{(E_e - E_g)/k_B T} + n_c^2\right) + \alpha\left(\frac{N_V}{g_h} e^{-E_h/k_B T} + n_c\right) + \alpha\beta n_c} \tag{2.7}$$

where N_C and N_V are the conduction and valence band effective densities of states ($\propto T^{\frac{3}{2}}$), g_h and g_e are the hole and electron degeneracy factors, E_g is the bandgap, and E_h and $E_g - E_e$ are the hole and electron binding energies such that $E_e - E_h$ is the energy of the emitted photons.

[3]To consider the opposite case, interchange $\frac{N_C}{g_e} e^{(E_e - E_g)/k_B T}$ and $\frac{N_V}{g_h} e^{-E_h/k_B T}$ in Eq. 2.7.

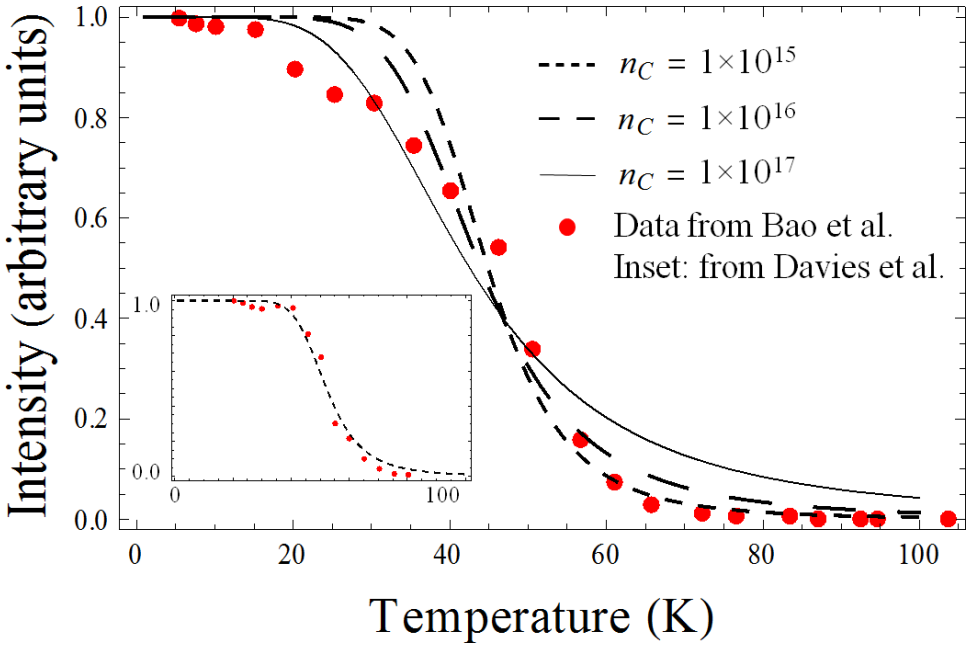

Figure 2.1: Main figure: Plot of a least-squares fit of the model to the W line electroluminescence data in Reference 5 for three assumed carrier concentrations: 10^{15}, 10^{16}, and 10^{17} /cm^2. The temperature dependences of the fitting parameters and bandgap were ignored. Inset: Plot of a least-squares fit of the model to the G line photoluminescence data in Reference 9 for an assumed carrier concentration of 10^{15} /cm^2. Data for temperatures below 20 K were disregarded because they reflect an additional trap level not described in this model (see Reference 9).

n_c (cm^{-3})	G line E_e (eV)	W line E_e (eV)
10^{15}	1.138	1.144
10^{16}	N/A	1.153
10^{17}	N/A	1.162

Table 2.2: Trap energy calculated from a least squares fit of the model to the data in References 9 and 5 assuming the stated values for n_c.

Dividing Equation 2.7 by n_D provides a functional form for the temperature dependence that can be compared with and fit to photo- and electroluminescence intensity data. The main portion of Figure 2.1 shows three least-squares fits (for three different carrier concentrations) of this model to the data of Bao *et al.* for the temperature dependence of electroluminescence intensity from a W line light emitting diode (LED) [5]. The inset shows a least squares fit to the data of Davies *et al.* for the temperature dependence of G line photoluminescence intensity for an assumed carrier concentration of $10^{15}/cm^3$ [9]. This data series is truncated below 20 K to exclude points influenced by a trap state not contained in this model. Both sets of data have been normalized to a maximum of unity. All fits ignore the temperature dependences of a, β, n_c and the bandgap of silicon. a, β, and n_c and are considered constants to prevent a proliferation of fitting parameters. The bandgap is set to its low-temperature value of 1.17 eV: including its temperature dependence would represent false precision because the (unknown) temperature dependence of the defect levels is neglected. $E_e - E_h$ is taken to be 1.02 eV for the W line and 0.969 eV for the G line. Finally, the silicon samples in both references are assumed to be undoped. This is accurate for Reference 9 but the active region of the W line LED in Reference 5 was lightly p-doped to a resistivity of 5 Ω-cm [5, 9]. This resistivity corresponds to a boron concentration of roughly $3 \times 10^{15}/cm^3$, which is on the order of the smallest carrier concentration assumed in fitting the W line data [5].

The model presented above provides an accurate fit to the G line data from Reference 9 and a reasonable fit to the W line data in Reference 5. In the latter case higher carrier concentrations produce a better fit at low temperatures and lower carrier concentrations produce a better fit at high temperatures. This could be a consequence of one or more of the temperature dependences ignored in this calculation. The results of fitting were highly insensitive to variations of several orders of magnitude in the values of α and β. Table 2.2 reports the values of E_e computed by the least-squares fits. For both defects it is evident that one carrier, assumed by Equation 2.7 to be an electron, is bound much more loosely than the other. The result for the G line is in quantitative agreement with Reference 9, which fits a model of a defect binding a single carrier to the same data.

Given the model's reasonable fit to the data, it is possible to use the model to consider whether devices relying on defect-mediated luminescence in silicon will ever operate at room temperature. Equation 2.7 implies that that the dominant influence on the temperature dependence is the smaller of the carrier binding energies $E_g - E_e$ and E_h. Whereas it would be difficult to manipulate the binding energy for a given defect, the model provides grounds for optimism if we can use a defect with trap states at least 100 meV from both band edges, leading to luminescence at around 800 meV— an energy that would be ideal for telecommunication applications at 1.55 μm. This would allow for tighter binding of carriers, which is necessary for room-temperature operation. Such a defect would bind electrons and holes with roughly equal energies and would thus be beyond the scope of the model presented in Reference 9 but tractable using the model presented above. Temperature-dependent photoluminescence measurements on a system with comparable electron and hole binding energies would thus be a natural way to test experimentally the additional complexity of Equations 2.6 and 2.7 relative to the model in Reference 9.

In addition to changing defects, one could also potentially increase the number of defects through materials processing. Although the model presented above is normalized with respect to defect concentration, the absolute intensity scales with defect concentration. Furthermore, one could raise the carrier concentration by increasing the level of optical or electrical pumping. Nevertheless, the priority should be manipulating the defect energy if possible because varying the defect and carrier concentrations provides linear and sub-linear[4] enhancement of luminescence, respectively.

It is worth noting that if the defect binding energies increase enough, bound exciton escape (contained within a) might come to dominate the temperature dependence. Although including this effect in the model would have been possible, the temperature dependence of a was ignored, as noted above, to reduce the total number of fitting parameters.

In summary, we have presented a model of defect-mediated luminescence in silicon based on the kinetics of carrier emission and capture that is consistent with past experimental observations. The model indicates that the most effective way to make a device based on these principles operate at room temperature would be to uses a defect with trap states at least 100 meV from the conduction and valence band edges.

2.2 An experimental procedure for identifying and optimizing electroluminescent defects

The search for a point defect that traps both an electron and hole strongly enough to mediate substantial amounts of radiative recombination at room temperature has so far been fruitless. Aside from erbium, whose F electrons create a unique set of challenges [11, 12], the best performing point defects discovered to date are the complexes

[4] Ignoring stimulated emission.

formed by sulfur with copper or silver when they are co-implanted into silicon [13]. The luminescence from these complexes peaks between 1200 and 1400 nm, is strongest at 77 K, and persists to temperatures above 150K [13]. Though this performance is superior to that of the W and G line defects, the level of cooling required remains unacceptable. While some progress, including room temperature LED operation, has been made by using dislocations and other extended defects either alone or in combination with point defects [14–17], these efforts have not yet led to a commercial device. Because there is no obviously correct way to make electroluminescent silicon, the field is fragmented among a staggeringly wide variety of potential methods for integrating LEDs and lasers into silicon architectures. Heteroepitaxy, porosity, nanostructuring, and resonant cavities are just a few examples of the may approaches tried[5] [18, 19].

Despite this shift in focus, recent advances present an opportunity to search for the ideal luminescent defect in a manner that is both far broader and far more systematic than has been attempted previously. Computational and theoretical groups are rapidly developing the ability to move beyond defect formation energies to accurate calculations of the electronic structure of complicated defects [20]. This new theoretical capability opens up the possibility of applying inverse design methods, such as those used to identify promising photovoltaic materials [21], to search thousands of potentially luminescent defects for the desired hole and electron trapping energies. A key part of a successful inverse design methodology is high-throughput experimental screening of the candidates identified by computational methods [22]. Although high-throughput screening of luminescent materials is routine [23], university laboratories are ill-equipped to fabricate electroluminescent devices with the speed or scale necessary to support such a broad search. As can be seen in Figure 2.2a, which shows the steps used to make the

[5] Readers interested in exploring this field are encouraged to begin with the reference lists in References 18 and 19, which are both broad review articles.

LED in Reference 5, fabrication is intricate enough that uncontrolled process variation routinely confounds attempts to compare the performance of different devices.

Here we present a method for rapidly and reproducibly fabricating large arrays of silicon LEDs. The key innovation of this method is the use of unpackaged commercial silicon photodiodes as a substrate. The large exposed area of the photodiodes provides ample room for the creation of defects via ion implantation while commercial fabrication ensures excellent material and contact quality with a high degree of reproducibility between devices and between wafers. Consequently, the LED fabrication procedure can be reduced to just two steps as shown in Figure 2.2b.

To demonstrate the effectiveness of this new methodology, we used it to fabricate a W-line LED. A chip of Hamamatsu silicon p-i-n photodiodes with aluminum contacts (see Figure 2.3 for a schematic) was implanted with ^{28}Si to a dose of 10^{11} /cm^2 at an energy of 5 meV, which gives a mean implant depth of 3 μm. The implanted silicon was thus contained entirely within the high-resistivity n-type "i" layer of the photodiodes. This was necessary to avoid the complexing of silicon interstitials with boron, which is known to prevent W-line luminescence [24]. There was no need to mask the implant to protect the contacts or portions of the device surface because, at this implant energy, little or no nuclear ion stopping should occur outside the "i" region [25]. The implanted devices were annealed at 280°C for 2 minutes in flowing argon in a rapid thermal annealing instrument. After annealing, the devices were packaged and wirebonded as shown in Figure 2.4 so that each could be accessed electrically.

The devices showed the excellent current-voltage characteristics one would expect from commercial diodes. As can be seen in figure 2.5, they possess a low turn-on voltage and negligible leakage ($<$ 300 nA at 1 V) in reverse bias. This is a substantial improve-

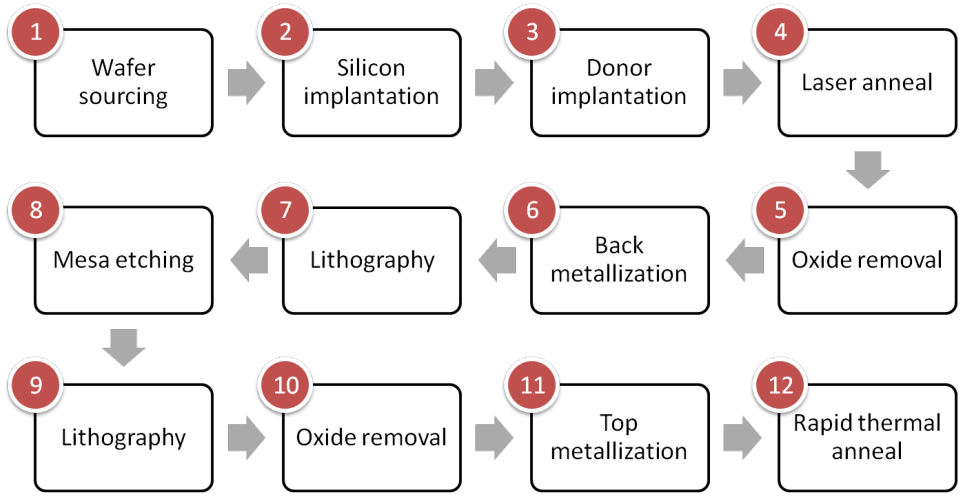

(a) LED fabrication procedure used in Reference 5. Note the many potential sources of process variation.

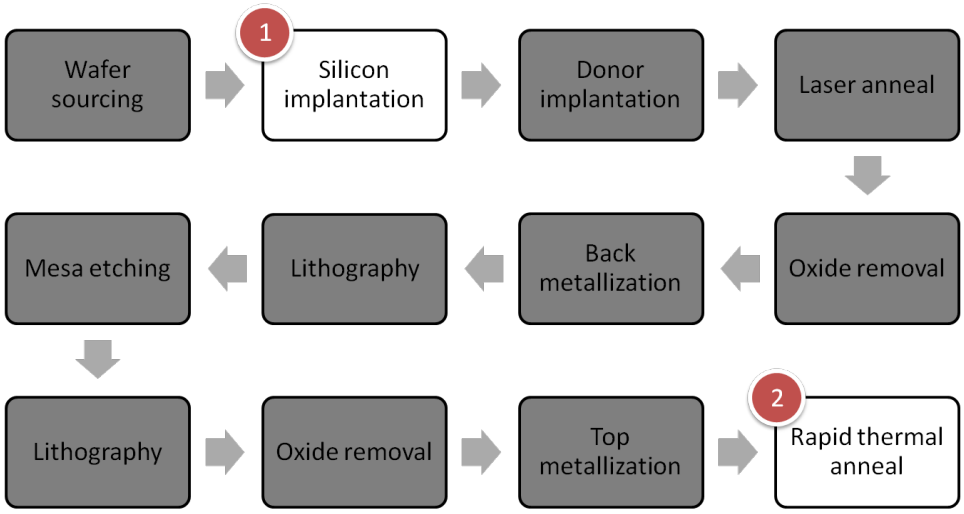

(b) LED fabrication procedure used here. Note the highly simplified process relative to Figure 2.2a.

Figure 2.2: Comparison of the LED fabrication procedure used in Reference 5 with the procedure used in this work.

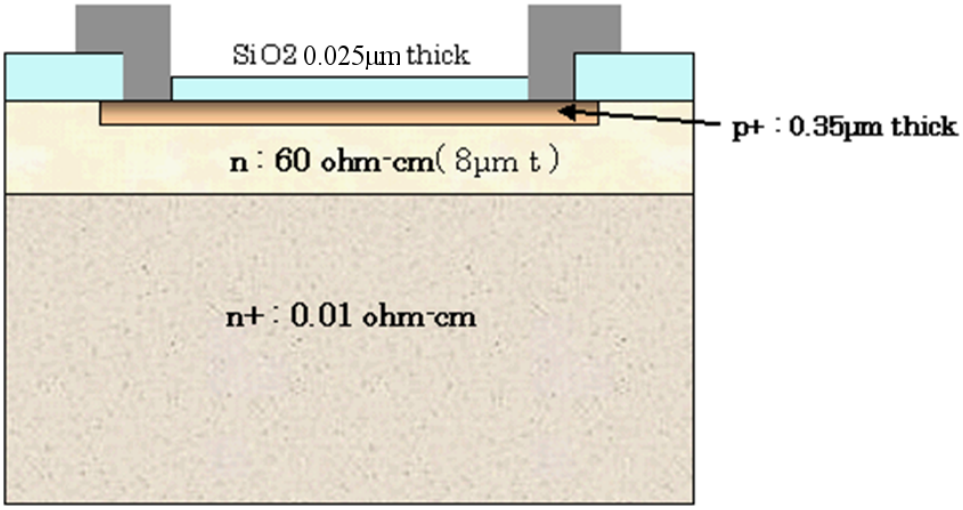

Figure 2.3: Schematic of the Hamamatsu photodiodes used in this study. The silicon implant was contained entirely within the high-resistivity n-type layer.

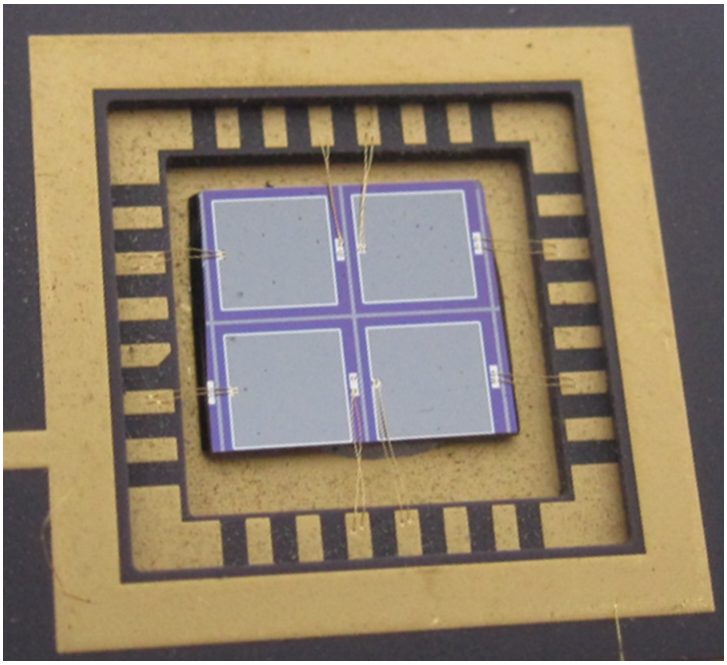

Figure 2.4: Photograph of packaged, wirebonded photodiodes. Each stripe on the package border is 1 mm wide.

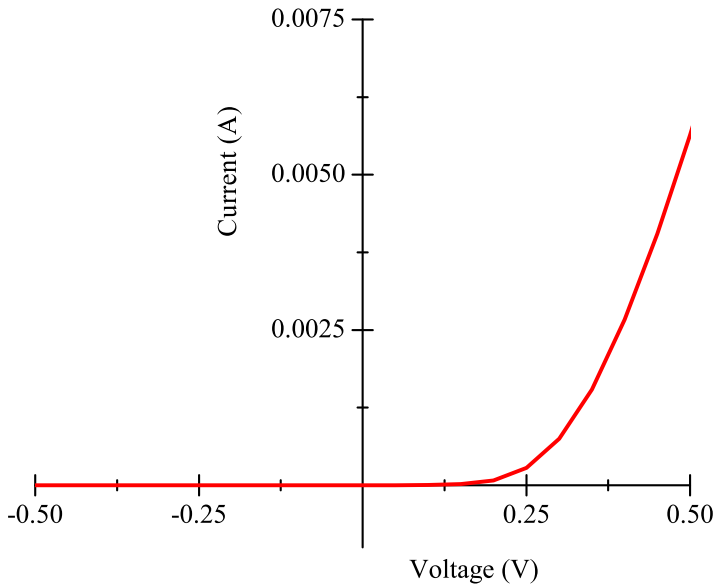

Figure 2.5: Current-voltage plot for an implanted, annealed photodiode. The I-V characteristic shows negligible leakage in reverse bias and a low threshold in forward bias.

ment over the device in reference 5, which had a turn-on voltage greater than 5 V.

The electroluminescence of these LEDs is also quite promising. Figure 2.6 shows both the electroluminescence spectrum and the W-line peak intensity as a function of current. We find that while the spectrum is comparable to that of Reference 5, the luminescence intensity of our devices does not saturate even at currents approaching 2 A. This improves upon previous work by more than a factor of 10 [5].

The one issue remaining with this method is the need for wirebonding in order to access these devices electrically. In this experiment, wirebonding was done one device at a time and thus was a source of experimental error. Variation in the resistance of wirebonds made it difficult to compare the current-voltage and luminescence vs. current curves of different LEDs. If this sort of fine comparison proves necessary in the future, it

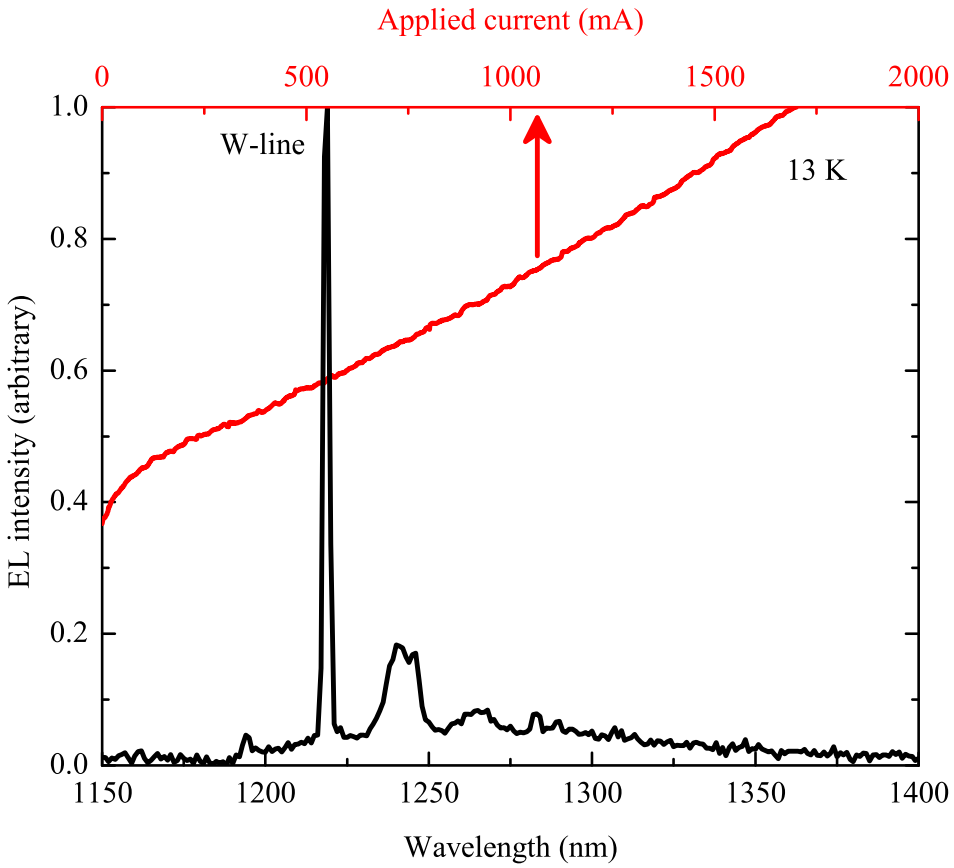

Figure 2.6: Electroluminescence spectrum of an implanted, annealed photodiode (bottom axis) along with the dependence of the W-line peak height on applied current (top axis).

will be necessary to develop a more reproducible wirebonding procedure. If wirebonding became the bottleneck in a high-throughput screening methodology, one could take advantage of the fact that all of the devices are identical in structure by building a rig with a pair of needle probes spaced to the exact width necessary to contact a device. A system with automated motion control and/or an array of probes capable of contacting a number of devices at once could speed the measurement substantially. Reproducible contact could be automated by using a camera and a simple computer-vision algorithm to align the probes to the visually obvious squares of the device mesas (see Figure 2.4) and by employing feedback from pressure sensors on the probes to ensure the same degree of contact each time. The overall electrical resistance of this setup would likely be higher than that of wirebonding, but the speed and reproducibility would make it worthwhile.

We have thus demonstrated a method that greatly simplifies the production of silicon point-defect LEDs while yielding devices with excellent performance. If coupled with an efficient way to connect these devices to an external circuit, this method will enable the use of electroluminescence as a high-throughput screening technique for evaluating luminescent point defects. Furthermore, the use of a standard commercial photodiode and transferable measurement protocols could allow the work of multiple laboratories to be combined in evaluating the suitability of different defects.

3

Material properties of silicon hyperdoped with chalcogens

Critics of the discovery of black silicon might note that the formation of high-aspect-ratio spikes on the silicon surface in the presence of SF_6 or Cl_2 plasma had already been seen [26–28], or that the process of doping silicon by laser melting in the presence of a dopant-rich gas had already been developed [29,30], or even that the concept of trapping a large supersaturation of solute in silicon by rapid solidification had already been thoroughly studied [31–33]. However, to apply these criticisms

is to miss the crux of the discovery entirely. When members of Eric Mazur's group at Harvard found that irradiation above the ablation threshold with a series of femtosecond laser pulses in the presence of SF_6 gas imbued silicon with the ability to absorb a broad spectrum of photons with energies less than its bandgap (See Figure 3.1) [34–36], they established for the first time that doping silicon above the solid solubility limit could lead to changes in its optical properties qualitatively different from anything that might have been predicted based on equilibrium doping experiments [37]. The fundamental role played by highly non-equilibrium doping in generating these novel optical properties has led to the adoption of the term "hyperdoped," coined by Tonio Buonassisi to describe semiconductors doped to concentrations far greater than the solid solubility limit without the formation of compounds or secondary phases, as a way of differentiating these materials both from typical doped semiconductors and from alloys.

3.1 From "black silicon" to "silicon hyperdoped with chalcogens"

Moving from the first observations of sub-gap optical absorption to proof that the incorporation of sulfur is the root cause of this dramatic change in properties required several careful experiments. Early work by the Mazur group focused on comparing the optical absorption of silicon irradiated with many shots of a femtosecond laser in the presence of various background gases [38, 39]. The key result of this work can be seen in figures 3.1 and 3.2 which show, respectively, the optical absorptance spectra of silicon irradiated above the ablation threshold by many femtosecond-laser pulses in the presence of gases containing sulfur and gases not containing sulfur. These experiments confirmed that the presence of sulfur was necessary for the development of broadband sub-gap optical absorption, but the complexity of the femtosecond-laser-processed material— it

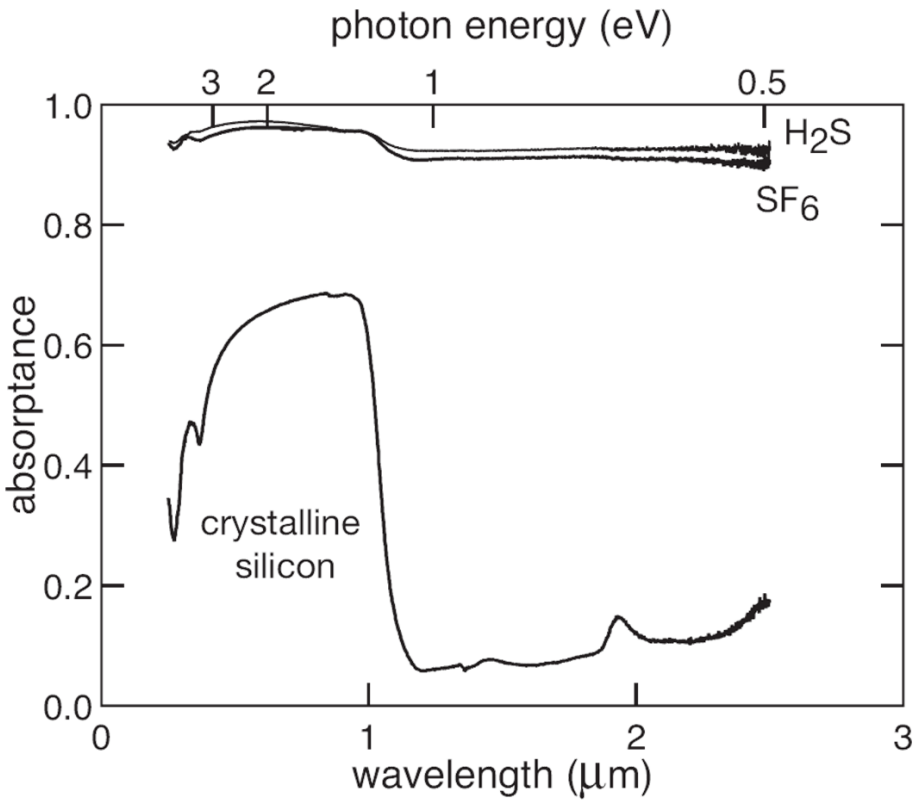

Figure 3.1: Optical absorption spectrum for black silicon produced by irradiation of a silicon wafer by many femtosecond laser pulses in the presence of SF_6 or H_2S gas. Figure adapted from Reference 39 by Mark Winkler in Reference 40 and used with permission.

has an inhomogeneously microcrystalline structure and a complex morphology consisting of high-aspect ratio, micron-scale spikes with flocculent features on their surfaces—obscured the manner in which sulfur acted.

In order to answer the question of whether sulfur incorporation was sufficient for the development of sub-gap absorption, the Mazur group turned to a collaboration with the Aziz group's nanosecond laser processing laboratory. By comparing the properties of silicon irradiated above the ablation threshold in the presence of SF_6 by a series of

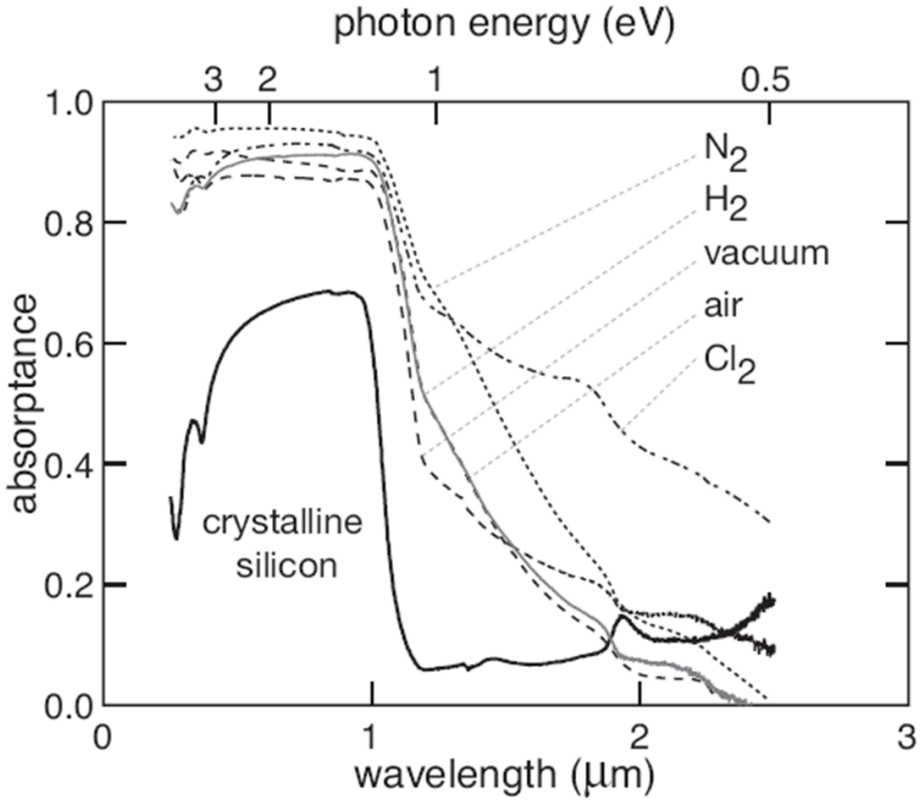

Figure 3.2: Optical absorption spectrum for materials produced by irradiation of a silicon wafer by many femtosecond laser pulses in the presence of N_2, H_2, or Cl_2 gas, vacuum, or air. In comparing with Figure 3.2, note that sub-gap optical absorption is substantially smaller in these materials than for silicon irradiated in the presence of sulfur. Figure adapted from Reference 39 by Mark Winkler in Reference 40 and used with permission.

nanosecond laser pulses with the Mazur group's standard black silicon, they found that the optical properties of both materials were effectively identical [41]. This was especially notable because the nanosecond-laser-irradiated material was monocrystalline, in contrast to the microcrystalline femtosecond-laser-irradiated material [41]. This study's elimination of the exotic, femtosecond-laser-induced structure described above as a potential cause for the change in properties led the Aziz group to explore the effects of composition directly. By ion implanting a fixed concentration (roughly 1 % at.) of sulfur into silicon and then irradiating above the melting threshold but below the ablation threshold with a single nanosecond laser pulse to heal the implantation damage (see Section 3.2), they were able to produce optically-flat, single-crystal silicon hyperdoped with sulfur [42]. This material also displayed substantial sub-gap optical absorption [42]. Importantly, two controls produced by the Aziz group, a sample implanted with sulfur but not melted and a sample implanted with silicon and melted, did not show significant sub-gap absorption and thus confirmed that sulfur incorporation into a crystalline silicon substrate was both necessary and sufficient for the creation of strong sub-gap optical absorption [43].

Having established that hyperdoping with sulfur was sufficient to induce the change in optical properties, both groups began to explore the other chalcogens, selenium and tellurium, as well. In order to incorporate selenium and tellurium into silicon, the Mazur group first dispersed elemental powders on silicon's surface before femtosecond laser irradiation [44] but eventually replaced powders with thermal evaporation of elemental films [45,46]. While the Aziz group continued to focus on using ion implantation [47], they also tried nanosecond-pulsed-laser mixing of a selenium film thermally evaporated onto silicon [48]. In all cases, the groups observed strong sub-gap optical absorption.

Comparing samples hyperdoped with sulfur, selenium, and tellurium also began to

shed some light on the metastability of the optical absorption. While it was known from early on that thermal annealing led to a sharp drop in the sub-gap absorption [36,41,42], the mechanism by which this occurred was unclear. By creating a matrix of silicon samples femtosecond laser doped with one of the three chalcogens and then subjected to one of a series of thermal anneal treatments, the Mazur group was able to argue that diffusion played an important role in the deactivation of absorption [45]. The crux of Reference 45's argument is that the deactivation of optical absorption appears to scale with the (species dependent) solid-state diffusion length across all three chalcogens. Because the spiked surface of the Mazur group's material prevented techniques such as Secondary Ion Mass Spectroscopy (SIMS) and Rutherford Backscattering Spectrometry (RBS) from producing plots of dopant concentration vs. depth, which might have provided direct evidence of diffusion, this reasoning was debated from the start. Additional cause for concern came when SIMS concentration depth profiles of Aziz group samples furnace annealed for 30 minutes at 250, 400, and 550°C (shown in figure 3.3) appeared identical to one other and to a sample that was not annealed even though their optical absorption spectra were readily distinguishable, as can be seen in 3.4. This seemed to contradict the hypothesis that diffusion lay at the heart of a thermal anneal's ability to diminish optical absorption. A subsequent extended X-ray absorption fine-structure study[1] of silicon femtosecond laser doped with selenium by the Mazur group and then subjected to a series of furnace anneals indicated that the deactivation of luminescence correlated with a change in the chemical state of the selenium atoms that was consistent with precipitation [49]. Ongoing work on single-crystal silicon hyperdoped with sulfur or selenium suggests that the kinetics of absorption deactivation are Arrhenius in temperature and parabolic in time for this material as well [50]. Although this favors

[1] This was the first work on this subject produced in collaboration with Tonio Buonassisi's group at MIT.

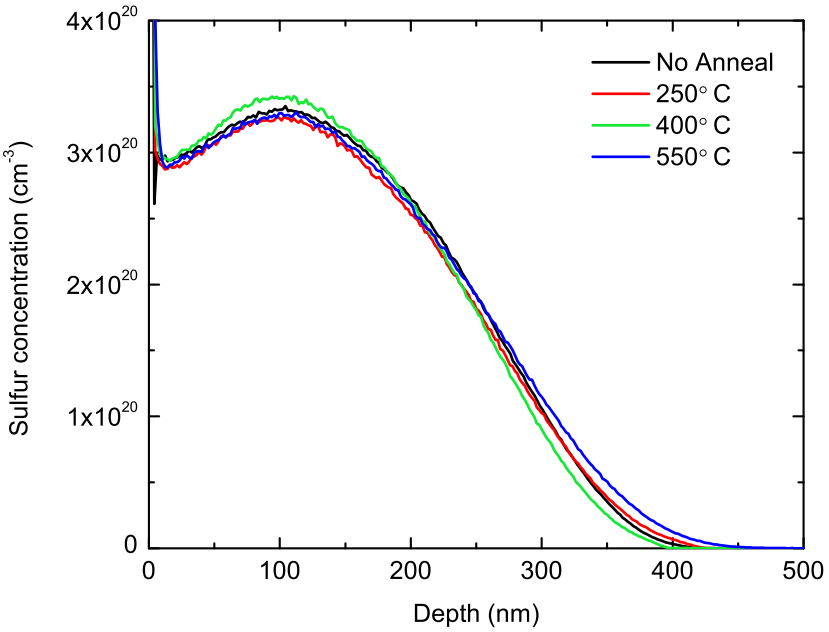

Figure 3.3: Secondary Ion Mass Spectroscopy (SIMS) concentration vs. depth profiles for silicon implanted with 10^{16} $^{32}S^{+}$ ions /cm^2 at an energy of 95 keV, then laser melted four times according to the procedure described in Setion 3.2, and finally furnace annealed at various temperatures in flowing nitrogen for 30 minutes. These data were collected as part of the work leading to Reference 47, but were never published.

diffusion as a mechanism, any model of the deactivation of absorption will have to reconcile this with the data in Figures 3.3 and 3.4 and the fact that deactivation appears to be at least partially reversible [51].

Even though the exact details of the deactivation mechanism are still being worked out, a consistent picture of the material properties of silicon hyperdoped with chalcogens has emerged. This can be summarized as follows.

1. Hyperdoping with chalcogens causes silicon to strongly absorb light with energy

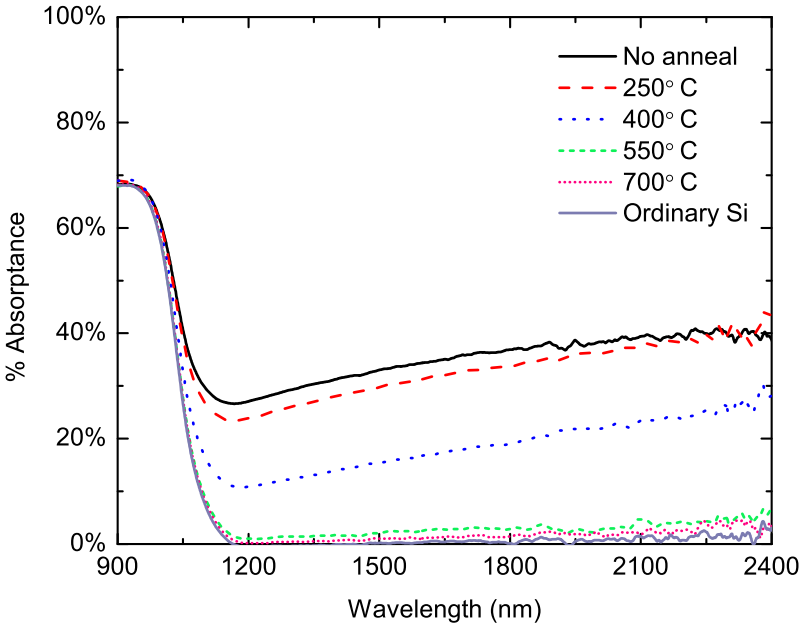

Figure 3.4: Optical absorption spectra for silicon implanted with 10^{16} $^{32}S^{+}$ ions /cm^2 at an energy of 95 keV, then laser melted four times according to the procedure described in Section 3.2, and finally furnace annealed at various temperatures in flowing nitrogen for 30 minutes. The absorption spectrum of ordinary silicon is included for reference. These data were collected as part of the work leading to Reference 47, but were never published.

from 1.1 eV to 0.5 eV or less. [42, 47, 52].

2. This effect cannot be explained by free-carrier absorption [52].

3. The strength of the enhanced optical absorption increases with chalcogen concentration [52].

4. The strength of the enhanced optical absorption decreases with thermal annealing by a mechanism that is likely diffusion limited [42, 45, 50].

This thesis seeks to build upon the above base by filling gaps in the fundamental understanding of hyperdoped materials, pushing the limits of hyperdoping as a material processing technique, and applying hyperdoped materials in optoelectronic devices.

3.2 Producing hyperdoped silicon

Before transitioning into the original contributions of this thesis to this field, it is worth pausing to describe the standard procedure developed by the Aziz group for hyperdoping bulk silicon[2]. All of the hyperdoped silicon samples discussed in this work were fabricated according to this procedure or, as will be described along with the details of specific experiments, close variants of it.

The basic outline of the Aziz group's hyperdoping procedure is shown in Figure 3.5. In this procedure silicon is first ion implanted with a fixed dose, typically betweem 10^{14} and 10^{16} /cm^3, of the desired element. For bulk silicon, the implant energy is typically chosen so that the peak concentration of the implanted species falls at a depth of roughly 100 nm. For sulfur, selenium, and tellurium, this corresponds to implant energies of 95 keV, 176 keV, and 245 keV, respectively [47]. Although the minimum implantation

[2]Detailed descriptions of the procedure used by the Mazur group can be found in References 40 and 53.

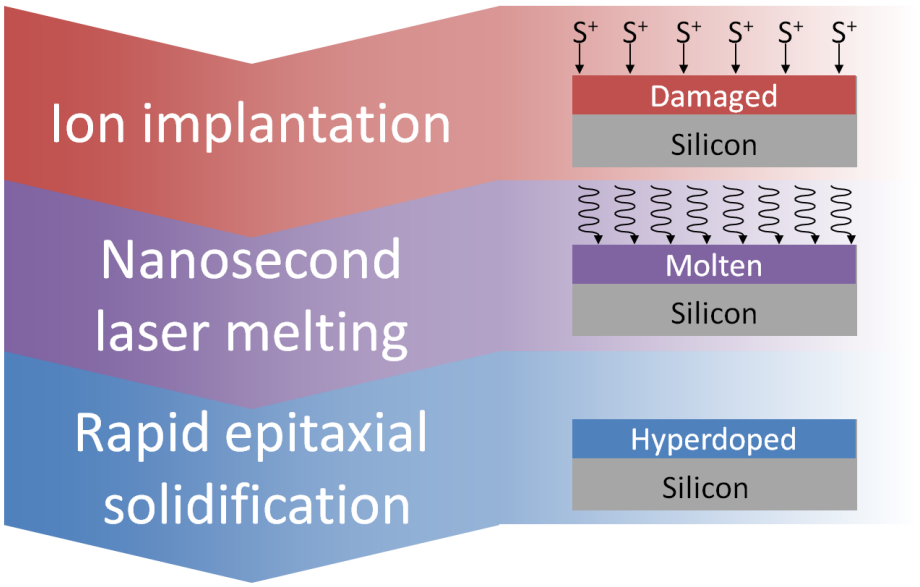

Figure 3.5: Outline of the hyperdoping procedure used by the Aziz group.

dose necessary for amorphization of silicon at these implantation energies is known [54] to be on the order of 10^{14} ions/cm^2, care is taken to ensure that all samples are fully amorphized to a similar depth before melting. Given the above threshold, it is safe to consider samples implanted at doses at or above 3×10^{15} /cm^2 completely amorphous in their top 200 nm or so. To be sure that samples implanted at doses less than 3×10^{15} /cm^3 have the same amorphous layer thickness, their doping implants are preceded by a depth-matched[3] silicon implant with a dose of 3×10^{15} /cm^2. This causes all samples have roughly identical amorphous layers regardless of dopant dose, which ensures that the thermal history resulting from laser melting will be the same for all samples.

Following ion implantation, samples are irradiated with one to four 308 nm pulses from a xenon chloride excimer laser. Pulses from this laser have a total duration of 50 ns with a full-width at half maximum of 25 ns. The laser beam is spatially homogenized by

[3]For the chalcogen enegies listed above, silicon should be implanted at 85 keV.

using a "fly's eye" optic, which splits the beam into 49 components and then superposes them on the material to be melted. Because the excimer beam is incoherent, this leads to spatial averaging without causing interference. The homogenizing optics also act as a variable magnification telescope, which enables fine control of the laser fluence via adjustments to the laser beam size. Following homogenization, the beam passes through a 3×3 mm^2 aperture in contact with the sample surface. The standard deviation of the intensity of the portion of the beam passing through this aperture is typically $< 4\%$ of the mean intensity. A typical laser beam profile is shown in Figure 3.6; quantitative line scans for that profile appear in Figure 3.7.

The laser fluence is chosen to melt all the way through the damaged layer and into the pristine, single-crystal silicon substrate underneath. For samples implanted at the energies listed above, a fluence of 1.7 J/cm^2 is ideal. When a sample is melted multiple times, the fluence of the final laser pulse is chosen to be slightly larger than that of all previous pulses (usually 1.8 J/cm^2). This guarantees that the final melt is the deepest, preventing exposure of hyperdoped material to non-melting thermal treatment.

The melt duration is measured via time-resolved reflectivity using a low-power 488 nm Ar^+ ion laser [32]. This probe laser reflects off the surface of the sample at the center of the aperture described above and is then focused onto a fast photodiode. Molten silicon is metallic and accordingly has a substantially higher reflectivity than amorphous or crystalline silicon, which are both semiconductors. Consequently, when the sample melts, the amount of probe laser light reflected by the sample and collected by the photodiode increases significantly. A typical time-resolved reflectivity trace is shown in figure 3.8.

Given a melt duration, a code (originally developed by Michael O. Thompson at Cor-

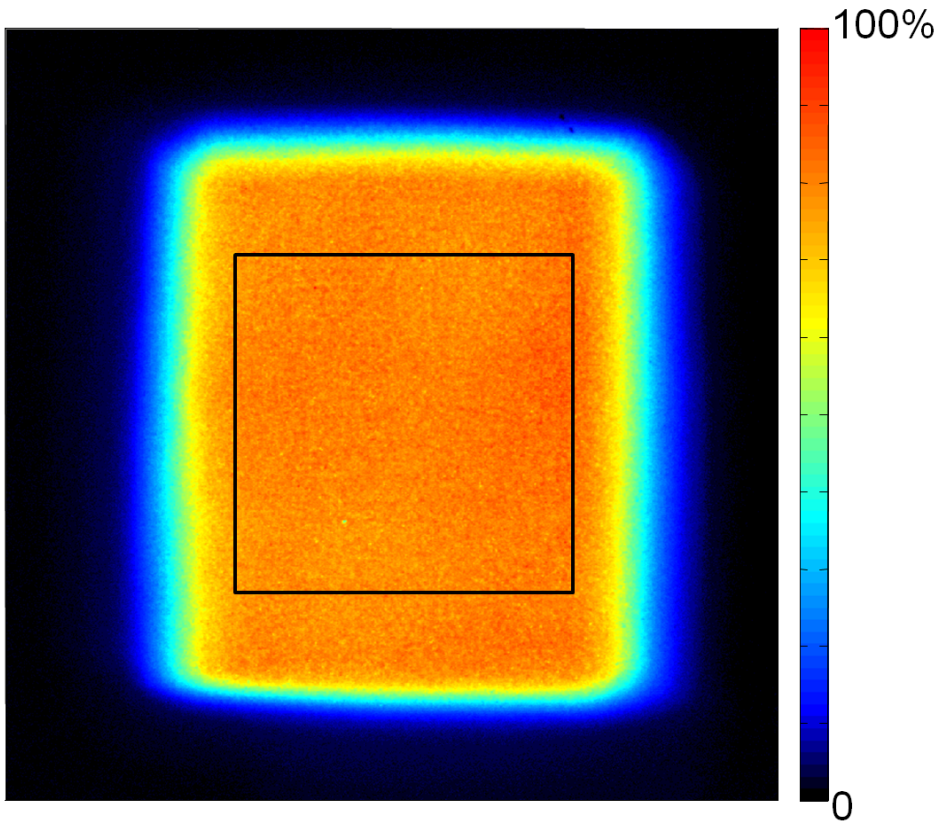

Figure 3.6: Typical beam profile of the xenon chloride excimer laser used by the Aziz group for nanosecond pulsed laser melting. The black square indicates the size and approximate position of the 3×3 mm^2 aperture. This profile was collected at the highest magnification (smallest beam size) that would be used with this aperture.

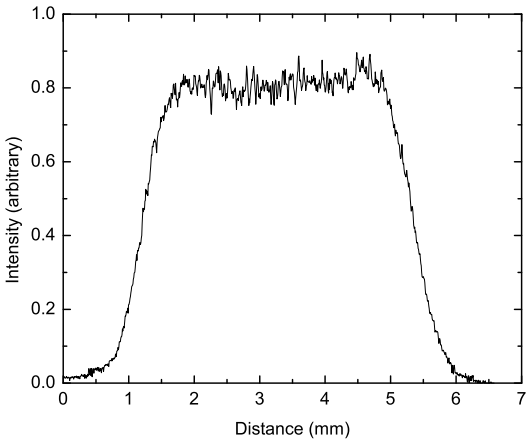

(a) Horizontal line scan

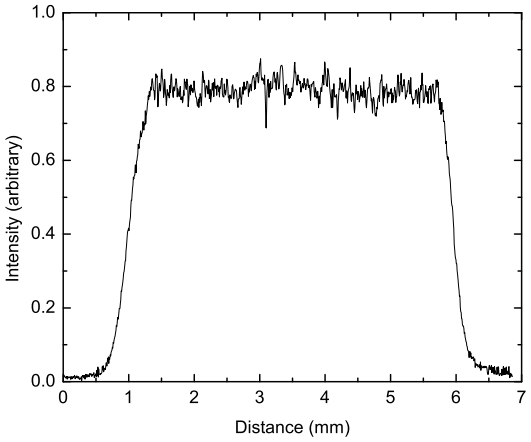

(b) Vertical line scan

Figure 3.7: Horizontal (a) and vertical (b) line scans taken through the center of the aperture on the beam profile shown in Figure 3.6.

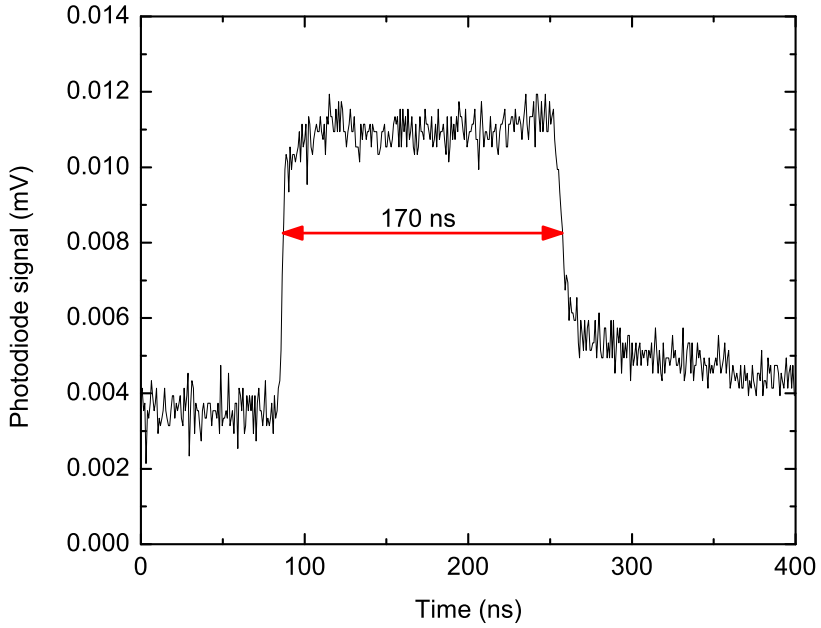

Figure 3.8: Typical oscilloscope trace from the time-resolved reflectivity measurement of a silicon sample during laser melting. The sample represented in this figure was implanted with 10^{16} $^{32}S^{+}$ ions/cm^2 and irradiated three times at 1.7 J/cm^2 and once at 1.8 J/cm^2. This figure is the trace from the final irradiation. Times of high reflectivity correspond to the period when the top surface of the sample was molten. The reflectivity does not fall to its original value immediately after solidification because the silicon remains at elevated temperature for roughly one microsecond thereafter. The red arrow illustrates how the melt duration is determined from this measurement.

nell, and subsequently modified by the Aziz group and collaborators) that simulates melting by solving the one-dimensional heat equation can be used to predict the temperature accurately, melt depth, and solidification velocity as functions of time [33, 47, 55]. The output of this code can then be used in conjunction with the as-implanted doping profile in a finite-element simulation (also developed in-house) of dopant diffusion and evaporation to predict the concentration profile after melting [47, 55].

After laser irradiation and melting, the liquid silicon solidifies rapidly; solidification velocities are typically in the 1-10 m/s range [56]. When nanosecond pulsed laser hyperdoping works properly, solidification proceeds rapidly enough that a substantial fraction of the implanted dopant remains trapped in the solid but slowly enough that the silicon has time to solidify epitaxially. The resulting material is monocrystalline, free of extended defects, and optically flat. Standard samples are melted four times to yield a relatively uniform doping profile with a fairly abrupt cutoff (see Figure 3.3) [47].

3.3 The visible and near-infrared optical properties of silicon hyperdoped with chalcogens

While the sub-gap optical absorption of silicon hyperdoped with chalcogens has been the focus of much scientific attention, the optical properties at above-gap wavelengths have mostly been ignored. This is in large part due to the experimental challenges involved in measuring these properties. While the spiked surface of black silicon immediately precluded the use of modeling-heavy optical measurement techniques such as thin-film transmission and ellipsometry, the advent of flat, single-crystal hyperdoped material did not immediately permit these measurements either. The main obstacle to measuring the above-gap optical properties was the fact that hyperdoped silicon was fabricated on a bulk silicon substrate thick enough to absorb all above-gap light passing

through the sample. Early efforts at ellipsometry were stymied by a lack of refractive index contrast between the substrate and the hyperdoped film, which prevented the use of multiple reflections to isolate the properties of the hyperdoped material. Here we describe hyperdoping the device layer of silicon on insulator (SOI) wafers with chalocgens as the key step in a method for fabricating free-standing hyperdoped silicon films and as a means to create the bottom-surface reflection necessary to extract the optical properties of the hyperdoped material using spectroscopic ellipsometry. We are thus able to report the first direct measurement of the absorption coefficients, over the range of 400 to 1600 nm, of silicon samples supersaturated with sulfur, selenium, and tellurium by ion implantation followed by pulsed laser melting.

Hyperdoping was carried out in the device layer of SOITEC SOI wafers (p-type, 001, boron-doped, 13.5–22.5 Ω-cm) with a 260 nm silicon device layer atop a 1 μm buried oxide on a 625 μm silicon substrate. The 260 nm silicon layer was ion implanted at room temperature with either 80 keV $^{32}S^{+}$, 125 keV $^{80}Se^{+}$, or 120 keV $^{130}Te^{+}$ to a dose of 1×10^{16} ions/cm^2 or 70 keV $^{28}Si^{+}$ to a dose of 3×10^{15} ions/cm^2 (for pre-amorphization) followed by 80 keV $32S^{+}$ to a dose of 1×10^{15} ions/cm^2. All implantation energies were chosen to yield an average projected ion range of approximately 80 nm.

Under these conditions, the 1×10^{16} ions/cm^2 and 3×10^{15} ions/cm^2 doses were sufficient to amorphize roughly the top 200 nm of the 260 nm device layer. The samples were subsequently irradiated with one pulse from a spatially homogenized, pulsed xenon chloride excimer laser (308 nm, 25 ns FWHM, 50 ns pulse duration) with a square spot approximately 3×3 mm^2. A laser fluence of 0.6-0.7 J/cm^2 was chosen empirically to achieve a melt depth between 200 and 260 nm (*i.e.*, beyond the amorphous layer thickness while still leaving a thin single-crystal silicon layer to seed crystal growth in the subsequent rapid solidification). Time-resolved reflectivity measurements using a low-

power Ar+ ion laser (488 nm) were used to monitor the melt duration. Figure 3.9a shows a schematic of samples after ion implantation and pulsed laser melting.

Resolidification was found to occur within a few hundred nanoseconds[4], such that chalcogen concentrations 2-4 orders of magnitude higher than equilibrium solubility in silicon remained trapped within the alloy [57, 58]. After laser treatment, electron backscattering diffraction (EBSD) on a Zeiss Supra field emission scanning electron microscope was used to confirm the monocrystallinity of each sample; sample EBSD data is shown in Figure 3.10. Even though EBSD measures the crystal structure only in the near-surface region, solidification proceeds epitaxially from the melt depth to the surface and thus if the surface is monocrystalline then the entire film must be as well. Secondary Ion Mass Spectrometry (SIMS) was performed to measure final chalcogen concentrations as shown in Figure 3.11. Because SIMS does not allow for measurements of concentration against an absolute scale, samples of implanted but unmelted material at each dose were assumed to contain their measured implant doses exactly and used as calibration standards. As can be seen from the figure, the retained chalcogen concentration increased with atomic mass. In addition, some selenium and tellurium segregated to and remained in the near-surface region after resolidification. We note that the SIMS profile for the 1×10^{15} S/cm^2 sample (not shown) is almost identical in shape to that of the 1×10^{16} S/cm^2 sample but at an order of magnitude lower concentration.

Although spectroscopic ellipsometry is widely used to measure the optical properties of thin films on substrates, interpretation (via numerical fitting) of the raw data pro-

[4]Despite presumably being able to account for the low thermal conductivity of the silicon dioxide insulator layer in the SOI samples, the Aziz group melting simulation could not accurately model the melting and solidification of silicon on insulator materials. We hypothesize that an effect not considered in the simulation, such as phonon reflection at the interface, is responsible for the discrepancy.

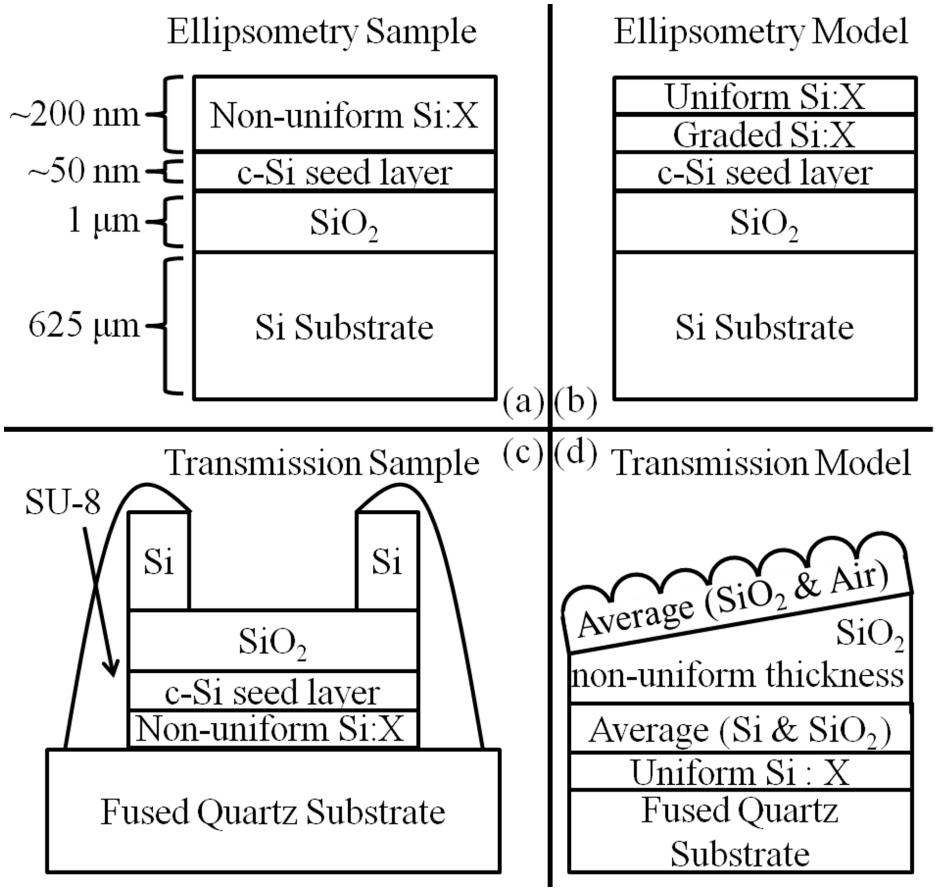

Figure 3.9: Schematics illustrating sample structures and how they were modeled. (a) Presents a sample structure after pulsed laser melting, where X is the chalcogen species. (b) Shows how samples such as the one in (a) were modeled in fitting ellipsometry data. (c) Shows a thinned sample. (d) Shows how samples such as the one in (c) were modeled in fitting transmission data with average layers serving as a model of rough interfaces.

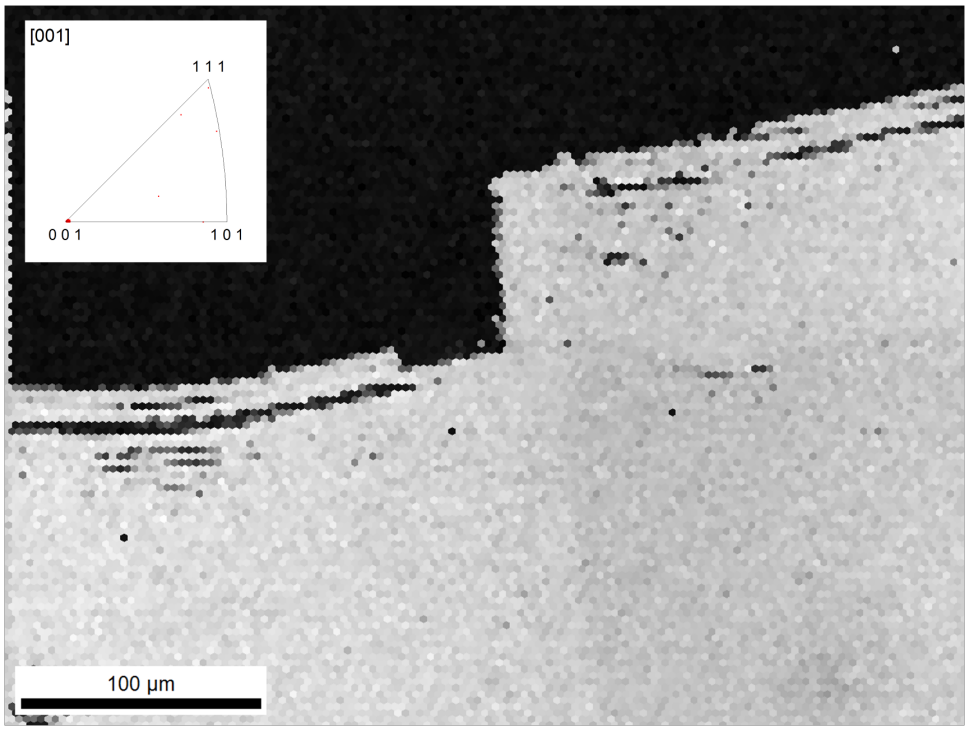

Figure 3.10: Typical electron backscattering diffraction data collected at the edge of the melted region of the 1×10^{16} S/cm² implanted sample. Light-colored areas are crystalline while dark colored areas are amorphous. A notch in the edge of the laser aperture that was later repaired is visible at the boundary between the melted (lower, light colored) and unmelted (upper, dark colored) regions. The inset shows a crystallographic pole figure for the light-colored region, indicating that it is uniformly 001 oriented and thus confirming that the resolidified material is monocrystalline.

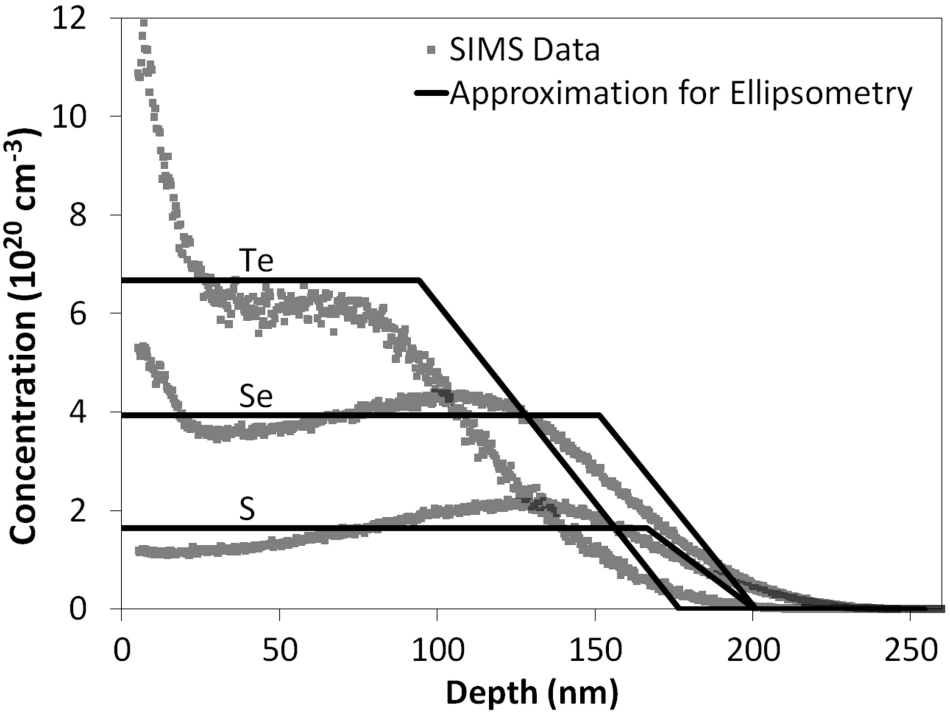

Figure 3.11: Experimental SIMS profiles (dots) of sulfur, selenium, and tellurium in SOI samples after implantation to a dose of 1×10^{16} ions/cm^2 followed by pulsed laser melting compared with the profiles (solid lines) used for fitting the ellipsometry data. The first 5 nm of data were excluded because they were visibly affected by surface transients.

duced by an ellipsometer requires one to have some knowledge of the material properties of the film being studied. Because the optical properties of these materials had never been characterized for photon energies above silicon's bandgap, direct transmission through thin films was used to obtain a first, though less precise, measurement. To perform transmission measurements through the hyperdoped layer, it was necessary to remove the 625 μm silicon substrate. We adapted the milling method used by Schmid to create optical windows in heavily doped silicon, replacing the final polishing step with reactive ion etching [59].

The 625 μm silicon layer was polished to roughly 200 μm in thickness. The sample was then mounted melted side down onto a fused quartz substrate using SU-8 photoresist so that a 5×5 mm^2 window of bare silicon remained open over the laser-melted area. The sample was then placed on a hot plate at 150°C for two hours to evaporate the resist solvent. The remaining 200 μm of silicon was removed at a rate of roughly one micron per minute by inductively-coupled plasma reactive ion etching in a Surface Technology Systems instrument using a mixture of SF_6, CF_4, and O_2. This recipe etches silicon 100 times faster than it etches SiO_2. After roughly four hours of etching, the 5×5 mm^2 of exposed silicon was removed, leaving a transparent window consisting of the oxide and hyperdoped layers, shown schematically in Figure 3.9c.

The transmittance of each sample was measured with a Hitachi U-4001 UV-VIS-NIR spectrophotometer equipped with an integrating sphere. The probe beam was focused to fit in the laser-melted region. Because the geometry of our thinned samples was not well-suited to reflectance measurements, we opted for a transmission-only technique. Fortunately, there is a long history of using transmittance-only methods to obtain the optical properties of thin films [60].

To extract the optical properties from the transmission data, thinned samples were

modeled according to Figure 3.9d. Four layer thicknesses (see Figure 3.9d) and the absorption coefficients of the hyperdoped layer at wavelengths of 400 nm, 450 nm, 500 nm, 700 nm, 900 nm, 1.1 μm, 1.3 μm, 1.6 μm, 2 μm and 2.4 μm were used as fitting parameters. The absorption coefficient as a function of wavelength was obtained by smoothly interpolating the values at the above wavelengths with cubic splines. The refractive index, n, of the hyperdoped layer was assumed to be the same as that of silicon because there was no evidence of reflections from their interface. Transmittance spectra were generated from the model by solving Maxwell's equations recursively at each interface and fit, using a least-squares method, to the measured spectra for wavelengths from 400 to 1600 nm. An example of a fit transmission spectrum is shown in figure 3.12.

Figures 3.13, 3.14, and 3.15 show the absorption coefficients determined by the transmittance fitting method. It is important to remember that these data are an intermediate step in our determination of the optical properties of silicon hyperdoped with chalcogens. Hence, the data are presented on a linear axis with each sample represented by a separate curve to emphasize the inaccuracies in the measurements of untreated SOI and the degree of sample-to-sample variation, both major motivations for completing this study using ellipsometry. It is also worth noting that even though transmission spectra were fit for wavelengths between 400 to 1600 nm, the spectra were too smooth beyond 1100 nm (as can be seen in Figure 3.12) to constrain the absorption coefficient between 1100 and 1600 nm. The ability to measure the absorption coefficient in that wavelength range for comparison with absorptance measurements of hyperdoped films on bulk substrates proved to be another advantage of ellipsometry.

Spectroscopic ellipsometry was performed on samples that had not been thinned us-

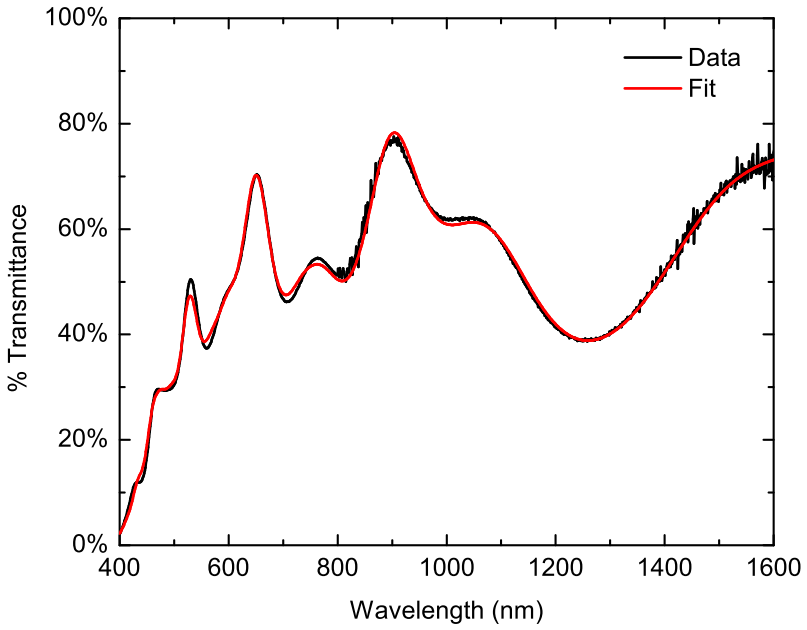

Figure 3.12: The transmission spectrum of a sample implanted with 1×10^{16} S/cm^2 and then melted compared with a fit to that spectrum using the model described in the text.

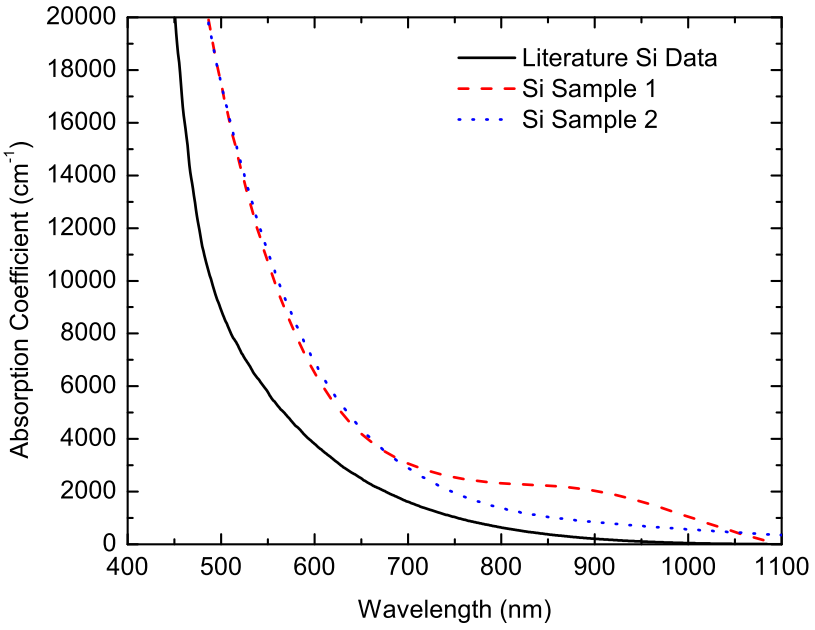

Figure 3.13: The absorption coeffecients extracted from fits to thin-film transmission measurements of thinned samples of untreated silicon on insulator (SOI) .

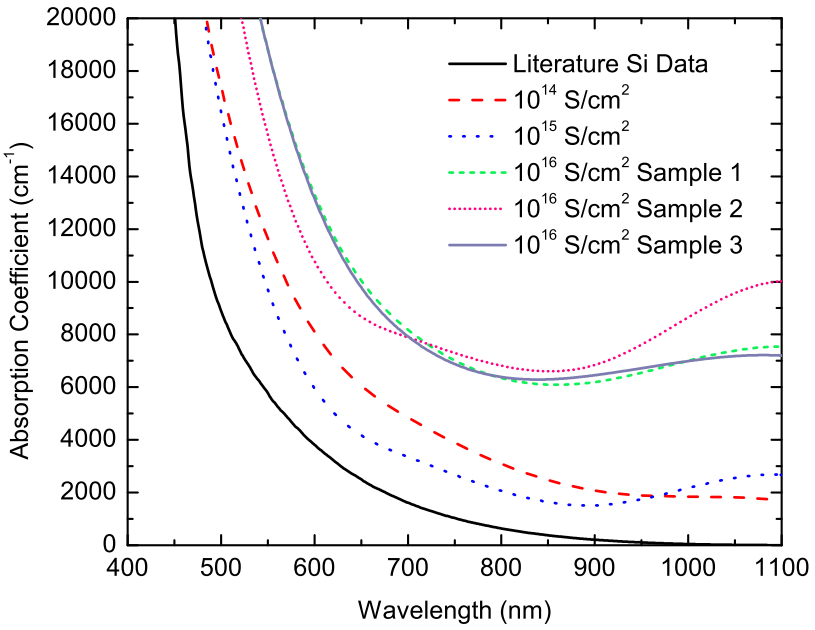

Figure 3.14: The absorption coeffecients extracted from fits to thin-film transmission measurements of thinned samples of silicon on insulator (SOI) hyperdoped with sulfur.

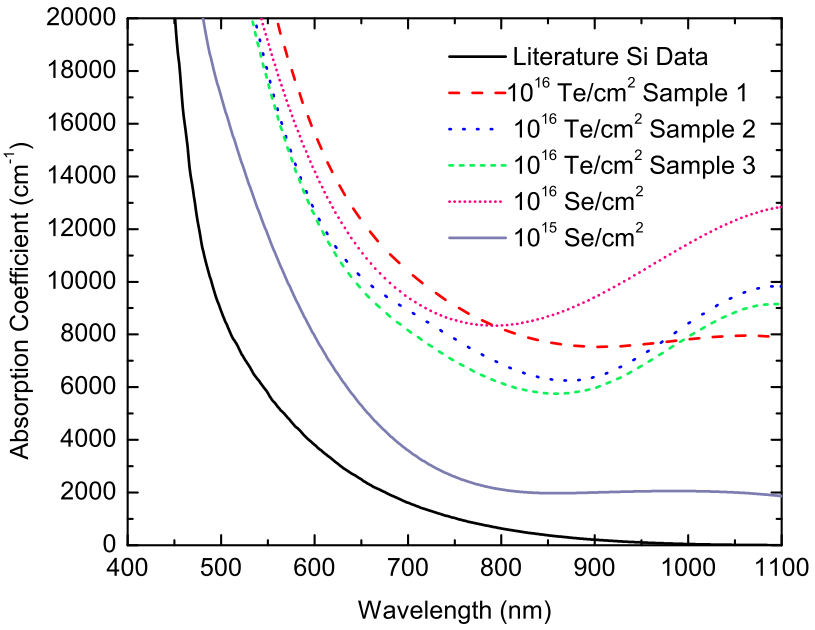

Figure 3.15: The absorption coeffecients extracted from fits to thin-film transmission measurements of thinned samples of silicon on insulator (SOI) hyperdoped with selenium and tellurium.

ing a J.A. Woollam VASE ellipsometer and raw data were analyzed with its built-in software WVASE32. The ellipsometric parameters ψ and Δ were measured every 5 nm at 65°, 70°and 75°. Focusing probes were used for all measurements to reduce the spot size to 200 μm in diameter, ensuring that the probe beam was always within the laser-treated area at all angles. Regression analysis was applied to extract the optical functions from ψ and Δ. The optical functions were parameterized with an asymmetric-oscillator-based model requiring Kramers-Kronig consistency [61]. In addition, linear grading was used to model the non-uniformity of chalcogen concentration with depth in the implanted layer. Figures 3.9a and 3.9b show schematics of the samples measured in ellipsometry and the way they were modeled respectively. Figure 3.11, containing the SIMS profiles discussed above, shows the linear compositional grading used to model the concentration profiles. Seeding the oscillator model with the wavelength-dependent absorption coefficient determined from the transmission measurements significantly improved the results of ellipsometry. In addition, because the samples measured in ellipsometry received no treatment after laser melting, we believe the results of ellipsometry to be an accurate representation of the optical properties of these alloys.

Figure 3.16 shows the wavelength-dependent absorption coefficient of all hyperdoped samples as measured by ellipsometry. Ellipsometry reports the optical properties at the average chalcogen concentration of the layer modeled as uniform (see figures 3.9b and 3.11). These concentrations, obtained from SIMS, are listed in figure 3.16. Because they are less than 25 nm thick and thus substantially thinner than the optical penetration depth, the chalcogen-rich regions occurring near the surface of the selenium and tellurium samples are assumed to have no effect other than to raise the average chalcogen concentration. These results are compared with an untreated SOI sample measured by ellipsometry and literature data on the absorption coefficient of silicon [62]. Typically,

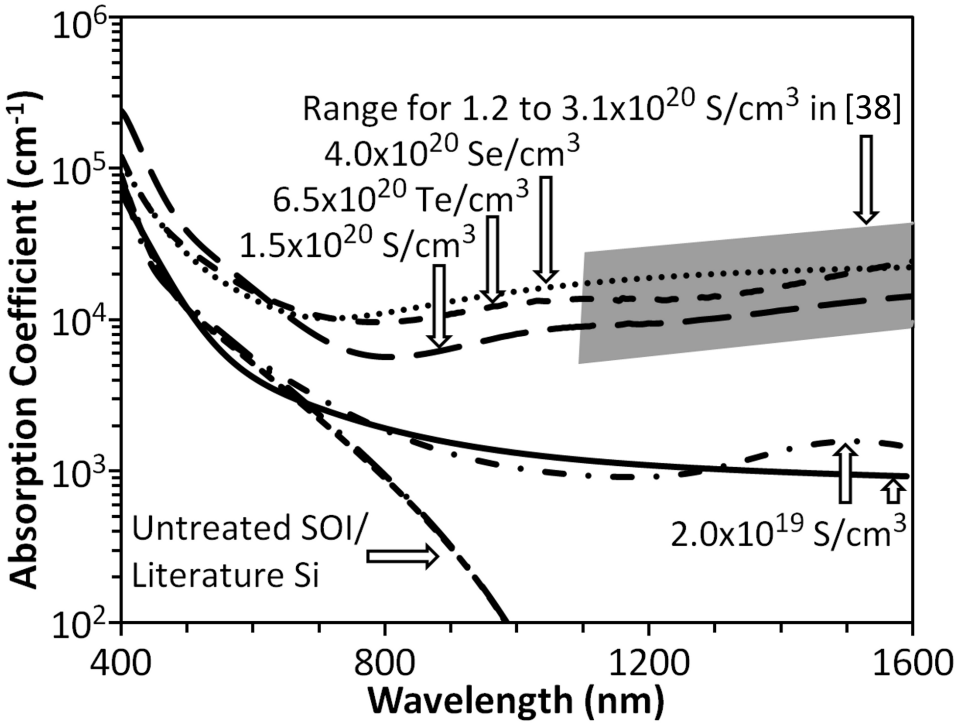

Figure 3.16: The optical absorption coefficient of chalcogen-rich silicon, as measured by ellipsometry and reckoned in the region modeled as uniform. The data are compared with those obtained in the same manner from an untreated SOI sample and the literature data on the absorption coefficient of silicon from Reference [62]. A difference of roughly 5 cm^{-1} between the measurement of an untreated SOI sample and the literature data near 1050 nm is not shown in the plot. The range of absorption coefficients measured less precisely in Reference [47] for samples with sulfur concentrations between 1.2 and 3.1 $\times$ 10^{20} /cm^3 (comparable to the 1 $\times$ 10^{16} S/cm^2 samples measured in this work) is also shown.

the results of two samples measured for each case were indistinguishable on a semilog plot and so average values are plotted. The 1×10^{15} S/cm^2 samples were an exception to this and so the results from two samples are plotted separately. In addition, this figure shows the range in which one would expect the absorption coefficient of the highly sulfur-doped samples to fall based on data for comparable sulfur concentrations from the work of Bob *et al.* [47].

Significant enhancement in the absorption coefficient is observed at all wavelengths for samples implanted with chalcogens at 1×10^{16} ions/cm^2 (the top three curves in Figure 3.16). The absorption coefficient is roughly an order of magnitude higher than that of hydrated amorphous silicon and comparable to that of cadmium telluride and other compound thin-film solar cell materials [63]. In addition, we note that the results of this work for the 1×10^{16} S/cm^{2}samples agree with, extend, and refine the sub-bandgap measurements of Bob *et al.* [47]. Little structure is observed in the wavelength dependence of absorption for these samples. The absence of peaks or other sharp absorption features suggests a lack of discrete optical transitions in this wavelength range. The slight differences in absorption coefficient among different chalcogen species may be due to several factors. The observed concentration variation caused by laser melting is one such factor, but other effects of rapid solidification may also be important. Different absorption cross sections of different chalcogen species could also play a role.

Some enhancement of the optical absorption is observed in the 1×10^{15} S/cm^2 samples (the middle two curves in Figure 3.16) for wavelengths longer than 800 nm. The order of magnitude drop in absorption for these samples relative to the 1×10^{16} S/cm^2 samples is consistent with the linear dependence of absorption on chalcogen concentration observed by Bob *et al.* for concentrations in this range [47].

In summary, we have measured the absorption coefficient of chalcogen-rich silicon

fabricated by ion-implantation followed by pulsed laser melting for the wavelength range from 400 to 1600 nm. Chalcogen doping at about 1 atomic percent leads to a marked enhancement of the absorption coefficient over the entire wavelength range studied.

4

Silicon hyperdoped with chalcogens as a light detecting material

Since the discovery of black silicon, researchers have attempted to take advantage of the remarkable optical properties of silicon hyperdoped with chalcogens by using this material in photodetectors. The Mazur group's initial work on this topic focused on incorporating black silicon into existing avalanche photodiodes [36]. It was quickly realized, however, that the key advantage black silicon offered these devices was light-trapping and so the group refocused their efforts on silicon structured by

a femtosecond laser in vacuum to avoid hyperdoping [64]. Concurrently, James Carey of the Mazur group began an effort to fabricate traditional photodiodes directly using black silicon [65]. These photodiodes displayed two remarkable properties: 1) an internal gain mechanism leading to the collection of many electrons for each detected photon in reverse-biased devices and 2) a response spectrum extended into the infrared relative to that of ordinary silicon photodiodes. The extension of response occurs in two distinct spectral regions. In the first, from the bandgap to 1250 nm, the response is as large as it is for above-gap light; in the second, from 1250 to 1600 nm, the response is detectable but more than 1000 times smaller than at shorter wavelengths [65]. These attractive device properties led to the formation of a company, SiOnyx, to develop and manufacture these detectors. SiOnyx's technology has advanced dramatically from the Mazur group's original prototypes and now shows a great deal of promise [65–69]. Nevertheless, since SiOnyx's primary mandate has been to produce a commercializable device, there has been relatively little progress on the fundamental physics underlying not only the two intriguing properties displayed by black silicon photodiodes but also the lack of optical response from this material's broad sub-bandgap absorption. This chapter reports experiments using silicon hyperdoped with chalcogens via ion implantation and nanosecond pulsed laser melting intended to clarify the relationship between sub-gap absorption and photodiode response and to identify a potential mechanism at the root of the observed photodiode behavior.

4.1 Extended infrared photoresponse and gain in silicon hyperdoped with chalcogens by ion implantation followed by nanosecond laser melting

As a first step toward understanding the remarkable photodiode behavior seen using black silicon, it is important to establish whether the same properties can be observed in silicon hyperdoped with chalcogens by ion implantation followed by nanosecond pulsed laser melting. As with previous work on sub-gap absorption (discussed in Section 3.1), an observation of gain and extended response in photodiodes produced out of flat, single-crystal hyperdoped material will allow us to study these properties in this substantially simpler system. Here we report the observation of gain and extended response similar in several ways to that observed in Reference 65, in photodiodes made of hyperdoped silicon prepared by implantation with sulfur or selenium ions followed by nanosecond pulsed laser melting.

750 μm thick double-side polished p-type Si 001 wafers with resistivity 10-30 Ω cm were ion implanted at room temperature with either 95 keV $^{32}S^{+}$ or 176 keV $^{78}Se^{+}$, to a dose of 1×10^{16} ions/cm^2. Ion-implanted samples were then irradiated in air with four pulses from a spatially homogenized, pulsed xenon chloride excimer laser (308 nm, 25 ns full width at half maximum, 50 ns pulse duration) with a square spot approximately 3×3 mm^2. A fluence of 1.7 J/cm^2 was used for the first three shots and 1.8 J/cm^2 was used for the fourth shot to ensure that the final melt was the deepest (see Section 3.2). Laser fluences were calibrated by comparing the measured melt duration of an untreated silicon wafer with numerical solutions to the one-dimensional heat equation [32]. The melt durations were monitored in-situ via time-resolved reflectivity using a low-power 488 nm argon ion laser. Laser melting and the subsequent rapid solidification form a single-crystal region that retains most of the implanted impurities but that is free

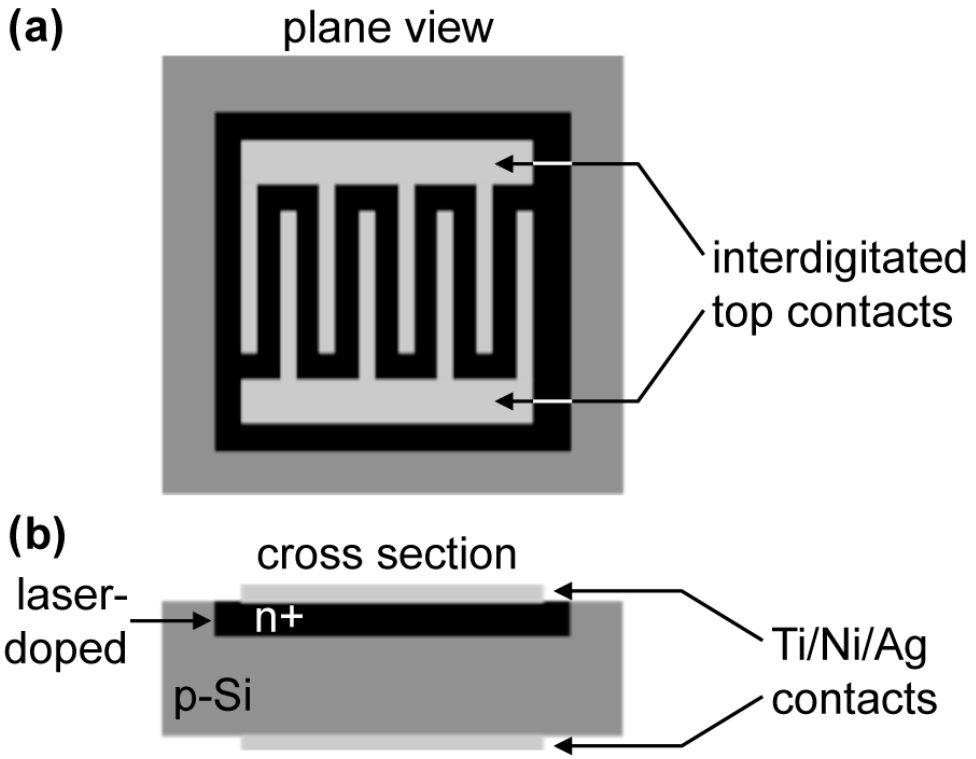

Figure 4.1: a) Top view of a hyperdoped silicon photodiode showing the interdigitated pattern of the top contacts. b) Cross-sectional schematic diagram of the diode. The substrate wafer (dark gray) is 750 μm thick and the supersaturated active layer (black) is approximately 350 nm thick over an area of 3 $\times$ 3 mm^2. The 240 nm thick Ti/Ni/Ag contacts (light gray) are deposited by electron beam evaporation as a comb pattern on the top and as a filled square on the bottom spread on an area 2.55 $\times$ 2.55 mm^2.

of extended defects [47, 70]. This region has the lateral extent of the laser spot and a thickness corresponding to the melt depth (350 nm). The resulting peak sulfur and selenium concentrations are 3 $\times$ 10^{20} /cm^3 and 4 $\times$ 10^{20} /cm^3, respectively, and the resulting retained doses of sulfur and selenium are 8 $\times$ 10^{15} /cm^2 and 1 $\times$ 10^{16} /cm^2, respectively.

Figure 4.1b shows a cross-sectional view of a n+/p diode made from a single melted

region of an implanted wafer. Treated wafers were first laser cut to a precise square geometry around each 3×3 mm^2 melted region. At this stage, some samples were furnace annealed in flowing nitrogen for 30 minutes. Prior to contact deposition, the treated wafers were cleaned in acetone, isopropanol, and deionized water, then dipped into a 1:5 HF:H_2O solution. Electron beam evaporation was used to deposit contacts made of titanium (20 nm at a rate of 0.1 nm/s) followed by nickel (20 nm at a rate of 0.1 nm/s) followed by silver (200 nm at a rate of 0.1 to 0.25 nm/s) on both sides of the sample in a deposition chamber with base pressure between 3 and 8×10^{-7} torr. Shadow masks were employed to create interdigitated contacts (shown in figure 4.1a) on the top (*i.e.*, the melted side) and a square contact on the back of the sample. Coplanar I-V measurements between the top contacts confirmed that they were ohmic. For all measurements reported below, both top contacts were held at the same potential relative to the back contact.

We report steady-state, room-temperature responsivity of these diodes under reverse bias. Light from a 50 W tungsten halide lamp was passed through a monochromator scanned from 400 to 1300 nm in increments of 5 nm. The illuminated area was approximately 3 mm wide $\times$ 1 mm high and was positioned to give maximum photoresponse for each device. The monochromatic light was chopped so that diode response could be measured using a lock-in amplifier. No filters were used from 400 to 750 nm, a 650 nm long-pass filter was used from 700 to 1300 nm, and a high-resistivity anti-reflection-coated silicon wafer was used as an additional filter beyond 1100 nm. The total incident optical power at each wavelength was measured using commercial photodiodes with well-characterized response spectra. A silicon diode was used from 400 to 1000 nm and a germanium diode was used from 1000 to 1300 nm. All measurements were made using an illumination intensity within an order of magnitude of 0.4 mW/m^2. The highest

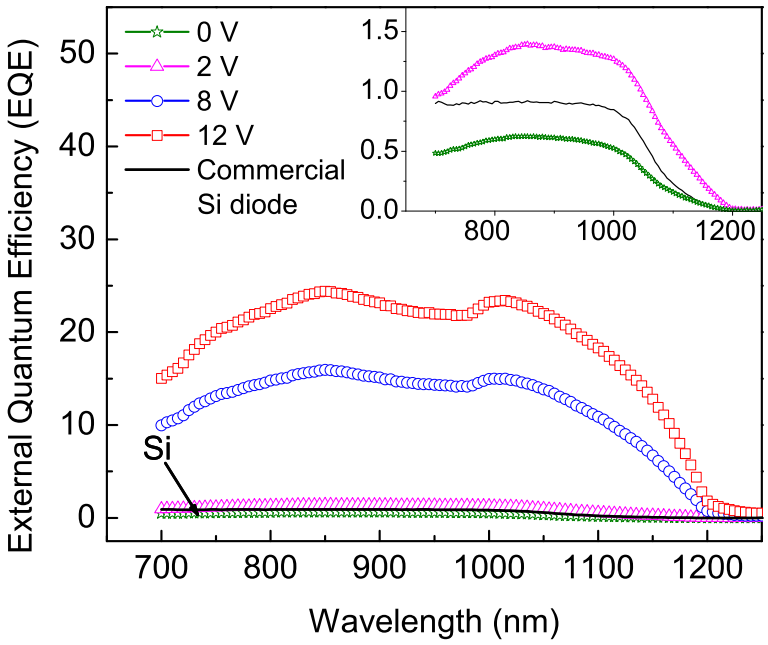

Figure 4.2: External quantum efficiency (EQE) of an un-annealed 1×10^{16} sulfur/cm^2 doped photodiode for several values of reverse bias voltage. EQE of a commercial silicon photodiode is shown for reference. The inset shows a magnified view of EQE at 0 V and 2 V reverse bias compared to the commercial silicon diode.

intensity occurred at 950 nm. External quantum efficiencies (EQE) were computed by dividing the measured photocurrent by the incident optical power and then converting to electrons per photon. In all measurements, light was incident on the top surface of samples. Note that this experiment was unable to probe optoelectronic response beyond 1300 nm and thus did not allow comparison of the response in that spectral region between our devices and the black silicon devices discussed above.

Figure 4.2 depicts the dependence of EQE on reverse bias voltage for a 1×10^{16} sulfur/cm^2 doped sample that was not furnace annealed. This photodiode shows sub-

stantial gain (EQE > 3000%) at 12 V of reverse bias. This gain decreases with decreasing reverse bias voltage, but EQE > 100% is observed even at 2 volts, as can be seen in the inset of Figure 4.2. The figure also shows the EQE of a commercial silicon photodiode, which did not vary with reverse bias, for comparison.

The cause and physics of gain cannot be identified by this experiment alone (see Section 4.3). Nevertheless, the available evidence appears to argue against both avalanche gain and photoconductive gain, at least in their simplest embodiments, as possible mechanisms. Avalanche gain seems to be ruled out by the observation of gain at 2 V of reverse bias. Such a small bias is insufficient to drive appreciable amounts of impact ionization in silicon [71]. The evidence against photoconductive gain presented by this experiment is more subtle[1]. The photoconductive gain factor is equal to the carrier lifetime for the carrier type dominating the current divided by the transit time of that carrier type across the device. In a typical silicon pn junction, an increase in the reverse bias voltage will a) have little effect on the carrier lifetime and b) cause a linear or sub-linear increase in the carrier transit speed [72]. Accordingly, for a photoconductive mechanism to account for the observed faster-than-linear increase of gain with bias, at least one of the two preceding statements, a) or b), must be incorrect. While we have found no evidence to justify rejecting either of these assertions in the case at hand, we recognize that there is some precedent for doing so. Both of these statements have been challenged in discussions of III-V quantum dot photodetectors [73, 74]. In addition, the lifetime could plausibly depend on voltage if the defect energy levels introduced by the sulfur atoms shift (e.g., as with metastable defects [75, 76]) or change occupancy under bias.

Figure 4.2 also shows that the optoelectronic response of these diodes is extended about 100 nm deeper into the infrared than that of commercial silicon photodiodes.

[1] Further evidence ruling out photoconductive gain is presented in Section 4.3.

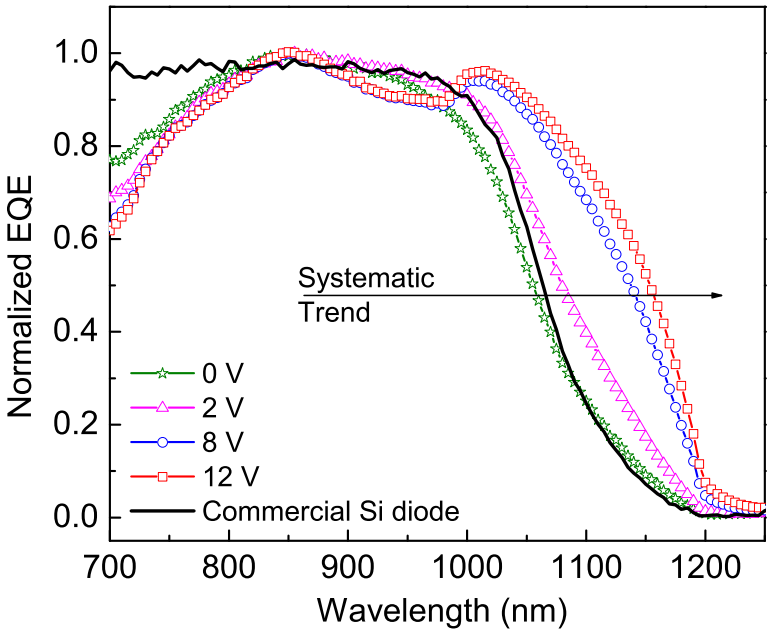

Figure 4.3: Normalized EQE spectra of an un-annealed 1×10^{16} sulfur/cm^2 doped photodiode as a function of reverse bias voltage. The extension of photoresponse to wavelengths beyond 1100 nm increases with bias voltage.

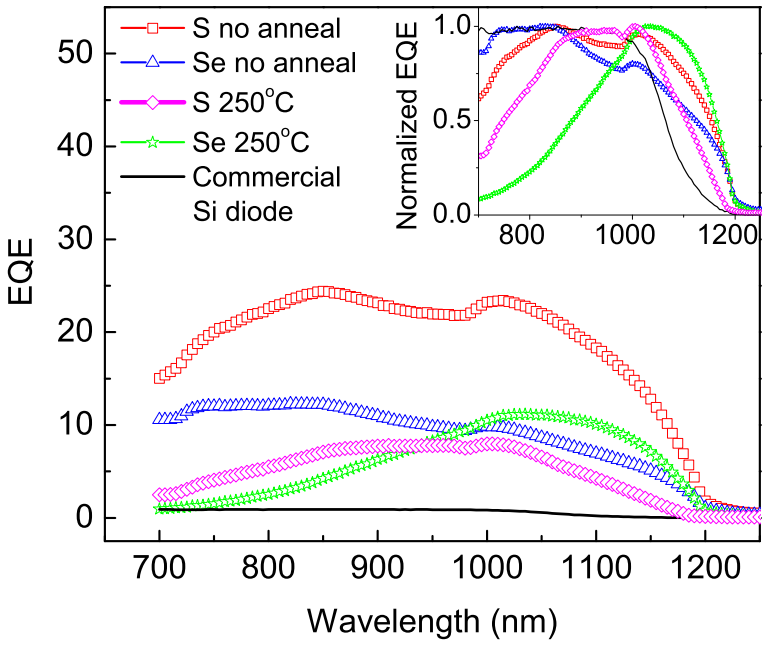

Figure 4.4: External quantum efficiencies (EQE) at 12 V reverse bias of un-annealed samples doped with 1×10^{16} sulfur/cm^2, or 1×10^{16} selenium/cm^2 and identically prepared samples annealed for 30 minutes at 250°C. EQE of a commercial silicon photodiode is shown for reference. Corresponding normalized EQE signals are reported in the inset.

This is more clearly illustrated in Figure 4.3, which depicts the data from Figure 4.2 with each curve's maximum normalized to unity. Figure 4.3 reveals that, like gain, the long-wavelength photoresponse increases with reverse bias voltage. This suggests that gain and extended response might arise from the same physical mechanism.

Figure 4.4 compares the EQE spectra at 12 V reverse bias of un-annealed samples doped with 1×10^{16} sulfur/cm^2 or 1×10^{16} selenium/cm^2 with identically prepared samples annealed for 30 minutes at 250°C. All diodes exhibit both gain and extended IR response. Normalizing the EQE spectra (as shown in the inset to Figure 4.4) reveals

that the spectra have a range of shapes. An important aspect of this variation is that the EQE from 700 to 850 nm appears to be independent of the EQE at longer wavelengths. Although the samples shown here all received different treatment, it is worth noting that, in a few cases, pairs of samples treated identically showed a similar degree of variation. In addition, as will be discussed at length in Section 4.3, gain and extended IR response are spatially inhomogeneous. Thus the roles of dopant species, annealing treatment, and inhomogeneity in explaining the observed differences in response spectra cannot be deduced from this experiment alone.

In summary, we have fabricated n+/p photodiodes having a thin (roughly 350 nm), hyperdoped (3 to 4×10^{20} /cm^3) n+ silicon top layer using ion implantation of sulfur or selenium followed by nanosecond laser melting. These photodiodes display high levels of gain (>3000% at 12 V and >100% at 2 V of reverse bias), along with substantial optoelectronic response at wavelengths as long as 1250 nm. The gain characteristics are not consistent with the behavior we would expect from avalanche gain or photoconductive gain. The mechanism for gain and extended response will be explored in Section 4.3.

4.2 Contactless microwave measurements of photoconductivity in silicon hyperdoped with chalcogens

As discussed in Sections 3.1 and 3.3, silicon hyperdoped with chalcogens by ion implantation followed by nanosecond pulsed laser melting displays significantly enhanced absorption of sub-gap light. Although, as Figure 4.3 shows, photodiodes made from silicon hyperdoped with chalcogens show little or no evidence of photoresponse due to this absorption [65], it is not known whether sub-gap absorption leads to the production of photocarriers which are not collected or whether no photocarriers are produced at all. In addition, as will be discussed in Chapter 5, there is a pressing need for reliable

measurements of the carrier lifetime of hyperdoped materials. This section attempts to shed light on both of these issues via non-contact measurements of photoconductivity in silicon hyperdoped with chalcogens using microwave reflectivity as a probe.

Photoinduced changes in microwave reflectivity are routinely used to measure photoconductivity without the confounding effects of electrical contacts [77–81]. In this technique, photocarriers generated by an optical pump beam lead to a small increase in the absorption of a microwave probe beam, which is detected as a decrease in the intensity of reflected microwaves. We report microwave reflectivity measurements of steady-state photoconductivity in silicon hyperdoped with sulfur and selenium by ion implantation followed by nanosecond pulsed laser melting. From these, we deduce upper bounds on the sub-gap photoconductivity and photocarrier lifetime in these materials.

Roughly 350 nm films doped with ^{32}S and ^{78}Se to peak concentrations approximately 2 to 3 $\times$ 10^{20} /cm^3 were prepared using the substrates (double-side polished, 750 μm thick, 10-30 Ω-cm) and the procedure described in Section 4.1, omitting furnace annealing and contact deposition. Aside from a shallower selenium implant depth, the samples should be similar in properties to those characterized previously [47]. Three identically prepared samples for each dopant were measured in a microwave reflectance setup similar to that of Borrego *et al.* [81]. Figure 4.5 shows a schematic of the microwave setup. 38 GHz microwaves emitted by a Millitech Gunn diode pass, via a waveguide, through an isolator to protect the source from reflections. A magic tee then splits the microwaves into two beams. One beam passes through an attenuator and is reflected back by a metallic shunt. The other beam emerges from a microwave emitter/collector horn and is reflected, in air, off the sample, which is mounted on an aluminum stage. The microwaves reflected from the sample and shunt then return to the magic tee where they recombine

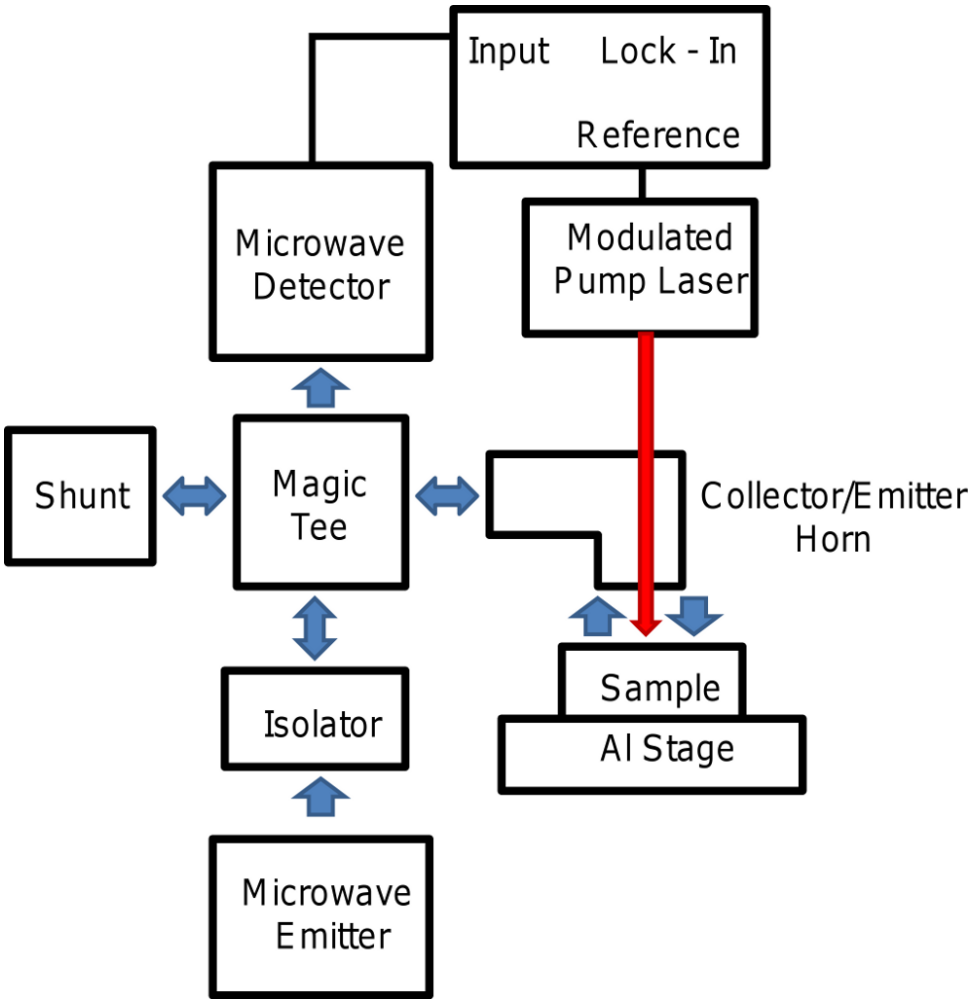

Figure 4.5: Schematic diagram of the microwave photoconductivity measurement apparatus.

and then pass, via the tee's fourth branch, through another attenuator and into a Hewlett Packard R422A crystal detector. Path lengths for the split beams were adjusted for each sample to maximize the amount of constructive interference, and thus the signal, at the crystal detector. A 1-mm-diameter hole was drilled in the microwave horn to allow the pump laser to illuminate the sample. Lasers were modulated at 286 Hz using a Thorlabs LDC500 laser diode controller. The photoinduced change in the intensity of reflected microwaves was recorded using a Stanford Research Systems SR530 lock-in amplifier. Laser wavelengths of 405, 650, 980, 1060, 1310, and 1550 nm were used. The signal varied linearly with laser power at all wavelengths. The power of light incident on the sample was generally kept below 3 mW to minimize heating. A higher incident power (36 mW) was used at 405 nm in an attempt to observe transient photoconductivity in the hyperdoped material using an oscilloscope. 405 nm was chosen because these materials' absorption coefficient, α, is greater than 100,000 /cm^{-1} at this wavelength (see Section 3.3), which provides absorption entirely within the 350 nm treated layer. Many measurements of each sample were made under each set of conditions and subsequently averaged. This experiment is similar to that of Sinton and Cuevas, but with microwaves as the probe [82].

Because the measurement involves microwave interference, we controlled for variations in sample thickness. Each sample was measured with its untreated surface resting on the stage ("down") and then measured again with its hyperdoped surface down. Because 405, 650, and 980 nm light cannot penetrate 750 μm of silicon to reach the hyperdoped layer, each sample thus provided its own untreated control at these wavelengths. Because 15% of 1060 nm light penetrates 750 μm of silicon, an additional sample was prepared where 2.7 μm (including the hyperdoped layer) were etched off using tetramethylammonium hydroxide. The signal from both sides of this sample under 1060 nm

illumination was indistinguishable from a measurement of the untreated side of a hyperdoped sample.

The measured photoinduced decrease in reflected microwave intensity results from an increase in microwave absorption. This can be expressed as

$$\text{signal} \propto \Delta A \propto \int_{\text{Sample}} \Delta a_{\mu\text{wave}}(z)\, E^2(z)\, dz \quad , \tag{4.1}$$

where ΔA is the change in microwave absorption, $\Delta a_{\mu\text{wave}}(z)$ is the change in the microwave absorption coefficient, $E(z)$ is the microwave electric field, and z is the depth. Steady-state conditions and uniform microwave illumination imply no dependence on time or the other two spatial dimensions. Because silicon is nearly transparent to microwaves while the aluminum stage is a mirror, $E(z)$ is a standing wave with a node at the stage. Silicon's microwave refractive index of 3.4 gives 38 GHz microwaves a wavelength of 2.3 mm [83]. This implies that $E^2(z)$ remains greater than 80% of its maximum in the top 350 μm of the sample and then decays smoothly with depth to the node at the stage. 405, 650, and 980 nm illuminations are thus absorbed in the region where $E^2(z)$ is nearly constant. For 1310 and 1550 nm pump wavelengths, absorbed only in the thin hyperdoped layer, $E^2(z)$ can be taken as constant for measurements with the hyperdoped layer up and zero with the hyperdoped layer down (at the node). Incomplete absorption in the substrate precludes the quantitative analysis of the response to the 1060 nm pump. Nevertheless, comparison with the etched sample would detect anomalous photoconductivity at 1060 nm, as might be expected from the enhanced photodiode response at this wavelength discussed in Section 4.1. Although the hyperdoped layer's resistivity of roughly .005 $(\Omega\text{-cm})^{-1}$ is several orders smaller than that of the substrate, the layer's thinness ensures that it will have a small effect on samples' microwave reflection and absorption in the dark [79]. Noting that the change in absorption coefficient is pro-

portional to the change in conductivity [81], combining with Equation 4.1, and pulling $E^2(z)$ out of the integral yields

$$\text{signal} \propto \int_{\text{Sample}} \Delta\sigma(z)\, dz = \int_{\text{Sample}} \Delta n(z)\, \mu(z)\, \tau(z)\, dz \quad , \tag{4.2}$$

in which $\Delta\sigma(z)$ is the change in conductivity, $\Delta n(z)$ is the photocarrier concentration, $\mu(z)$ is the carrier mobility (a single mobility is sufficient for order-of-magnitude estimates), and $\tau(z)$ is the photocarrier lifetime. Under steady-state conditions, this implies that

$$\text{signal} = C\Delta N\mu\tau \quad , \tag{4.3}$$

in which C is the constant of proportionality, ΔN is the total number of photocarriers generated per second, and μ and τ are averages over z weighted by the steady-state photocarrier distribution. Normalizing by the number of incident photons arriving per second gives

$$\frac{\text{signal}}{\text{photons per second}} = C'\eta\mu\tau \quad , \tag{4.4}$$

where the constant of proportionality C' is the same for all samples (because they have identical dimensions) and all wavelengths, and η is the quantum efficiency of photocarrier generation, a material property averaged over z weighted by the steady state photon distribution. Equation 4.4 means that the ratio of two measurements, corrected for different photon fluxes, is the ratio of the $\mu\tau\eta$ products implied by those measurements.

Figures 4.6 and 4.7 show the average photoinduced change in microwave reflectivity for the samples of silicon hyperdoped with sulfur and selenium, respectively. The data in both plots have been normalized by the number of pump photons incident per second, accounting for reflection, and scaled so that the signal from 980 nm illumination of the

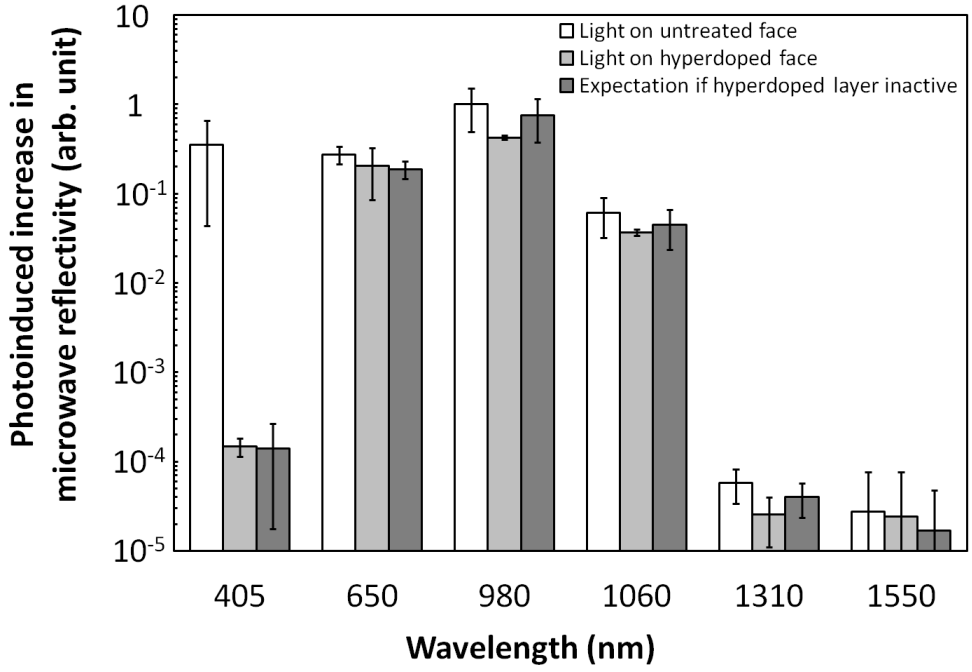

Figure 4.6: Plot of the photoinduced change in microwave reflectivity as a function of pump wavelength for silicon hyperdoped with sulfur. The white bars are control data collected with the untreated side of the sample illuminated, the light gray bars are data collected with the hyperdoped side illuminated, and the dark gray bars are an estimate of the expected signal from the substrate alone when the hyperdoped side is illuminated.

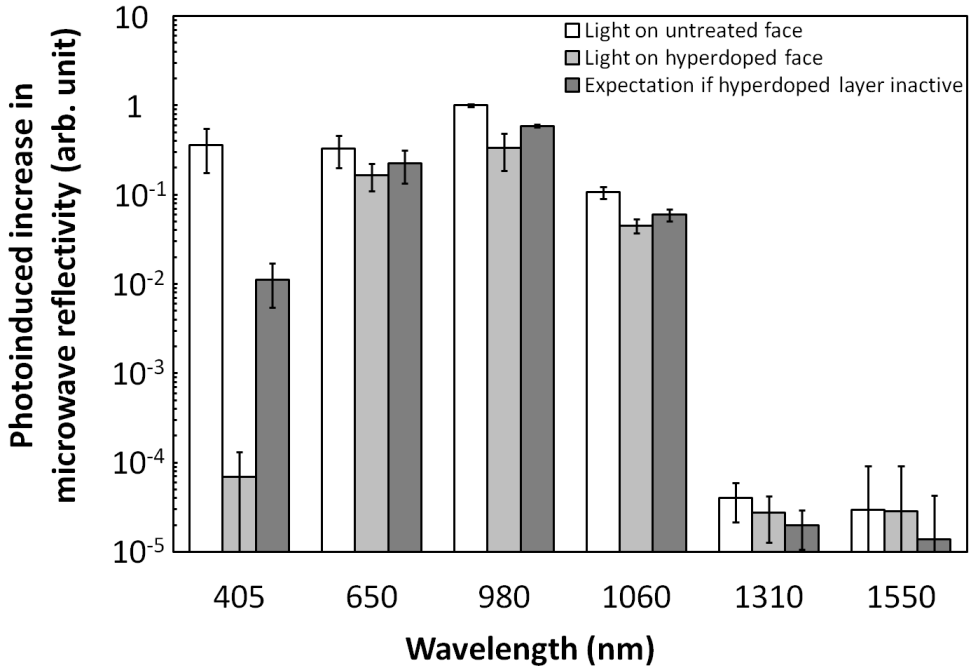

Figure 4.7: Plot of the photoinduced change in microwave reflectivity as a function of pump wavelength for silicon hyperdoped with selenium. The format is identical to Figure 4.6.

untreated side is unity. Three sets of data are shown: the signal with the untreated side illuminated, the signal with the hyperdoped side illuminated, and a calculation of the signal expected from the substrate when illuminating the hyperdoped side. Error bars represent one standard deviation in the combined three-sample datasets. The calculated data are the results when illuminating the untreated side scaled by the fraction of light transmitted by the hyperdoped layer. Recombination at the untreated surface may thus cause the calculated value to underestimate the expected signal. The transmitted fraction was computed from the optical absorption and secondary ion mass spectroscopy data (used to estimate the hyperdoped layer thickness of 350 nm) in Section 3.3 and Reference 47. Data for 1060 nm illumination is included for completeness despite the difficulties in interpretation discussed above.

At all wavelengths, our measurements were unable to detect photoconductivity in the hyperdoped material. The time-dependent photoconductivity measurements at 405 nm indicated a substrate lifetime of roughly 10 μs, but produced a null result for the hyperdoped material. Even though 650 nm illumination is absorbed near the n+/p junction, we observed no enhanced photoconductivity at that wavelength due to charge separation. Despite the intriguing device performance at 1060 nm reported in Section 4.1, we saw no evidence of anomalous photoconductivity at this wavelength either. Given that the hyperdoped layer should absorb roughly half of the unreflected light at 1550 and 1310 nm, we conclude that the photoinduced change in conductivity in hyperdoped silicon exposed to these wavelengths is at least 10,000 times smaller (on a per-photon basis) than the change in conductivity in ordinary silicon exposed to 980 nm light. A similar statement is true for 405 nm light, which is absorbed entirely in the hyperdoped layer. Combining this result with literature data gives an order-of-magnitude upper bound on the $\mu\tau\eta$ product of silicon hyperdoped with sulfur and selenium.

The conclusion of the previous paragraph implies that

$$10^{-4} \geqslant \frac{f\eta_h\mu_h\tau_h + (1-f)\eta_{Si}\mu_{Si}\tau_{Si}}{\eta_{Si}\mu_{Si}\tau_{Si}} \geqslant \frac{\eta_h\mu_h\tau_h}{\eta_{Si}\mu_{Si}\tau_{Si}} \quad , \tag{4.5}$$

in which the subscripts h and Si represent the hyperdoped material and ordinary silicon, respectively, and f is the fraction of the signal when the hyperdoped layer is up due to carriers in the hyperdoped layer. $f < 1$ because of optical absorption below the hyperdoped layer. The second inequality holds because $\eta_{Si}\mu_{Si}\tau_{Si} > \eta_h\mu_h\tau_h$. Including carrier escape into the substrate, *e.g.*, because of drift in an electric field caused by chalcogen concentration gradients in the hyperdoped layer [47], would add additional terms to the first inequality in 4.5 without changing the second. Inserting order-of-magnitude estimates for silicon's properties gives

$$10^{-4} \times 1 \times 1000 \frac{\text{cm}^2}{\text{V - s}} \times 10\ \mu\text{sec} = 10^{-6}\frac{\text{cm}^2}{\text{V}} \geqslant \eta_h\mu_h\tau_h \quad . \tag{4.6}$$

References 84 and 85 indicate that 50 cm^2/V-s is a reasonable estimate for the carrier mobility in the hyperdoped layer. Using this in Equation 4.6 implies that 20 ns $\geqslant \eta_h\tau_h$. That this bound is valid for 405 nm illumination, which should cause substantial band-to-band absorption even in the hyperdoped layer (*i.e.*, $\eta_h > 0.2$), suggests that a short photocarrier lifetime ($\leq$ 100 ns) in the hyperdoped layer is responsible for photoconductivity being undetectable there. This is consistent with the lifetime reduction due to Auger recombination observed in silicon doped to similar carrier concentrations with traditional dopants and/or Shockley-Read-Hall recombination in silicon with a similar number of deep traps [86] and prevents the use of this measurement to estimate the quantum efficiency of photocarrier generation associated with sub-gap absorption. Even though the samples measured here contain sufficient sulfur and selenium to be

metallic [84, 85], our data show carrier lifetimes much smaller than those associated with the lifetime recovery reported for silicon hyperdoped with titanium [87] and consistent with the theoretical prediction of no lifetime recovery made in Reference [88]. This will be discussed further in Chapter 5.

4.3 Surface structure is necessary for gain in photodiodes made from silicon hyperdoped with sulfur

As discussed in Section 4.1, photodiodes made from silicon hyperdoped with sulfur or selenium have two remarkable properties: internal gain, i.e., external quantum efficiency (EQE) > 100%, and a response spectrum that appears to be extended into the infrared relative to that of ordinary silicon photodiodes [65, 89]. Despite the advantages of these devices, the physics behind their extraordinary performance has remained a mystery. Here we report evidence that gain is due to a Schottky barrier lowering mechanism and occurs only at sites with noticeable morphological defects.

750 μm thick double-side polished p-type Si 001 wafers with resistivity 10-30 Ω-cm were ion implanted at room temperature with 95keV $^{32}S^{+}$ to doses of 0.1, 0.3, 0.5, 0.7, 0.9 and 1×10^{16} ions/cm^2. Ion-implanted samples were then irradiated in air with one or four pulses from a spatially homogenized, pulsed xenon chloride excimer laser (308 nm, 25 ns full width at half maximum, 50 ns pulse duration) with a square spot approximately 3×3 mm^2. A fluence of 1.7 J/cm^2 was used for single-shot samples. In four-shot samples, a fluence of 1.7 J/cm^2 was used for the first three shots and 1.8 J/cm^2 was used for the fourth shot to ensure that the final melt was the deepest. The melting procedure was otherwise the same as that used in Section 4.1. The resulting peak sulfur concentrations were between 0.3 and 3×10^{20}/cm^3 (*i.e.*, the implant dose divided by 300 nm) with roughly 80% of the sulfur retained after laser melting [47]. Following laser melting,

some samples were annealed in flowing nitrogen for 30 minutes at 250, 400, or 550 °C.

Four contact procedures were used to make photodiodes from the hyperdoped material produced as described above. The first contact procedure matched that used in Section 4.1. The second employed the same procedure except that 20 nm of Ti followed by 200 nm of Al was used as a top contact and 250 nm of Al was used as a back contact. In the third procedure, a 200 nm Al back contact was deposited and the sample was then annealed at 1000 K for 30 seconds in argon using a Modular Process Technology 600xp rapid thermal annealing instrument. Following annealing, a top contact was deposited according to the procedure of Section 4.1. The fourth procedure was identical to the third except that the top contact consisted of many 3-micron-wide interdigitated fingers spaced 5 μm apart.

EQE spectra for all devices were collected by the procedure outlined in Section 4.1. Select devices were characterized by some or all of the following additional techniques. The spatial distribution of response across the surface of devices was measured at a variety of applied biases in a light beam induced current (LBIC) setup operating at 650 and 980 nm with a lateral resolution of 50 μm. Localized heating during device operation was measured with a FLIR camera lock-in thermography (LIT) instrument with a 4$\times$ lens and a resolution of 10 μm per pixel. Devices with high response were imaged by scanning electron microscopy (SEM) and electron beam induced current (EBIC). Temperature-dependent current-voltage (IV) curves were collected by a Keithley 2400 sourcemeter in the dark and under AM 1.5 illumination from a Newport Thermo Oriel solar simulator. Surface defects were identified and counted using optical microscopy.

Measurements of EQE spectra revealed that gain and extended response occurred in 22 of 102 devices measured. Whether a device showed gain and extended response did

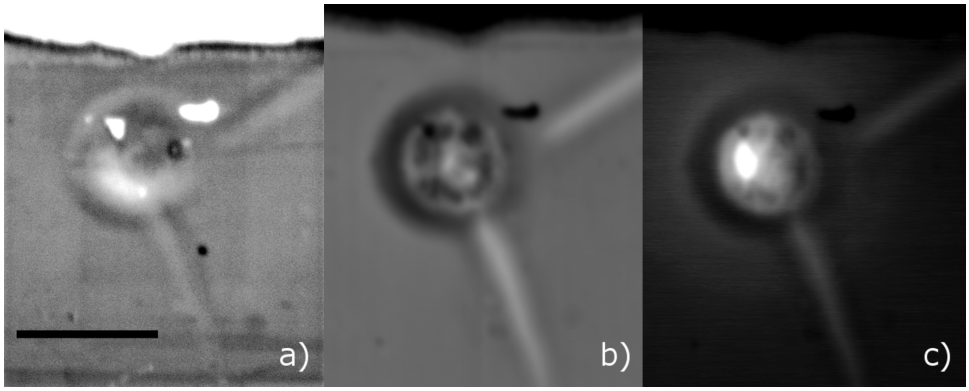

Figure 4.8: Electron micrographs of an active defect taken with a secondary electron detector (a) and electron beam induced current at 0 (b) and 3 (c) volts of reverse bias. The bright area in c) is a location in which the incident electron beam causes an anomalously large current to flow through the device, indicating that the gain mechanism is centered there. The scale bar is 20 microns. Brightness and contrast have been adjusted between b) and c) to highlight features of interest.

not appear to correlate with sulfur dose, number of laser shots, furnace anneal treatment, or contact procedure. Surprisingly, the presence of a crater-like surface defect, such as is shown in Figure 4.8a, near one of the top contact fingers was found to be a necessary but not sufficient condition for gain. Figures 4.8b and 4.8c show EBIC images of the defect in Figure 4.8a under 0 and 3 V of reverse bias. EBIC data were collected by rastering an electron beam across the top surface of the device and measuring the current through the device as a function of beam position. The electron beam was accelerated at 6 kV and had a spot size < 200 nm. Lighter colors on the image indicate that a greater current flowed through the device when the electron beam was incident at that location. As can be seen in figures 4.8b and 4.8c, applying a bias caused the device's response to the electron beam to increase dramatically in a portion of the defect. Such craters appear to be an unintended consequence of pulsed laser melting; as can be seen in Figure 4.9, we observe them in small numbers on both untreated and silicon-implanted silicon wafers

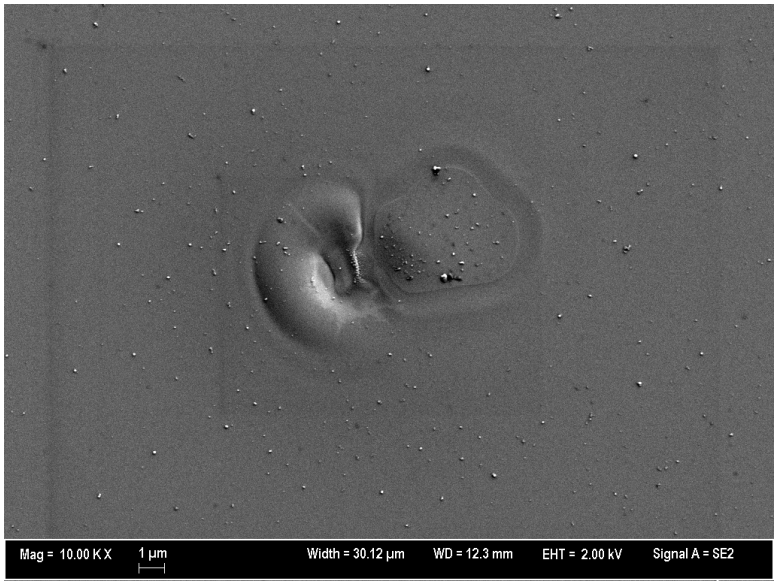

(a) Unimplanted sample

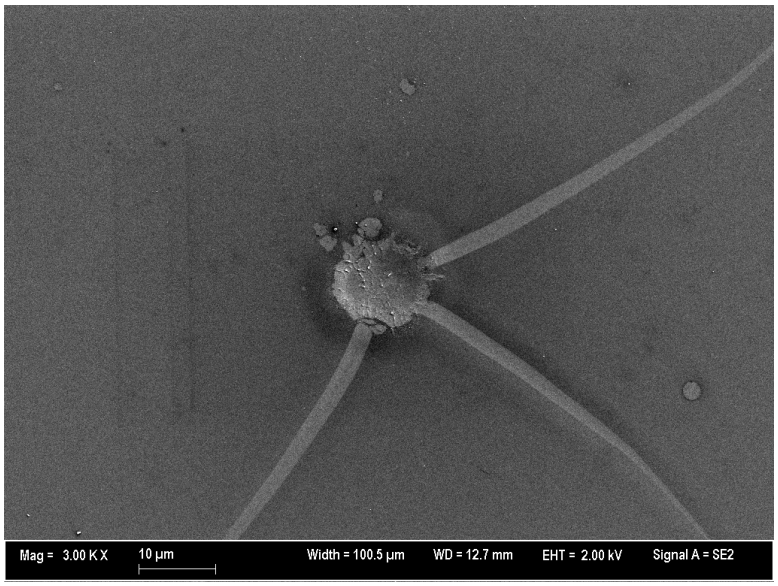

(b) Sample implanted with 10^{14} $^{28}Si/cm^2$ at 85 keV

Figure 4.9: Scanning electron micrographs of defects similar to the one shown in Figure 4.8 observed on two control samples: an untreated silicon wafer that was laser melted with one pulse and a sample implanted with 10^{14} $^{28}Si/cm^2$ at 85keV that was laser melted with four pulses.

melted in our system [2].

LBIC measurements (methodologically similar to EBIC, but with a modulated diode laser instead of an electron beam) indicated that 1) these defects responded to light as well as to the electron beam and 2) EQE values > 100 % at 650 and 980 nm occurred only at locations where these defects were within 10 μm of the top contact fingers (*i.e.*, defects observed further than this distance from contacts did not show gain). In addition, we observed that the devices with gain that were measured by LBIC had no more than three high EQE locations on their surfaces and usually only one such location. An example of LBIC data is shown in Figure 4.10. Comparing optical micrographs (not shown) of devices with LBIC data, however, revealed that the presence of defects of this type near contacts did not guarantee gain. Optical microscopy of a selection of 10 samples revealed that a typical device had a small but non-zero number of such defects (roughly 3 to 10) on its surface. In samples examined optically and/or by SEM, it was common to find defects near contacts in areas with EQE <100%. We thus hypothesize that an additional factor is necessary for a defect near a contact to yield EQE > 100%, but have not identified this factor.

[2]At one time we hypothesized that some manner of dirt, damage, or contamination of the sample surface prior to melting led to the formation of these defects during laser treatment. In an attempt to test this a number of intentionally flawed samples were prepared and melted. Fingerprints, aggressive use of Teflon or metal tweezers (these were tested separately), and the residue of isopropyl alcohol allowed to dry quiescently on the sample surface had no visible effect on the post-solidification surface morphology. Glass dust prepared by grinding a microscope slide with a mortar and pestle and then liberally sprinkled on the surface may have slightly increased the number of surface defects, but not in proportion to the amount of dust applied and not provably outside the range of normal samples. Samples coated with silicon dust prepared by grinding a wafer and samples scratched deeply with a diamond-tipped scribe prior to melting both displayed hundreds of additional defects similar to one another an not entirely dissimilar to those shown in Figures 4.8 and 4.9. However, out of a set of 4 devices prepared from samples to which silicon dust was applied, only one displayed gain and extended response. This suggests that the presence of defects due to the silicon dust did not significantly increase the probability of a sample containing an active defect. An interesting anecdotal observation from this experiment is that the defects due to silicon dust did not appear to have the radially-oriented cracks visible in Figures 4.8 and 4.9a. It may be that such cracks are a necessary ingredient for gain and extended response.

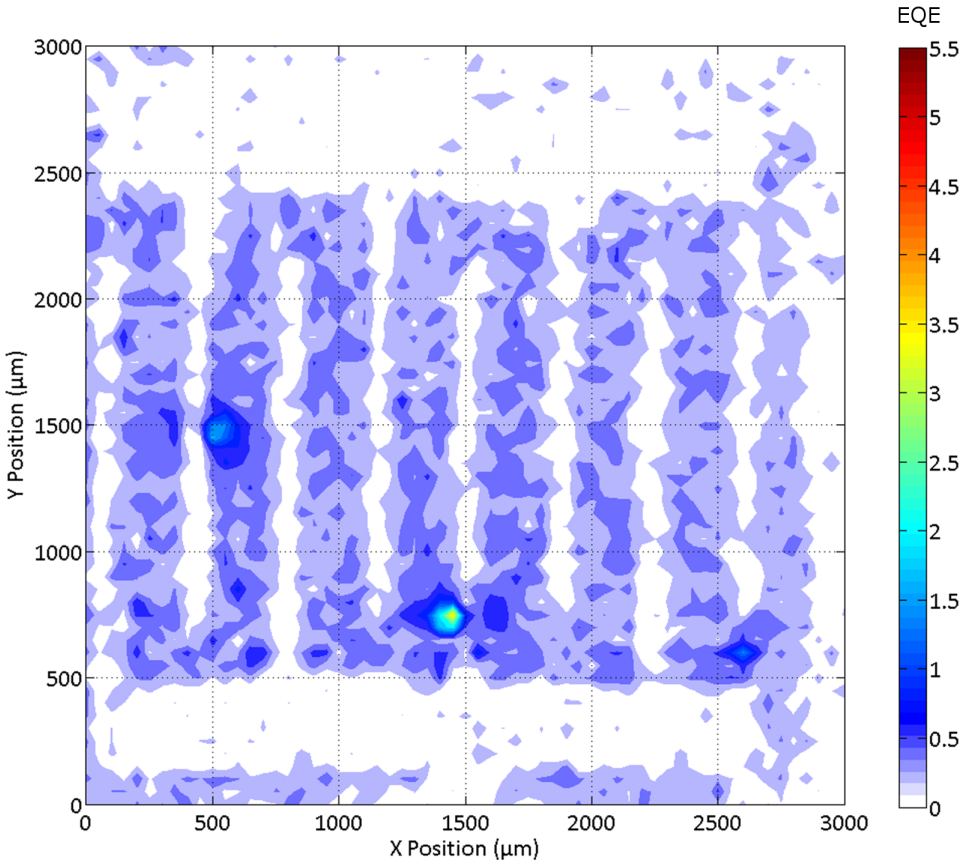

Figure 4.10: Light beam induced current (LBIC) measurement of a device with gain taken at 1V reverse bias using a 980 nm pump laser at roughly 1 mW/mm². Areas with no response (shown in white) roughly correspond to the locations of metal contacts. Three active defects can be seen on this device. This is the same device as shown in Figure 4.8, which focused on the defect in the center of this figure.

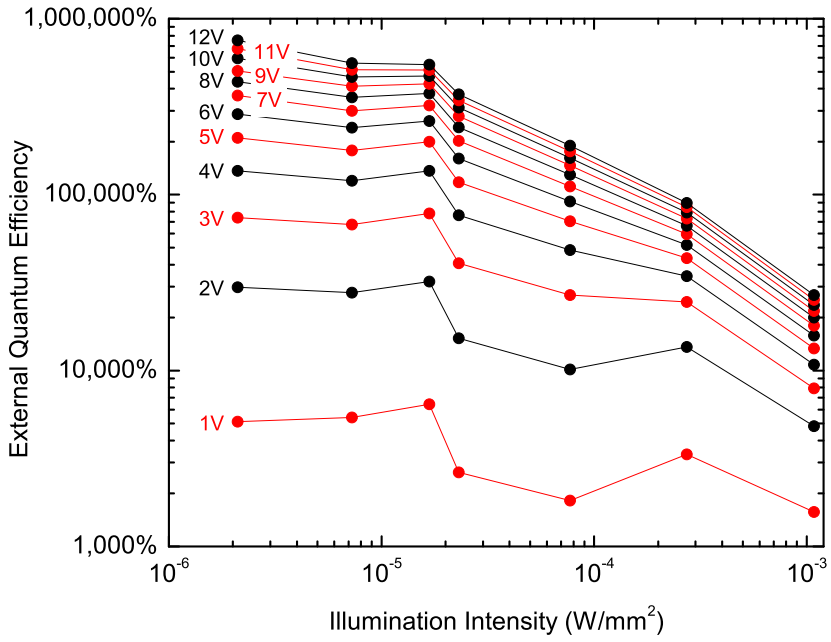

Figure 4.11: Plot of external quantum efficiency (EQE) vs. illumination intensity collected with the 980 nm laser of the light beam induced current setup incident directly on an active defect. The decrease in EQE with increasing illumination intensity indicates a saturation of the gain mechanism.

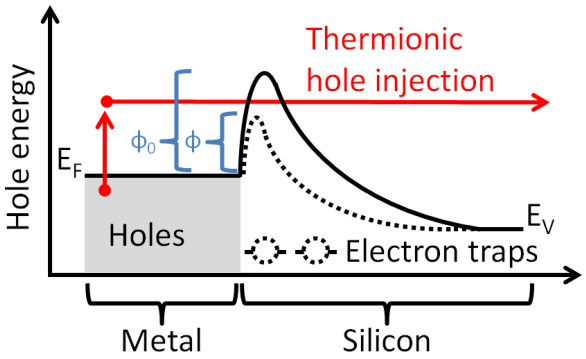

Figure 4.12: Schematic of the Schottky barrier lowering gain mechanism in which trapped electrons aid thermionic injection of holes from the metal contact into the semiconductor. The initial schottky barrier height, φ_o, and the effective barrier height under illumination, φ, are shown. The decrease in hole energy very near the interface is due to the image-force effect. After Reference 90.

The fact that the enhanced performance of these devices is driven by a small number of locations on their surfaces means that the device-average EQE measurements discussed in Section 4.1 underestimate the EQE value at active defects considerably. Figure 4.11 shows a plot of EQE vs. 980 nm light intensity measured under a series of reverse biases with the LBIC probe beam incident directly on an active defect in a device produced according to the fourth contacting procedure. As can be seen from the figure, at low light intensities, EQE values of roughly 30,000 % are observed at 2 volts of applied bias. Increasing the bias to 12 V gives an EQE above 500,000%. EQE decreases with increasing light intensity, indicating a saturation of the gain mechanism.

The high levels of gain we observe at low reverse bias voltages are inconsistent with either an avalanche or photoconductive gain mechanism[3] (see Section 4.1 and References

[3]In the case of photoconducitive gain, as discussed in Section 4.1, EQE $= \eta g$, where η is the internal quantum efficiency (photocarriers generated per absorbed photon) and $g = \frac{\text{lifetime}}{\text{transit time}}$ is the gain factor. To achieve a gain factor of 5000 (the minimum necessary for an EQE of 500,000%) with a carrier lifetime of 10 μsec (as reported in Section 4.2) in our 700 μm thick devices would require a net carrier velocity of 3.5×10^5 m/s, which is unphysical. In the case of avalanche gain, it is enough to note that bias voltages less than silicon's bandgap cannot excite appreciable amounts of impact ionization.

91 and 71). EQEs of this magnitude are possible, however, from the photoinduced Schottky barrier lowering mechanism sometimes observed in metal-semiconductor-metal (MSM) photodetectors [90, 92, 93]. In this mechanism, shown in Figure 4.12, minority photocarriers (here, electrons) captured by traps in the depletion region near a Schottky contact to a semiconductor lower the energy barrier for thermionic emission of (oppositely-charged) majority carriers (here, holes) from the metal into the semiconductor. Complete descriptions of this mechanism are given in References 90 and 92. For reverse biases $>$ 1 V, the current, I, due to this thermionic emission is well approximated by

$$I \propto -T^2 e^{-q\varphi/k_B T} \quad , \tag{4.7}$$

in which T is the temperature, q is the electron charge, φ is the effective barrier height, and k_B is Boltzmann's constant [94]. Plots of current vs. temperature at a series of reverse bias voltages were extracted from temperature-dependent IV measurements taken in the dark and under AM 1.5 illumination. AM 1.5 illumination was chosen because it was a readily available light source bright enough to saturate any reasonable number of traps. Because the high gain regions cover only a small portion of the diode's surface, the illuminated IV curves contained a substantial current contribution from the photovoltaic effect in areas without gain. This effect was removed by subtracting the short-circuit current from each IV curve so that they all reported no current at 0 V. Sample current voltage measurements are shown in Figure 4.13.

Figure 4.14 shows a plot of $-\ln(I/T^2)$ vs $\frac{q}{k_B T}$ in the dark and under illumination at 2 V of reverse bias for a device produced with the fourth contact procedure. On these axes, a linear fit is equivalent to fitting with Equation 4.7 and the line's slope gives the Schottky barrier in eV. The quality of the fits is strong evidence that Schottky barrier lowering is

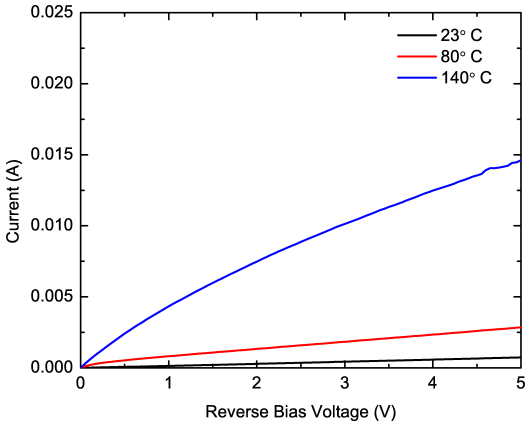

(a) Dark IV curves

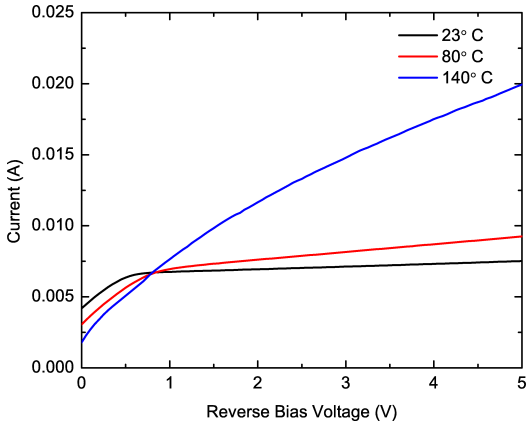

(b) AM 1.5 IV curves

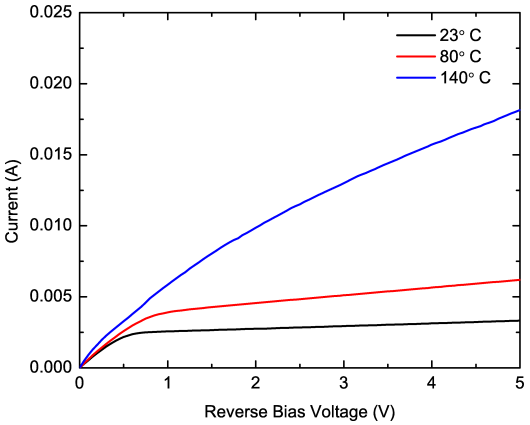

(c) Corrected AM 1.5 IV curves

Figure 4.13: Selection of the IV curves used to create Figure 4.14. Plots are shown at three representative temperatures with the device in the dark (a), under AM 1.5 illumination (b), and under AM 1.5 illumination with the short circuit current subtracted as described in the text (c).

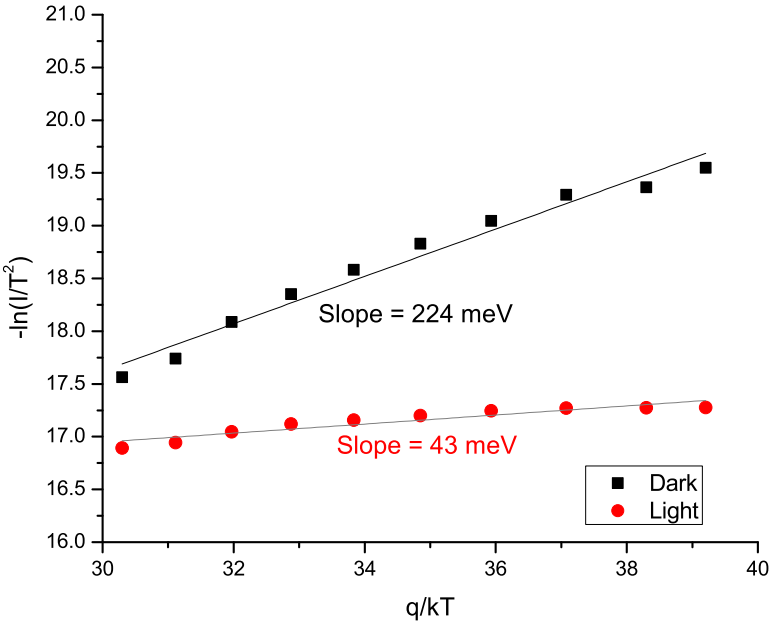

Figure 4.14: Plot of the − ln of current, I, in Amperes vs. the reciprocal of the thermal voltage in Volts^{-1} for a device with gain produced using the fourth contact procedure and measured in the dark and under AM 1.5 illumination. The slopes of the linear least-squares fits give the effective Schottky barrier height in eV.

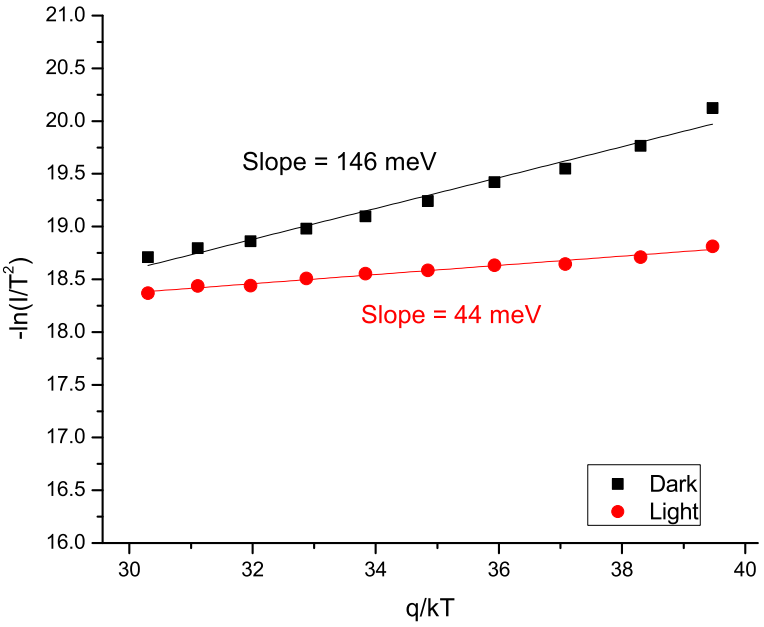

Figure 4.15: Plot of the − ln of current, *I*, in Amperes vs. the reciprocal of the thermal voltage in Volts^{-1} for a device with gain produced using the third contact procedure and measured in the dark and under AM 1.5 illumination. As in Figure 4.14, the slopes of the linear least-squares fits give the effective Schottky barrier height in eV.

the gain mechanism operating in these devices, while the slopes of the lines show that illumination led to a Schottky barrier lowering of nearly 200 meV. Identical illumination conditions lowered the effective Schottky barriers of other devices by between 100 and 300 meV. Figure 4.13 shows a second example of the analysis illustrated in Figure 4.14 for a device fabricated using the third contact procedure.

In addition to extracting the change in barrier height from measurements at a single voltage, an attempt was made to model the observed change in barrier height and its small but measurable dependence on voltage. Figure 4.16 shows barrier height as a

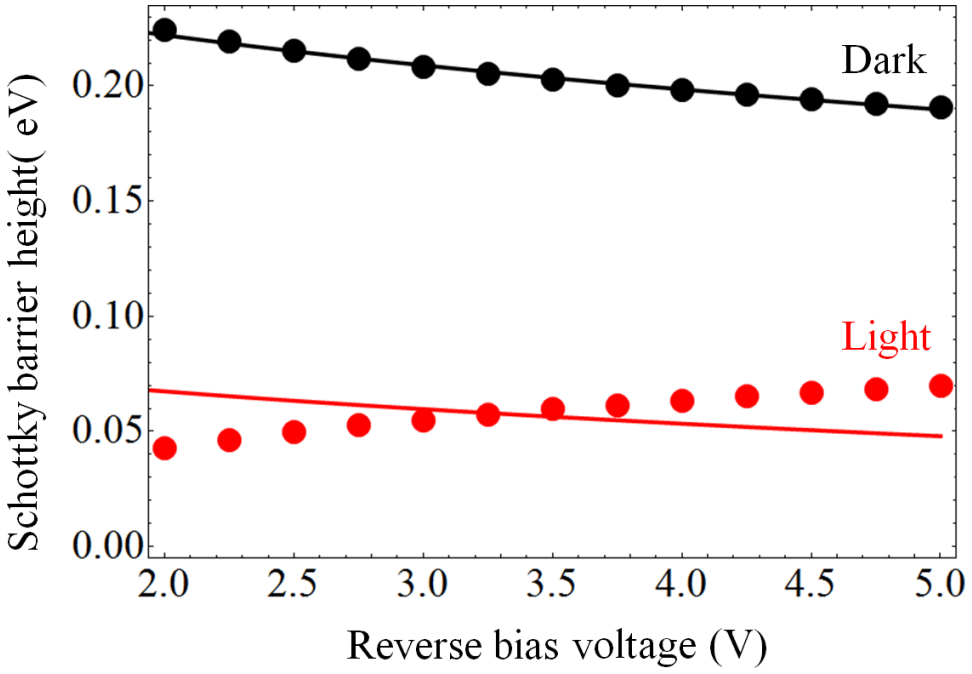

Figure 4.16: Plot of the dependence of Schottky barrier height on reverse bias voltage for the device measured in Figure 4.14. Data (points) are plotted along with fits (lines) from the model described in the text for measurements in the dark and under AM 1.5 illumination.

function of voltage and illumination computed by solving Poisson's equation (accounting for image-force lowering of the barrier height [90]) for a p-type semiconductor with a Schottky-barrier and a uniform concentration of electron traps within 1 nm of the barrier's location[4]. The acceptor and trap concentrations along with the zero-bias barrier height were used as fitting parameters. The best-fit values for these three parameters were 9×10^{17} /cm^3, 2.3×10^{20} /cm^3, and 276 meV, respectively. As can be seen from the figure, this simple model can account for the barrier heights measured in the dark and under AM 1.5 illumination and provides a good fit to the bias dependence of the barrier height in the dark. The model is unable to fit the small bias dependence of the barrier height under illumination. It may be that additional phenomena become important once the barrier height is lowered to such a small value. The best-fit trap concentration of 2.3×10^{20} /cm^3 corresponds to a physically reasonable total of 2.3×10^{13} traps/cm^2. The best-fit acceptor concentration, however, is nearly three orders of magnitude larger that the boron concentration in the substrate wafers. This suggests the presence of defects that are negatively charged regardless of the illumination conditions. This is plausible since the presence of significant damage at the location of the Schottky barrier (see Figure 4.8) could easily create a variety of electronically active defects near the surface.

Figure 4.17 plots the hole energy (the negative of the valence band edge) as a function of distance from the interface computed from the model for no applied bias in order to illustrate how the model implements the mechanism shown schematically in Figure 4.12. The inset shows the concentration of ionized dopants (traps and acceptors) back calculated from the plots in the main figure as a check. This plot reveals that the depletion width is very shallow even in the dark, further emphasizing the role of surface states in

[4]This choice of trap distribution was somewhat arbitrary. Many concentration depth profiles of traps in the depletion region could have fit the data. This particular distribution represents the hypothesis that all the traps are surface or near-surface states.

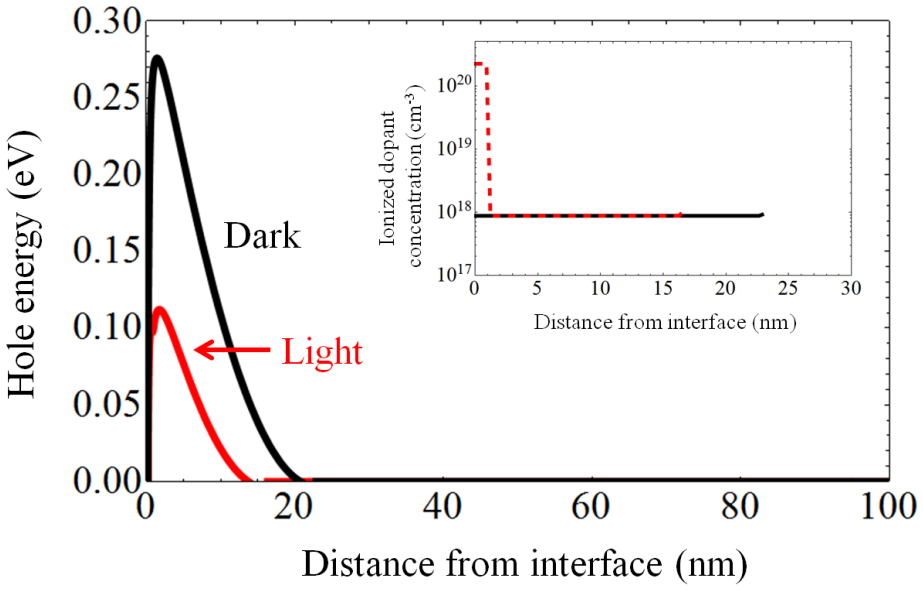

Figure 4.17: Main figure: Plot of hole energy as a function of distance from the interface at which the Schottky barrier is located as predicted by the model described in the text. Inset: concentration depth profile of ionized dopants (traps and acceptors) back calculated from the plots in the main figure as a check. The curves stop abruptly at the end of the depletion region.

our observations.

Although Figure 4.14 provides the most direct evidence for barrier lowering as the gain mechanism, several other characteristics of these devices support this explanation as well. Recent work on gallium nitride MSM photodetectors [92] attributed an extension of the response spectrum by roughly 50 nm toward sub-bandgap wavelengths and a saturation of gain with increasing illumination intensity to this mechanism. The saturation of gain with increasing light intensity in that work is a result of the finite number of traps present near the Schottky barrier [92]. Figure 4.12 indicates that we observe the same phenomenon.

The extension of response in Reference 92 can be explained by large gain factors be-

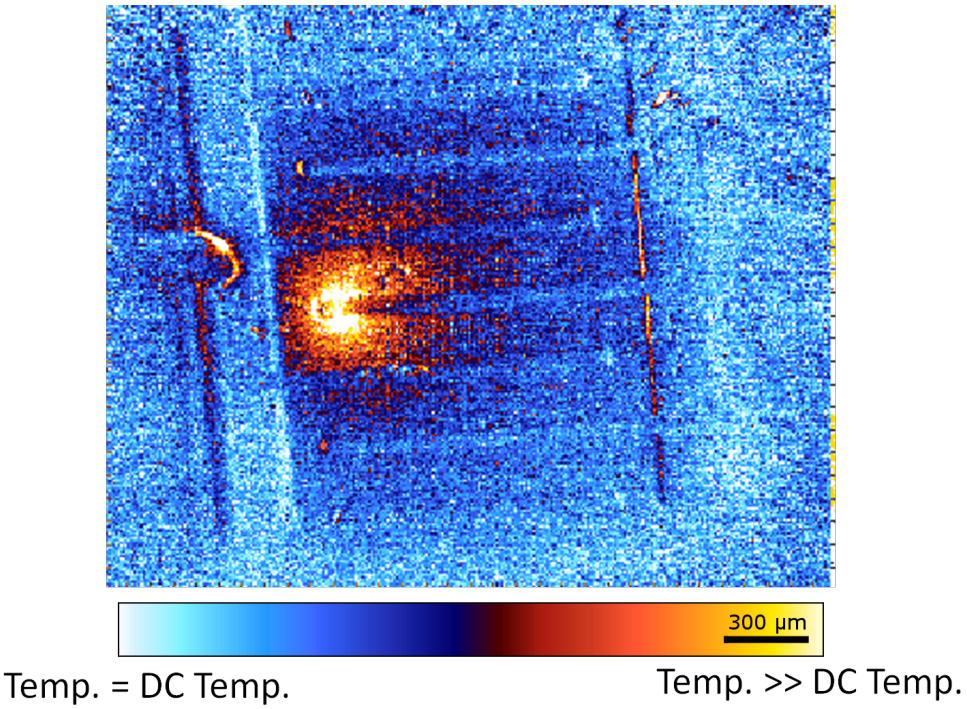

Figure 4.18: Lock-in thermography image of a device with gain taken at 10 V reverse bias under uniform illumination from a white LED. The orange area indicates local heating due to excess current flow at the location of an active defect.

ing applied to their devices' small, intrinsic sub-bandgap response. We believe that the same effect is responsible for the extension of response in the photodiodes considered here and in Section 4.1. The direct, contactless measurements of the photoresponse of silicon hyperdoped with chalcogens discussed in Section 4.2 found no evidence of response in the hyperdoped material at any wavelength above or below silicon's bandgap. Furthermore, the high-EQE region of the response spectra of photodiodes made from silicon hyperdoped with chalcogens shown in Figure 4.3 extends no further into the infrared than the response spectra of the best silicon solar cells [95]. Accordingly, amplification of the silicon substrate's sub-gap photoresponse is the most plausible explanation for the observed response spectra.

Although our measurements indicate that an MSM-like Schottky barrier lowering mechanism applies to our devices, the manner in which an MSM configuration arises requires elaboration. Electron microscopy, optical microscopy, and optical profilometry indicate that the defects create topography much taller and deeper than the thickness of the 350 nm hyperdoped layer. This suggests that these defects provide a potential conduction path directly from the top contacts into the p-type substrate, *i.e.*, an approximation of an MSM configuration. The presence of this conduction path is corroborated by lock-in thermography measurements, an example image from which appears in Figure 4.18. These show that when devices with gain are reverse biased, active defects become substantially hotter than the rest of the device. This indicates that active defects do indeed shunt the n+/p junction formed between the hyperdoped layer and substrate. We thus conclude that the defects yield an MSM configuration by bypassing the n-type hyperdoped layer and forming a direct electrical connection between the top metal contact and the silicon substrate. However, as mentioned above, not all defects near contacts are active. We thus propose that the unidentified factor necessary for a defect to be active is a low-resistance conduction path between a contact and the defect. The physical location of the Schottky barrier that is lowered is likely somewhere on that path. One candidate for such a path is the radial cracks visible in figures 4.8 and 4.9b. The fact that these cracks have an appearance that is light in color but independent of applied bias in the EBIC data in 4.8 indicates that they are more conductive than the surrounding material. They could thus provide a low-resistance connection between the active portion of the defect and the contact.

Since Carey's original publication on hyperdoped silicon photodiodes, their mechanism of operation has been a source of debate. Because Carey's femtosecond-laser-doped devices possessed a spiked surface, a microcrystalline structure, and high concen-

trations of fluorine in addition to the sulfur hyperdoping, there were several candidates for the origin of gain and extended response. The observation of a number of strong similarities between the single-crystal devices reported in Section 4.1, which resembled standard silicon photodiodes except for hyperdoping with chalcogens, and Carey's devices seemed to indicate that hyperdoping might be responsible for gain and enhanced response between 1100 and 1250 nm not only in our devices, but in Carey's as well. By finding no correlation of gain with sulfur concentration over an order of magnitude variation in implant dose, the results of this section suggest that hyperdoping with chalcogens is not the cause of gain. Conclusive proof of this, however, will require control devices identical to those discussed here except implanted with phosphorous or arsenic instead of sulfur. This is a potential topic for future experiments.

In summary, closer examination of devices identical to those in Section 4.1 has revealed that local areas of damage, an unintended consequence of nanosecond laser melting, are at the heart of the devices' anomalous performance. Furthermore, we have observed that variations in the chalcogen concentration, laser treatment, and furnace anneal do not correlate with changes in the amount of gain or the response spectrum. Thus it appears that surface structure is necessary for gain and extended response in silicon photodiodes hyperdoped with chalcogens.

5

Hyperdoped silicon as a potential intermediate band photovoltaic material

The intermediate band solar cell (IBSC) is a high-efficiency solar cell concept capable of exceeding the Schokley-Quiesser efficiency limit [96, 97]. This limit dictates that typical, single-bandgap solar cells cannot convert more than roughly 40% of concentrated sunlight (30% if not concentrated) into electricity [97]. As its name suggests and as is shown schematically in Figure 5.1, an IBSC has, in addition to a conduction band and a valence band, a third band of intermediate energy. The excita-

tion of electrons from the valence band to the intermediate band and from the intermediate band to the conduction band allows an IBSC to generate electricity from photons with energy smaller than the gap between its conduction and valence bands. Furthermore, if photocarrier lifetimes are long enough so that the intermediate band does not equilibrate with either the conduction or valence band[1], these sub-gap photons can be harvested without disturbing the collection of photons possessing a bandgap or more of energy [96, 98].

In terms of engineering parameters, an intermediate band can increase a solar cell's short-circuit current without lowering its open-circuit voltage. In order to accomplish this, the cell design must avoid making direct electrical contact to the intermediate band material. Such contact will either short the device completely (if the band is partially filled and high-mobility) or lower the open circuit voltage by reducing the device's effective bandgap. Thus, the intermediate band must always be "blocked" [99] by a layer of the host material placed between it and the metal contacts. Note that in Figure 5.1 the intermediate band material is sandwiched by a standard pn junction to accomplish this goal while aiding photocarrier extraction. If correctly blocked, the IBSC is thermodynamically equivalent to the three-junction tandem cell architecture and thus has a limiting efficiency above 60% under concentrated sun [96, 98].

Although an IBSC is easy to describe, it has proven difficult to realize. Early attempts incorporated nanocrystal quantum dots into semiconductor solar cell matrices, but this approach has not yet yielded a functioning cell [100, 101]. The first proof of concept devices have recently been fabricated using highly-mismatched alloys grown by molecular beam epitaxy (MBE) [102] and by a combination of MBE and ion implantation and

[1] If transitions from the conduction band to the intermediate band are too rapid, then it is as if the overall bandgap has shrunk. If transitions from the intermediate band to the valence band are too rapid, no sub-gap photons can be collected.

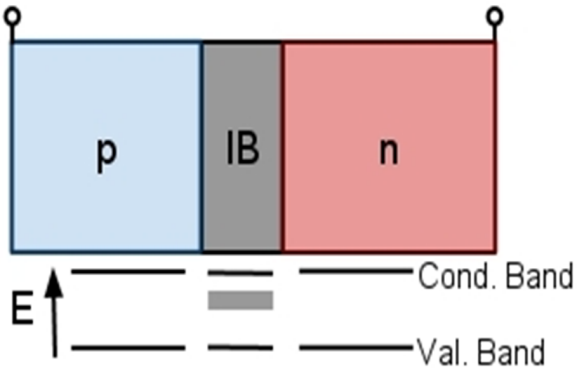

Figure 5.1: The intermediate band solar cell architecture. Note that electrical connection is made to only the conduction and valence bands.

pulsed laser melting [103]. To date, however, no one has fabricated an IBSC with an efficiency of even 1%.

Hyperdoping has the potential to provide an alternative route to the fabrication of intermediate band materials. It is well known that, at high concentrations, impurities in a semicondutor begin to interact and form delocalized, band-like states. For shallow donors and acceptors in Si, this leads to the well-known insulator-to-metal transition, which occurs when the impurity states broaden themselves and deform the conduction band enough so that the two sets of states overlap [104–106]. The hope for making intermediate band devices by hyperdoping lies with impurities known to create energy levels near mid-gap. If incorporating such impurities at high concentrations yields a sizable density of states between the conduction and valence bands without overlapping either, these states could function as an intermediate band [2].

A further critical question in this field is whether an IBSC can ever achieve efficiencies approaching its theoretical potential. At issue is the assumption that it is possible

[2]There is a surprising parallel to this effort in the field of thermoelectrics where impurities have been used to modify the band structure of materials in order to improve their thermoelectric figure of merit [107]. Unfortunately, despite considering a number of ideas during a long conversation, Eric Toberer and I were unable to find a way to apply the lessons of this thesis to his work.

to have an intermediate band that does not instantly equilibrate with either the conduction or the valence band. The standard theory of Shockley-Read-Hall (SRH) recombination [108, 109] suggests that including an intermediate band in a semiconductor should always decrease the carrier lifetime. It has been argued, however, that the states in the impurity band could be delocalized enough to invalidate the "localized state" assumption of SRH theory [110], which might in turn imply that the impurity band has, relative to its density of states, a disproportionately small effect on photocarrier recombination. The authors of Reference 110 have even claimed to observe some evidence of this effect [87]. On the other hand, Jacob Krich has argued extensively against the possibility that intermediate band devices could ever have larger than expected carrier lifetimes [88, 111]. According to Krich, a combination of Anderson localization at the tails of disorded bands [111] and phonon localization of delocalized states within any intermediate band [88] will ensure that recombination will proceed at least as fast as for localized states of the same density. As was mentioned in Section 4.2, this controversy creates the need for accurate measurements of carrier lifetime in hyperdoped materials such as those presented in that section.

While it is relatively obvious that a useful intermediate band should contribute a net positive number of photocarriers by facilitating the excitation of electrons by sub-gap light more than it accelerates the recombination of free eletrons and holes, Krich's work establishes that this need not be true for any particular materials system. It will thus be necessary to search through a wide range of intermediate-band semicnductors in order to find candidate materials with useful contributions from their extra band. Hyperdoping by ion implantation followed by nanosecond pulsed laser melting could potentially be a rapid and low-cost method for synthesizing a wide-variety of intermediate band semiconductors. Although the bandgap of silicon is substantially smaller than that of

the ideal intermediate band material [96], it is both well-understood and monatomic, making it a good test system for creating proof-of-concept fabrication procedures and devices. After reviewing the latest understanding of the effect of chalcogen hyperdoping on the the band structure of silicon, this chapter reports two recent experiments intended to adapt ion implantation and nanosecond pulsed laser melting of silicon to the unique materials challenges of fabricating intermediate-band semiconductors.

5.1 The band structure of silicon hyperdoped with chalcogens

As it became clear that hyperdoped silicon might be a useful material for IBSCs, the obvious quesiton to ask was whether hyperdoping with chalcogens, which was already well underway, could be used for this application. In order for this to be true, the chalcogen atoms would have to create a band that is 1) well-separated from the conduction and valence bands and 2) partially filled to allow transition into and out of it. Diagnosing the nature of the energy states induced by chalcogen hyperdoping of silicon turned out to be a substantial challenge because of the lack of precedent for measuring materials doped to this concentration. Too n-type for capacitive techniques and too broadly absorbing for most sophisticated optical spectroscopies, silicon hyperdoped with chalcogens required a tailored characterization approach. In parallel to this thesis and using hyperdoped silicon produced by its author, Mark Winkler and Joseph Sullivan of the Buonassisi group and Elif Ertekin of Jeffrey Grossman's group (also at MIT), led an effort to determine the band structure of silicon hyperdoped with chalcogens.

Because, as was mentioned above, doping silicon to high concentrations with highly-soluble shallow dopants leads to an insulator-to-metal transition, a natural first experiment was to check whether this ocurred in silicon hyperdoped with chalcogens as well. Beginning with his Ph.D thesis and extending to later work, Mark Winkler used

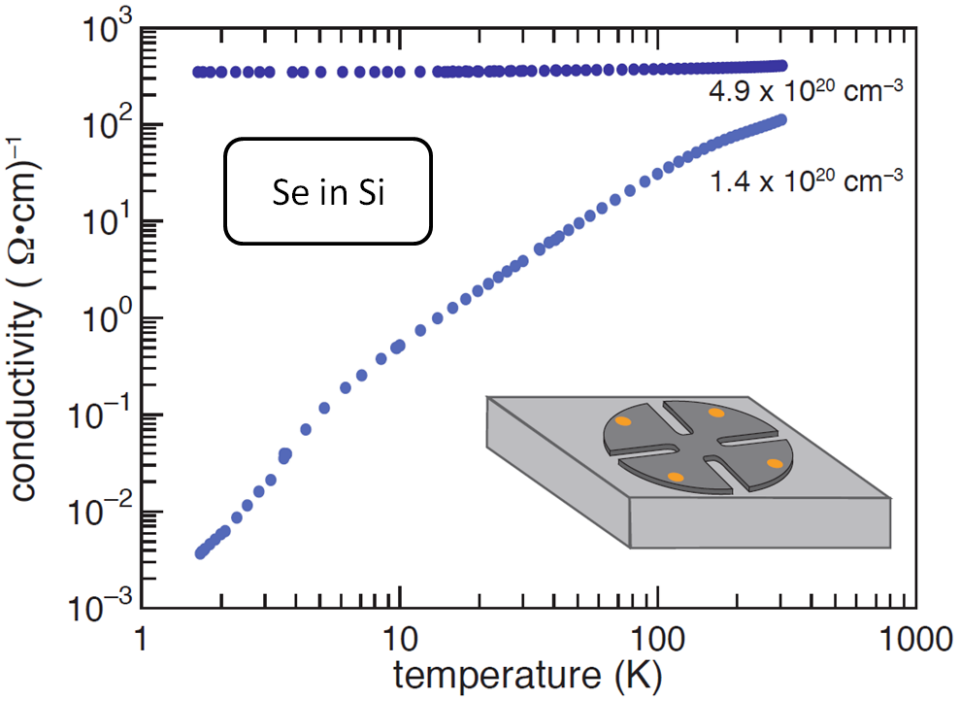

Figure 5.2: Plot of the conductivity of silicon hyperdoped with selenium derived from Hall effect measurements using the sample geometry shown. Between 1.4 and 4.9 $\times$ 10^{20} Se/cm^3 the material undergoes an insulator to metal transition evidenced by the higher concentration sample's constant conductivity down to 2 K.

temperture-dependent Hall effect studies to show that that an insulator-to-metal transition does indeed occur in silicon hyperdoped with sulfur or selenium [40, 84, 85]. His data, some of which is shown in Figure 5.2, established this result by demonstrating that the conductivity of silicon hyperdoped with a sufficient concentration of chalcogen atoms remained constant as the temperature was decreased to 2 K. Somewhat unexpectedly, however, for both elements the critical doping concentration for the transition was found to be roughly 3×10^{20} /cm^3. This is nearly two orders of magnitude larger than the concentration at which the insulator to metal transition occurs in silicon doped with boron or phosphorous [106, 112]. At concentrations slightly below the transition Winkler found signs of variable-range hopping transport [84]; at lower concentrations he observed carrier freeze-out with a donor level of roughy 120 meV [40]. While observing an insulator-to-metal transition showed conclusively that the energy states associated with the chalcogen atoms did indeed broaden, this set of experiments did little to elucidate the induced density of states beyond establishing that the low-concentration donor freeze-out energy is much smaller than the roughly 300 meV one would expect from substitutional monomers and more consistent with the energy levels observed from multi-atom complexes [37, 40].

In an attempt to measure the occupied density of states directly, Joseph Sullivan and collaborators performed soft X-ray emission spectroscopy[3] on silicon hyperdoped with sulfur [113]. Although the difficulty of interpreting X-ray emission data for hyperdoped silicon limits the scope of the conclusions that can be drawn from this experiment, Sullivan *et al.* arrived at a number of observations relevant to applying these materials to IBSCs. They found that 1) sulfur creates occupied states at energies above the valence band of silicon, 2) there is a small but clear qualitative difference in the density of states

[3] Sullivan *et al.* did attempt X-ray absorption and photoemission spectroscopy to probe the unoccupied density of states, but technical challenges have thus far stymied efforts to collect and interpret these results.

(broadening at high concentrations) between samples with concentrations above and below the insulator-to-metal transition, and 3) the distribution of states induced by the sulfur at concentrations above the insulator-to-metal transition is broad enough that some states might overlap the conduction band [113].

From early on, the featureless nature of these materials' optical absorption (see Chapter 3) had led researchers to consider the possibility that chalcogen hyperdoping created filled states that overlapped the conduction band. The lack of sub-gap photoresponse (see Chapter 4) strengthened this hypothesis since adding occupied states to the bottom the conduction band could increase optical absorption without leading to the production of harvestable photocarriers. Elif Ertekin's theoretical analysis of silicon hyperdoped with selenium put this hypothesis on a more rigorous footing while providing an accurate prediction of the optical absorption seen in Figure 3.16. As is shown in Figure 5.3, Ertekin calculated that selenium should create only filled states in silicon and that those states will overlap the conduction band and thus cause a transition to metallic conduction at concentrations of roughly 4×10^{20} cm^3. This cemented the understanding that hyperdoping silicon with chalcogens was not in itself a route to a functional intermediate band material.

Our emerging portrait of the band structure modifications induced in silicon by chalcogen hyperdoping (specifically that such doping appears to lead to the formation of a broad swath of filled states) has led to the proposal of the two strategies shown in Figure 5.4 for using hyperdoping to create a partially filled intermediate band. In the first strategy, a single dopant that creates both a filled and empty level could be included in sufficient concentration to broaden both levels to the point of overlapping, thus creating a single partially filled band of states. In the second strategy, a deep donor, such as a

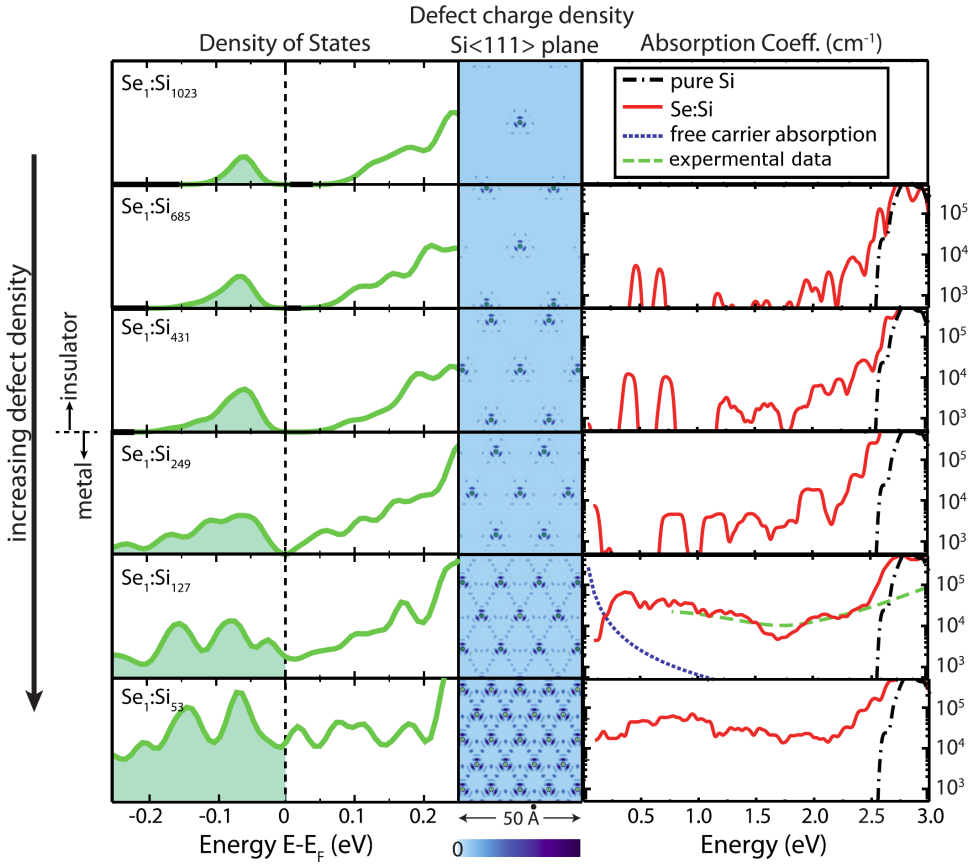

Figure 5.3: Evolution of the insulator-to-metal transition in selenium-hyperdoped silicon. Left column: the electronic density of states (referenced to the Fermi energy E_F) for a range of selenium concentrations, illustrating that the defect and conduction bands merge at $Se_1{:}Si_{249}$. The y axis is uniform for all concentrations, and the DOS is normalized so that each plot contains the same number of atoms; shaded regions indicate occupied states at $T = 0$ K. Middle column: charge density of the defect state at the Γ point, plotted on the Si $\langle 111 \rangle$ plane. Increasing dopant concentration increases interactions between neighboring defects, resulting in the eventual delocalization of the defect state. Right column: the calculated absorption coefficient arising from both direct optical transitions (for Se:Si) and free carrier absorption (for metallic Se:Si) in comparison to pure silicon. The experimentally measured absorption coefficient for $Se_1{:}Si_127$ ($\approx 4 \times 10^{20}$ Se/cm^3) is reproduced from Figure 3.16.

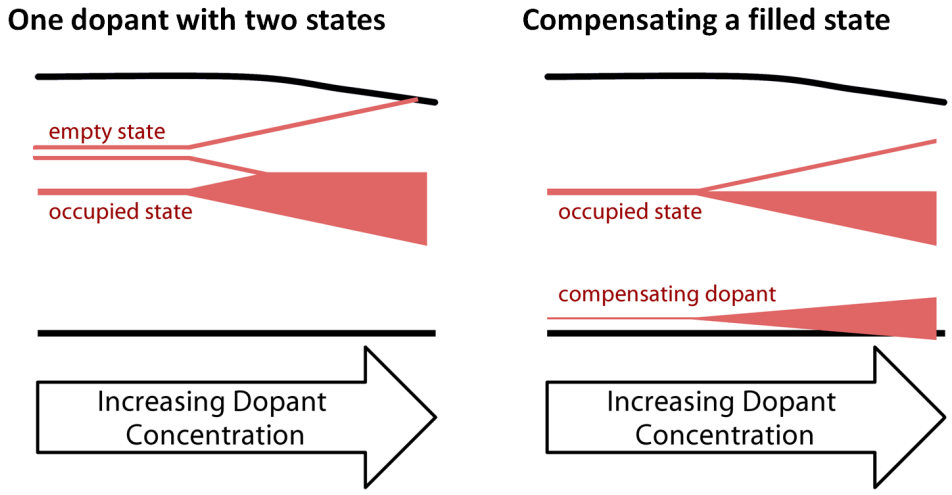

Figure 5.4: Strategies for creating a partially-occupied intermediate band by hyperdoping. Left: hypedoping with a dopant that, at low concentrations, creates both a filled and an empty state could lead to a partially-occupied intermediate band after those states broaden at high concentrations. Right: Dopants, such as the chalcogens, which create filled states can be used if they are compensated by an acceptor co-doped into the material.

chalcogen, that creates only filled states could be partially compensated by a shallow acceptor, such as boron, to create "inert" filled acceptor states and a partially occupied intermediate band. This strategy could also be implemented with a shallow donor and a deep acceptor. In all cases, care will need to be taken to ensure that concentrations remain small enough that metallic conduction due to overlap of intermediate states with the conduction or valence band does not cause an insulator to metal transition. The remainder of this chapter will focus on recent advances in hyperdoping methodology intended to facilitate the implementation of both strategies.

5.2 Controlling dopant profiles in hyperdoped silicon by modifying dopant evaporation rates during pulsed laser melting

An important aspect of IBSCs is the need to "block" the intermediate band from the charge collecting electrodes to ensure that the open-circuit voltage is determined by the largest energy gap of the intermediate band material. This can be accomplished by sandwiching the intermediate band layer within a pn-junction or between a pn-junction and a lightly-doped blocking layer, but requires that the heavily doped layer begin some distance below the device's surface [102]. Although ion implantation and nanosecond pulsed laser melting can produce single-crystal silicon with the requisite high doping levels, these techniques have never been used to form buried hyperdoped layers. Here we report a method for creating these previously inaccessible structures.

As discussed in Section 3.2, models of laser melting and rapid resolidification, and of dopant diffusion/evaporation in the melt, have been developed that can accurately predict the post-solidification dopant profile based on the as-implanted dopant profile [47,55,114]. These models have revealed that surface evaporation of high vapor pressure dopants such as sulfur and nitrogen can be significant during pulsed laser melting of

semiconductors [47, 114]. While silicon is known [115] to retain its native oxide during nanosecond laser melting, the effect of the native oxide on dopant evaporation has never been probed. Here we demonstrate that removing the surface oxide prior to pulsed laser melting significantly increases the surface evaporation rate of sulfiur from the melt and allows the formation of a buried hyperdoped layer.

750 μm thick double-side polished p-type silicon 001 wafers with resistivity 10-30 Ω-cm were ion implanted at room temperature with 95 keV $^{32}S^{+}$ to a dose of 1×10^{16} ions/cm^2. Ion-implanted samples were then irradiated with one or four pulses from a spatially homogenized, pulsed xenon chloride excimer laser (308 nm, 25 ns full width at half maximum, 50 ns pulse duration) with a square spot approximately 3×3 mm^2. A fluence of 1.7 J/cm^2 was used for the one-pulse samples and for the first three shots on the four-pulse samples. 1.8 J/cm^2 was used for the fourth shot to ensure that the final melt was the deepest. The details of the laser treatment can be found in section 3.2 and it closely resembles that used in Sections 4.1 and 4.3.

To test the effects of the native oxide on surface evaporation, some samples were oxide-etched in 10% hydrofluoric acid for 30 seconds to remove the native oxide no more than 4 hours before laser melting. The time between etching and melting was short enough that we would expect the etched samples to have an oxide that is less than half the thickness (roughly 0.2 nm) of that on the un-etched samples (roughly 1 nm) [116]. In addition, samples were melted in a variety of atmospheres: air, flowing argon, and a chamber evacuated and then back-filled with argon. Sulfur concentration depth profiles of as-implanted and laser melted samples were measured by dynamic secondary ion mass spectrometry (SIMS) using a Cameca IMS-5F instrument with a Cs^{+} primary beam.

The final sulfur concentration profiles (as measured by SIMS) of samples melted in the three atmospheres tested here were not noticeably different. Thus, the remainder of

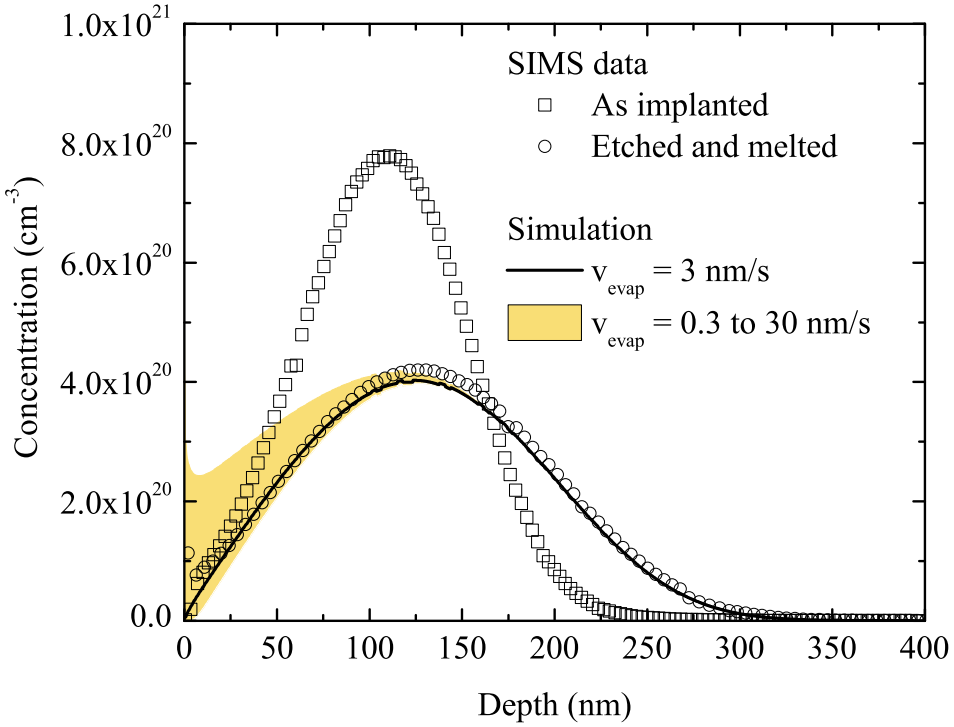

Figure 5.5: Sulfur concentration depth profile obtained by SIMS for a sample treated with HF to remove the native oxide and then melted with a single laser shot. The simulations shown use the best-fit values of the diffusivity of sulfur in liquid silicon (2.7×10^{-4} cm^2/s) and diffusive velocity (1.0 m/s). The shaded region shows the sensitivity of the simulation to changes in the surface evaporation velocity. For the lower concentration limit the surface evaporation velocity is an order of magnitude greater, and for the upper concentration limit an order of magnitude lower, than the best-fit value of 3.0 nm/s. The surface evaporation velocity of 0.3 nm/s, which leads to the upper concentration limit, is the value obtained previously [47] for a sample with a mature native oxide but otherwise nominally identical to this one. The as-implanted profile is shown for comparison.

this section will focus on the effects of etching away the native oxide. Figure 5.5 plots the sulfur concentration profiles of as-implanted material and of an etched sample melted with a single laser shot. Points within 10 nm of the surface are included for completeness, but are of substantially higher uncertainty because they were collected before steady-state sputtering conditions were reached during the SIMS measurement. Aside from oxide removal, the melted sample received the same treatment as those measured in Reference 47. Nevertheless, it is clear from Figure 5.5 that the surface concentration of sulfur in the sample that underwent oxide removal is well below the value of 3×10^{20} cm^{-3} reported in that paper (*cf.* both Figure 3.3 and their Figure 2) [47]. Figure 5.5 also shows the results of simulations of the laser melting and sulfur diffusion/evaporation processes. The best fit values (as determined by visual inspection) of the diffusivity, diffusive velocity, and surface evaporation velocity (analogous to the surface recombination velocity of charge carriers) are 2.7×10^{-4} cm^2/s, 1 m/s, and 3 nm/s, respectively. The diffusivity and diffusive velocity fits were performed over all samples, while the surface evaporation velocity fits were performed separately for the 1-shot and 4-shot samples. While the discrepancy in diffusivity between our result and the value of 1.4×10^{-4} cm^2/s reported in Reference 47 could conceivably be due to differences in the ion implanters used, it is most likely the result of measurement uncertainty. This uncertainty could exist either in the depth calibration of SIMS data by measuring the final crater depth with stylus profilometry or in the peak concentration because of the correction [117] for secondary ion counter dead-time (*i.e.* detector saturation) in the measurements reported in Reference 47.

The shaded region in Figure 5.5 indicates the sensitivity of the simulated concentration profiles to different values of the surface evaporation velocity. As can be seen from the figure, faster evaporation velocities lead to relatively small deviations toward lower

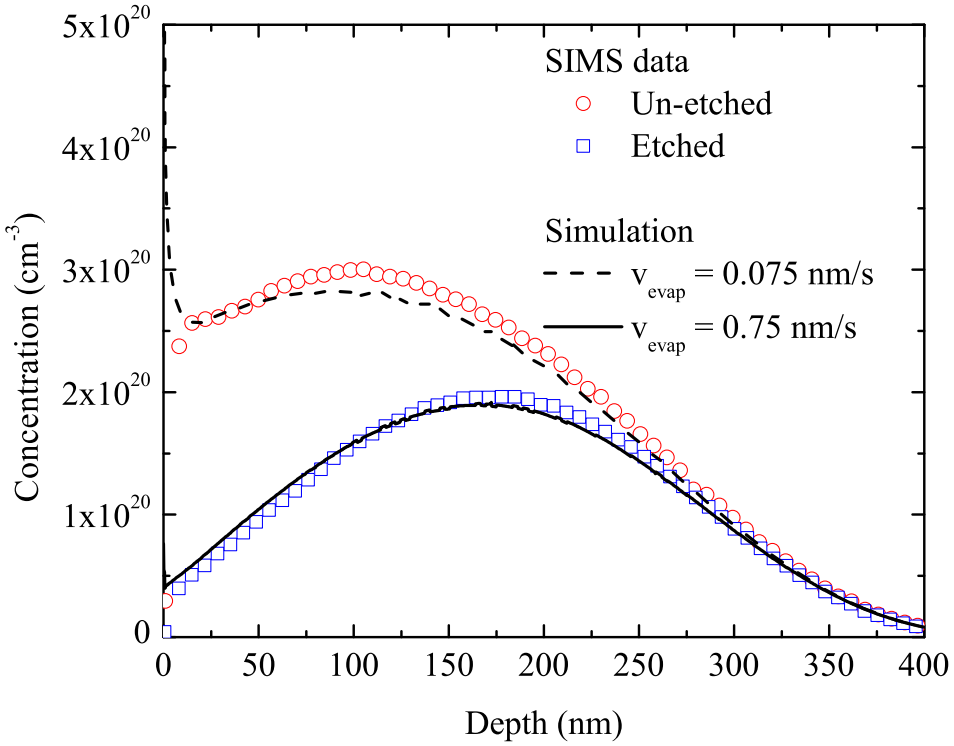

Figure 5.6: Sulfur concentration depth profiles and simulations for etched and un-etched samples melted four times by consecutive laser shots. The simulations shown use the best-fit values of the diffusivity of sulfur in liquid silicon (2.7×10^{-4} cm^2/s) and diffusive velocity (1.0 m/s). A constant surface evaporation velocity was assumed for all four melting events.

surface concentration from the best-fit profile because the best-fit velocity is fast enough to reduce the surface sulfur concentration to nearly nil. Slower evaporation velocities, however, lead to large deviations toward higher surface concentrations. A surface evaporation velocity of 0.3 nm/s (comparable to Reference 47's value of 0.27 nm/s) yields a predicted surface concentration far greater than what is observed. This indicates that etching the surface oxide causes a tenfold increase in the rate of surface evaporation relative to an un-etched sample.

Figure 5.6 compares data and simulations of the sulfur concentration profiles of sam-

ples pulsed laser melted four times with and without oxide removal. Etching the surface oxide leads to an order-of-magnitude decrease in the surface sulfur concentration and shifts the peak sulfur concentration deeper by more than 50 nm. The sample whose oxide was removed thus possesses a buried layer of hyperdoped silicon produced by ion implantation and pulsed laser melting. The best fits for the surface evaporation velocity (assuming, for simplicity, the same value for all four melting events) for the etched and un-etched samples are 0.75 nm/s and 0.075 nm/s respectively, once again demonstrating a tenfold increase in the evaporation rate due to removal of the native oxide. The value for the sample whose native oxide remained intact is consistent within experimental error with Reference 47's value of 0.054 nm/s. Comparing this to the value for the one-shot sample discussed above suggests that the surface evaporation velocity decreases with successive laser shots, possibly because of the growth of additional native oxide at the elevated surface temperatures present for a few hundred nanoseconds after melting. A similar decrease in evaporation velocity between one-and four-shot samples was reported previously [47].

The technological implications of control over the surface evaporation rate are numerous. Figures 5.5 and 5.6 indicate that the surface sulfur concentration can be lowered to such an extent that counter-doping with boron [118], for example, could easily yield a fully-compensated or p-type surface with a buried hyperdoped layer similar to that used in the first impurity band photovoltaic cell [102]. Furthermore, because of the ease with which the surface oxide may be laterally patterned, modulating surface evaporation represents a straightforward route to lateral control of the sulfur doping profile.

We have demonstrated that etching the native oxide of silicon increases tenfold the surface evaporation rate of sulfur during nanosecond pulsed laser melting. This simple method for controlling surface evaporation greatly broadens the range of doping profiles

and devices that can be fabricated using sulfur ion implantation and pulsed laser melting. As a demonstration, we have used this phenomenon to produce a buried layer of silicon hyperdoped with sulfur.

5.3 Rapid solute partitioning limits the trapping of transition metals in silicon during nanosecond pulsed laser melting but does not prevent the hyperdoping of silicon with gold

As discussed in Section 5.1, a potential strategy for producing a useful intermediate band in silicon is to incorporate a single dopant that creates both a filled and an empty level near mid-gap at a concentration high enough that those two levels overlap to form a single partially-filled band. The need for multiple mid-gap levels makes transition metal impurities, long the enemy of silicon devices for the rapid recombination such energy levels cause even at dilute concentrations, a potentially ideal choice [108,109,119]. Here we report the results of an attempt to hyperdope silicon with nine different transition metals by using ion implantation followed by nanosecond pulsed laser melting.

$^{197}Au^-$, $^{59}Co^-$, $^{52}Cr^-$, $^{63}Cu^-$, $^{56}Fe^+$, $^{184}W^+$, $^{66}Zn^-$ and the natural isotopic mixes[4] of Pd^- and Pt^- were implanted into silicon (p-type, 001, 1-10 Ω-cm) at the energies and doses listed in Table 5.1. These elements were selected using Figure 5.7 as a guide under the constraints of ion yield and ion source availability. Samples were melted with one 3×3 mm^2 pulse at 1.7 J/cm^2 from a pulsed xenon chloride excimer laser using the melting procedure described in Section 3.2. In addition, samples of silicon (n-type, 001, 5 Ω-cm and p-type, 111, 1000 Ω-cm) implanted with $^{197}Au^-$ at 50 keV to a dose of 10^{14} /cm^3 were melted with one 3×3 mm^2 pulse at 0.6 J/cm^2 from a frequency-tripled,

[4] A combination of low negative ion yields and the difficulty of mass selection at large masses motivated the experimental decision to use the natural range of masses for platinum and palladium.

Element	Dose	Energy	Breakdown?	c_{max}	v_D
Au	1×10^{16} /cm^2	325 keV	yes	5×10^{19}/cm^3	350 m/s
Co	1×10^{16} /cm^2	120 keV	yes	$< 10^{18}$/cm^3	$\gtrapprox 10^4$ m/s
Cr	5×10^{15} /cm^2	95 keV	yes	$< 10^{18}$/cm^3	$\gtrapprox 10^4$ m/s
Cu	4.5×10^{15} /cm^2	120 keV	no	$< 10^{19}$/cm^3	$\gtrapprox 10^3$ m/s
Fe	1×10^{16} /cm^2	140 keV	yes	$< 10^{20}$/cm^3	$\gtrapprox 10^2$ m/s
Fe	3×10^{15} /cm^2	140 keV	no	$< 10^{20}$/cm^3	N/A
Fe[a]	1×10^{15} /cm^2	140 keV	no	$< 10^{20}$/cm^3	N/A
Pd	5.4×10^{15} /cm^2	200 keV	yes	$< 5 \times 10^{19}$/cm^3	$\gtrapprox 10^2$ m/s
Pt	3×10^{15} /cm^2	325 keV	yes[b]	$< 10^{19}$/cm^3	$\gtrapprox 10^3$ m/s
W	1×10^{16} /cm^2	180 keV	yes[b]	$< 10^{19}$/cm^3	$\gtrapprox 10^3$ m/s
Zn	1×10^{16} /cm^2	120 keV	yes	$\approx 2 \times 10^{18}$/cm^3	$\approx 10^4$ m/s[c]

a. This sample was pre-amorphized by silicon implantation at 85 keV to a dose of 3×10^{15} /cm^3.
b. The presence of platinum and tungsten at these concentrations caused silicde formation in addition to cellular breakdown.
c. Some trapped zinc was detectable slightly above the SIMS noise floor of 10^{18}/cm^3. Though it was not possible to fit this data, it was used to derive an order of magnitude estimate of v_D.

Table 5.1: Summary of key experimental quantities and results for silicon implanted with transition metals and then melted with a xenon chloride excimer laser as described in the text. Dose and energy refer to the implantation parameters. Breakdown lists whether cellular breakdown of the solidification front was observed in transmission electron micrographs. c_{max} is the maximum incorporated concentration with the noise floor of SIMS or RBS used as a bound if no incorporation could be detected. v_D is the diffusive velocity determined by fitting concentration-depth profiles with the model described in the text where possible (only for gold) and otherwise bounded using the model and the bound on c_{max}.

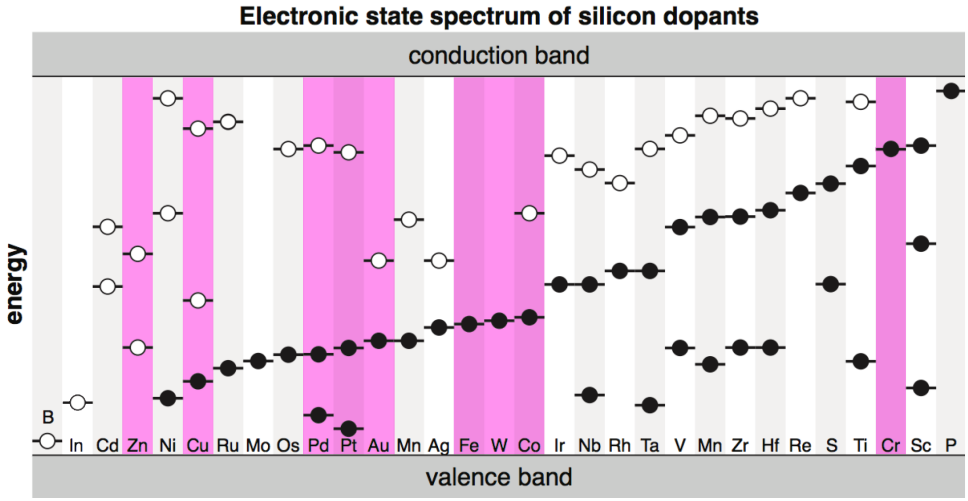

Figure 5.7: Plot of the energy levels due to dilute transition metal impurities in silicon. States which are occupied at 0 K are shown as black circles, states which are unoccupied at 0 K are shown as white circles. The metals studied in this paper are highlighted. Boron, Indium, Sulfur, and Phosphorous are included for comparison. Elements were chosen to represent a variety of energy level configurations while focusing on impurities associated with one or more mid-gap levels. Manganese is shown twice to reflect conflicting reports in the literature. Figure courtesy of Mark Winkler using data from Reference 119.

pulsed Nd:YAG laser (355 nm, 4 ns FWHM, 9 ns total duration, $\pm 20\%$ spatial intensity variation) using an otherwise identical procedure. The maximum melt depths were approximately 350 nm for the excimer laser and 150 nm for the Nd:YAG laser. Samples were examined by cross-section transmission electron microscopy (TEM). Select samples were also imaged in a scanning electron microscope (SEM) equipped with an electron backscattering diffraction (EBSD) detector. Concentration depth profiles were measured by rutherford backscattering spectrometry (RBS) for iron and tungsten[5] and by secondary ion mass spectrometry (SIMS) for all other elements. Where possible, concentration-depth profiles were fit using the model described in Sections 3.2 and 5.2 assuming no surface evaporation.

As can be seen in Table 5.1, which summarizes the results of characterization, two effects combined to disrupt hyperdoping with most of the metals studied. Cellular breakdown of the solidifcation front, a well-known phenomenon in which local freezing-point depression due to solute partitioning causes runaway amplification of small perturbations to the solidification front, occurred for many of the samples studied [120–124]. A key feature of cellular breakdown is the formation of dopant-rich walls between cells of the host semiconductor. These walls solidify more slowly than the surrounding material and thus act as sinks for impurities. As an example of a typical cellular breakdown morphology, Figure 5.8 shows electron micrographs of the sample implanted with 10^{16} $^{56}Fe^{+}$ /cm^2 and then melted. Cell walls are clearly visible, indicating that a substantial amount of dopant segregated to those regions. With diffusivities of the elements studied in liquid silicon on the order of 10^{-4} cm^2/s [125] and melt durations of roughly 150 ns, the diffusion length during solidification is approximately 50 nm. From Figure 5.8

[5] Iron's atomic mass of 56 prevents its detection in SIMS since it is obscured by the signal from the disilicon ion with the same mass. Tungsten concentration was measured by RBS as a matter of convenience.

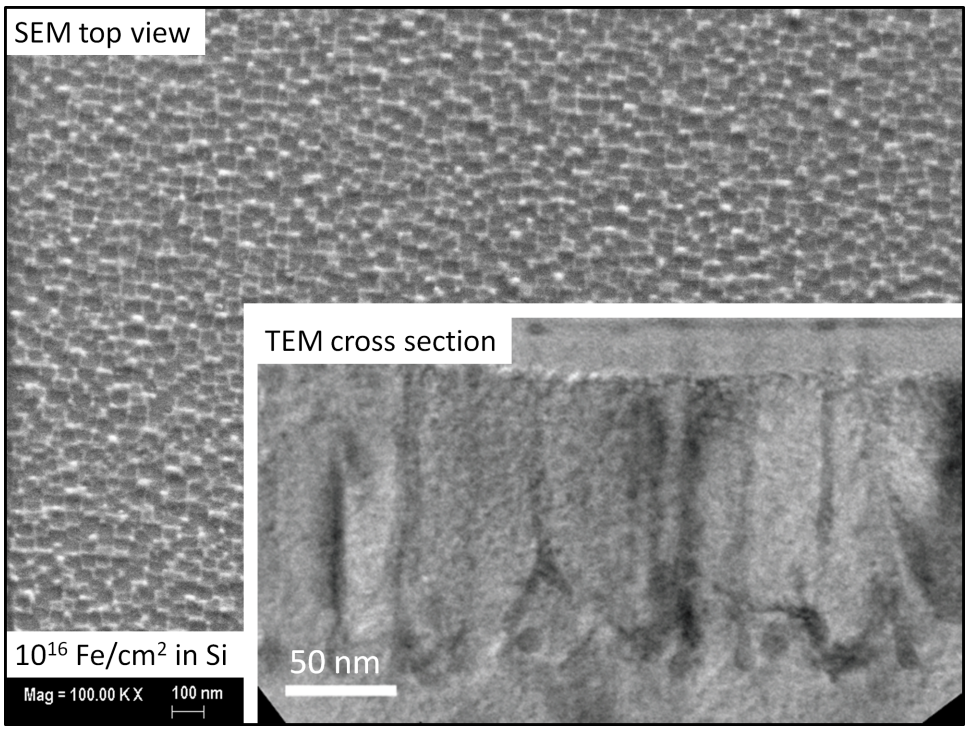

Figure 5.8: Plan-view scanning electron microscope and cross section transmission electron microscope images of silicon implanted with 10^{16} $^{56}Fe^{+}$ /cm^2 and melted with a xenon chloride excimer laser as described in the text. The appearence of cell walls in both images is clear evidence of cellular breakdown of the solidification front. Note that the cross section reveals that cell walls extend to a depth of roughly 150 nm, which is less than the melt depth. c_{max} in Table 5.1 was always reckoned at depths below the onset of breakdown.

it is clear that, at depths above the onset of breakdown, no part of the sample is more than one diffusion length from a cell wall. Accordingly, it is impossible to approximate the concentration of impurities trapped in the silicon between the cell walls from the concentration of impurities measured below the onset of breakdown. Thus the values of or bounds on $c_{\max}$ reported in Table 5.1 are reckoned at depths below the onset of breakdown.

Large diffusive velocities, v_D, posed a further challenge in fabricating silicon hyperdoped with transition metals. The diffusive velocity is the key material property governing the amount of solute partitioning during rapid solidification according to

$$k = \frac{\frac{v}{v_D} + k_e}{\frac{v}{v_D} + 1} \approx \frac{v}{v_D} + k_e, \quad v \ll v_D \tag{5.1}$$

in which k is the partition coefficient (*i.e.*, the ratio of the solute concentration in the solid to that in the liquid at the interface), k_e is the partition coefficient at equilibrium[6], and v is the solidification velocity. In most samples studied, the diffusive velocity was large enough that the maximum trapped solute concentration, $c_{\max}$, was below the detection limit of the concentration depth profiling techniques used. In addition to directly curtailing solute trapping, large values of v_D lead to a spike in solute concentration in the liquid at the solidification front due to rapid solute partitioning at the liquid-solid interface. This build-up of solute dramatically increases the probability of cellular breakdown and is likely the main reason for the frequency with which breakdown was observed in this study. Surprisingly, the values of v_D reported here for nine elements never previously measured[7] are an order of magnitude or more larger than all values of v_D previously

[6] $k_e \ll v/v_D$ in any system in which hyperdoping can occur and so k_e has been assumed to be negligible when modeling dopant diffusion and segregation in this work.

[7] A study of platinum in silicon was conducted early in the history of pulsed laser melting, but focused on depths above the onset of breakdown [126].

reported for nanosecond pulsed laser melting of silicon [31, 32, 47, 120, 121].

As can be seen in Table 5.1, gold is the only element studied for which significant hyperdoping could be demonstrated. Figure 5.9 shows a cross-section TEM image and a concentration-depth profile of the gold-doped sample described in Table 5.1. It is clear from the figure that a hyperdoped layer with thickness $>$ 100 nm formed below the depth at which cellular breakdown began. Figure 5.10 plots a fit using the simulation described in Sections 3.2 and 5.2 (assuming no surface evaporation) to the concentration depth profile for the melted material shown in Figure 5.9. The diffusivity, D, of gold in liquid silicon, fit over this sample and the two described below, was found to be 4.5×10^{-4} cm^2/s. As shown in Table 5.1, v_D was found to be 350 m/s. While this value of v_D is larger than that of any element hyperdoped into silicon previously, it is not so large as to render hyperdoping impossible. This is fortuitous given Figure 5.7, which indicates that isolated gold impurities create the filled and empty midgap energy levels required for the formation of a useful intermediate band.

Based on these promising results for gold in silicon, a preliminary effort was made to produce a breakdown-free sample of silicon hyperdoped with gold by increasing the solidification velocity to reduce the amount of solute segregation. In order to obtain an increased velocity, the laser pulse duration was reduced by a factor of ten (via the change in melting laser discussed above) and the implant and melt depths were decreased by more than a factor of two. Both of these changes were designed to increase solidification velocity by steepening the temperature gradient experienced by the sample to allow more rapid rejection of heat from the melt. In addition, both 001 and 111 silicon were tested since v_D is known to be significantly smaller in 111 silicon than in other orientations [32].

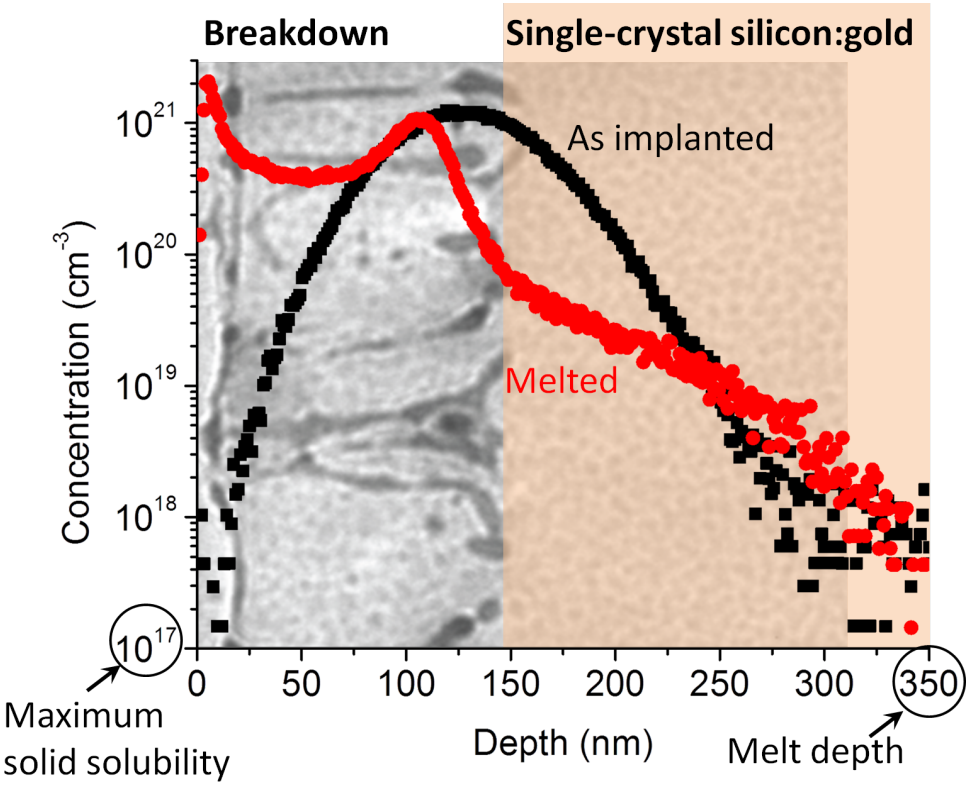

Figure 5.9: Concentration depth profile and cross section transmission electron micrograph of silicon implanted with 10^{16} $^{197}Au^{+}$ /cm² and melted with a xenon chloride excimer laser as described in the text. It is evident that gold was trapped in single-crystal silicon at concentrations up to 5×10^{19}/cm², more than two orders of magnitude above the solid solubility limit, before the onset of breakdown. Note also the shape of the concentration depth profile in the breakdown region. The subsurface peak at the abrupt beginning of a region of elevated concentration reflects the pattern of impurity enrichment of the cell walls and was common to all samples in which breakdown occurred.

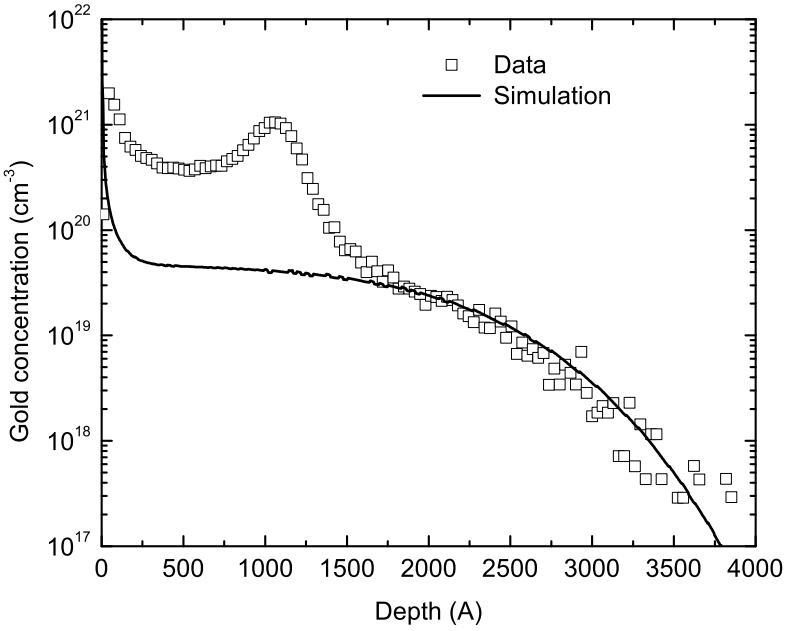

Figure 5.10: Concentration depth profile and associated simulation fit (performed over depths below the onset of cellular breakdown) for the melted sample shown in Figure 5.9. See the text for a full description of the fitting procedure.

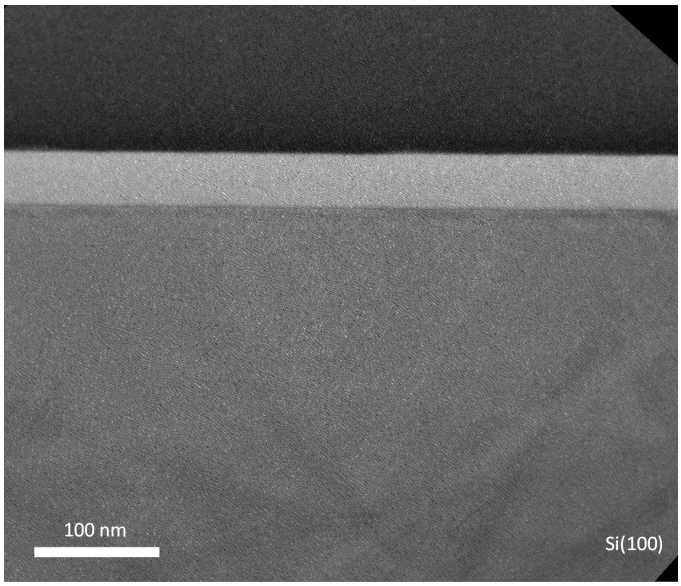

(a) Silicon 001

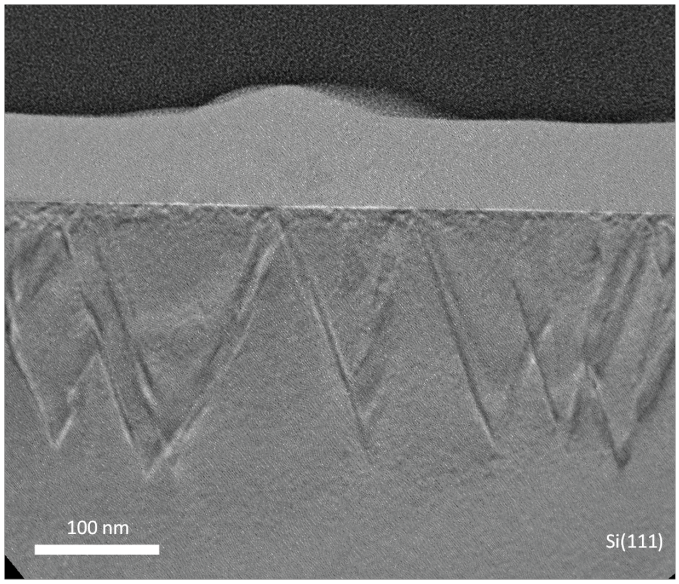

(b) Silicon 111

Figure 5.11: Cross-section transmission electron micrographs of silicon implanted with 10^{14} $^{197}Au^{-}$ /cm² and then melted with an Nd:YAG laser as described in the text. The silicon is the bottom (dark grey) section of each image and was melted from the top down. While the 001 silicon shows no sign of defects, the 111 silicon has a number of stacking faults.

Figure 5.11 shows cross-section TEM images of the 001 and 111 samples implanted with gold and melted with the Nd:YAG laser. While the 001 sample was found by both TEM and EBSD to be single-crystal and free of defects, stacking faults are clearly visible in the 111 material. The formation of stacking faults during the rapid solidification of 111 silicon is a well-known phenomenon at high solidification velocities [127, 128]. Since the stacking faults appear to have formed only near the maximum melt depth, in the region where the solidification velocity was the greatest, it may be possible to avoid their formation by slowing solidification slightly in future samples. Otherwise, such defects may render the 111 material unsuitable for device applications.

Figure 5.12 plots the concentration depth profiles and the associated simulation fits for the samples shown in Figure 5.11. As described above, $D = 4.5 \times 10^{-4}$ cm^2/s. Surprisingly, a good fit to the 001 data could not be obtained using $v_D = 350$ m/s. The best fit was instead achieved with $v_D = 110$ m/s. This discrepancy appears to be too large to be due to measurement error alone. Although accounting for this unexpected three-fold reduction in the partition coefficient is beyond the scope of this work, we note two major processing differences between the two 001 samples studied: the background doping and laser pulse spatial and temporal profiles. It is possible that either of these could have affected v_D[8]. As expected, less segregation was observed in the 111 sample. Although it is unclear how much error the stacking faults introduced into the SIMS measurement, fitting under the assumption that their influence was negligible yields $v_D = 30$ m/s. This three-fold decrease in the partition coefficient associated with the change in orientation is consistent with results for other dopants in silicon [32].

[8]The temporal profile of the laser pulse could also have influenced the best-fit value of v_D by leading to an unexpected error in the simulation of melting and solidification (described in Section 3.2) critical to fitting the final concentration profile. This simulation was tested extensively using the xenon chloride excimer laser [33], but has not been evaluated for use with the Nd:YAG laser used for these samples. An important piece of future work will be to qualify experimentally the simulation codes for use with the Nd:YAG laser.

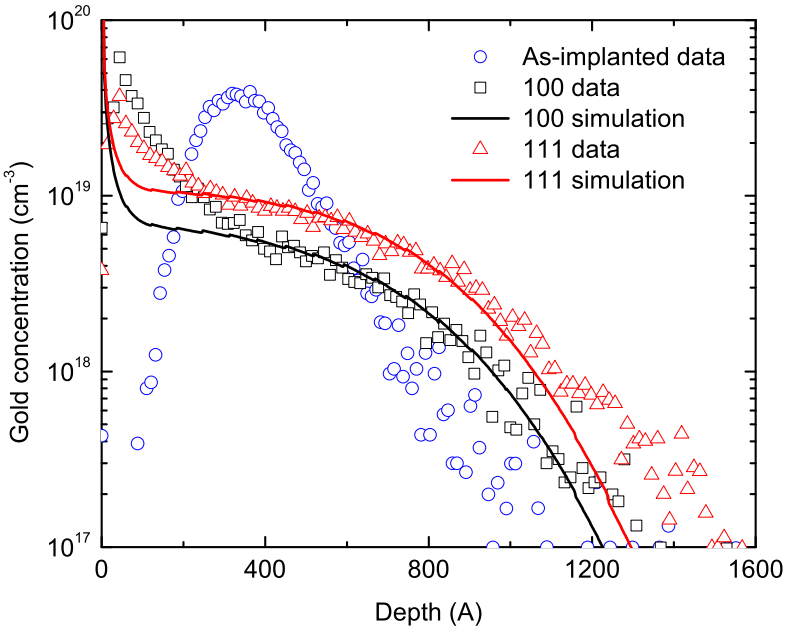

Figure 5.12: Concentration depth profiles and associated simulation fits for the samples shown in Figure 5.11. See the text for a full description of the fitting procedure. The surface concentration peak is likely broadening by the SIMS instrument of the gold segregated to the surface. Similar peaks appear for selenium and tellurium in Figure 3.11.

Figures 5.11a and 5.12 demonstrate that we have produced an approximately 100 nm thick layer of single-crystal 001 silicon that is free of extended defects and hyperdoped with gold to a concentration of roughly 10^{19} /cm^3, two orders of magnitude above the solid solubility limit. Considering the substantial reduction in dopant segregation observed relative to the sample shown in figure 5.9, it may be possible to increase the concentration of gold without inducing cellular breakdown merely by increasing the implant dose. If a further increase in concentration is desired, it could potentially be achieved while avoiding the appearance of stacking faults by using samples miscut by a few degrees from the 111 orientation or by using 111 silicon and slowing solidification slightly, perhaps by heating the sample above room temperature prior to melting [32]. One analysis [110] suggests that elements, such as gold, which create states near mid-gap in silicon should undergo a Mott insulator to metal transition at a concentration of approximately 6×10^{19} /cm^3. In theory, observing band-like conduction in the states induced by gold will require an impurity concentration above both the Mott transition and the threshold concentration for overlap between the filled and empty impurity levels. Such transport experiments (similar to those described in Section 5.1) may motivate the production of samples with higher gold concentrations than those fabricated in this study.

Setting aside the clear potential for future improvements to the hyperdoping procedure described here, we have already produced silicon hyperdoped with gold to a concentration comparable to the sulfur concentration of the 1×10^{15} S/cm^2 implanted samples discussed in Section 3.3. As can be seen in Figure 3.16, at this doping level silicon hyperdoped with sulfur displays a substantial change in optical properties. Accordingly, the natural next step will be to characterize this new material using the battery of techniques developed to study silicon hyperdoped with chalcogens and to test it as a potential active material for light detectors and photovoltaics.

6

Conclusion

This thesis has explored ways to use ion implantation and nanosecond pulsed laser melting to engineer defects in silicon, an indirect-bandgap semiconductor, that facilitate the use of this ubiquitous material in optoelectronic applications for which its unmodified band structure is not ideal. Chapter 2 considered the use of point defects as luminescence centers for light emitting diodes and demonstrated an experimental procedure capable of high-throughput screening of the electroluminescent properties of such defects. Chapter 3 discussed the dramatic change in optical absorption observed

in silicon hyperdoped with chalcogens and reported the first measurements of the optical absorption of such materials for photon energies greater than the bandgap of silicon. Chapter 4 examined the use of silicon hyperdoped with chalcogens in light detectors and concluded that while these devices display strong internal gain which is coupled to a particular type of surface defect, hyperdoping does not lead directly to measurable sub-gap photoconductivity. Chapter 5 discussed the potential for silicon to serve as an intermediate-band semiconductor and reported experimental progress on two proposed approaches for hyperdoping silicon so that it displays this highly desired but rarely observed property.

In addition to the extensions to experiments discussed in this thesis that were presented in previous chapters, there are a number of opportunities for future studies that emerge from a consideration of this work as a whole.

An important experimental development in Section 5.3 is the use of an Nd:YAG laser with a 4 ns pulse duration for pulsed laser melting. As discussed in that chapter, this laser's shorter pulse duration facilitated more solute trapping and thus a greater degree of hyperdoping than the xenon chloride excimer laser typically used. However, the coherence of the Nd:YAG laser beam makes it much harder to homogenize than that of the excimer laser. In the work reported here, the spatial intensity variation of the Nd:YAG laser was acceptable, but it may be necessary to homogenize its beam to improve reproducibility and surface quality in future melting applications. This may prove to be a formidable undertaking.

As devices made from new hyperdoped materials, such as are described in Section 5.3, are produced and studied, it will be important to separate the effects of the material itself from that of the device architecture. Even though the gain described in Sections 4.1 and 4.3 may ultimately prove to be a desirable feature of hyperdoped silicon devices, it could

easily complicate the interpretation of spectral response data. Accordingly, establishing control over the defects described in Section 4.3 in order both to suppress and create them could be required for future work. It may be that the best device structure is free of surface defects but harnesses the gain mechanism described in Section 4.3 by using a metal-semiconductor-metal architecture such as that described in Reference [92].

There may also be an opportunity to combine some of the work described in Chapters 2 and 5. The band structure modifications that can be implemented by hyperdoping need not be limited to use in optical absorption. They may be applicable to light emission as well. It might be possible to append impurity states onto the bottom of the conduction band and the top of the valence band so that direct, radiative transitions can occur between them. In this way, silicon could potentially be modified to display the luminescent properties of a direct-gap semiconductor. This was one motivation for the inclusion of chromium in the study described in Section 5.3. It was thought that it might serve as a potential donor complement to the acceptor states created by indium, which is readily hyperdoped into silicon [129]. Even though chromium proved difficult to incorporate, the overall idea may still be valid. If such a scheme is combined with techniques such as those described in Section 5.2 for creating buried hyperdoped layers, it may even be possible to improve luminescence by establishing quantum confinement to the hyperdoped region.

The previous idea also begins to address the possibility of unexpected properties emerging in silicon (or other semiconductors) hyperdoped with two elements at once. Although this thesis has been limited to the study of silicon hyperdoped with a single element, there is no fundamental reason for so restricting the range of possible materials. While the mechanism by which cellular breakdown of the solidification front occurs would likely respond to the total amount of dopant regardless of species, this

limits but does not preclude the use of multiple doping elements. The co-doping route to a useful intermediate band proposed in Section 5.1 is one example of two-element hyperdoping, but it explicitly bets on a lack of unexpected properties. Systematic explorations of single elements hyperdoped into silicon might thus be well-complemented by broad, combinatorial experiments with multiple-element hyperdoping. Such studies could both discover novel properties and interactions and establish pairs of dopants that could be used in concert without interfering with each other.

Although silicon is often considered to be a well-understood material with clearly defined bounds on its applicability, defect engineering by energetic beam processing has the potential to grant silicon a range of new and useful properties. If this processing can deliver on its promise of tailorable and vastly improved optoelectronic properties, silicon may prove to be one of the high-performance, multifunctional materials of the future, in addition to being one of the great materials science achievements of the past.

Included publications

Chapter 2 includes:

- D. Recht, F. Capasso, and M. Aziz, "On the temperature dependence of point-defect-mediated luminescence in silicon," *Applied Physics Letters*, vol. 94, p. 251113, 2009
- As yet unpublished work led by Supakit Charnvanichborikarn and Patrick Parkinson under the guidance of Professor James Williams with significant intellectual and experimental contributions from DR.

Chapter 3 includes:

- S. Pan, D. Recht, S. Charnvanichborikarn, J. Williams, and M. Aziz, "Enhanced visible and near-infrared optical absorption in silicon supersaturated with chalcogens," *Applied Physics Letters*, vol. 98, p. 121913, 2011

Chapter 4 includes:

- A. Said, D. Recht, J. Sullivan, J. Warrender, T. Buonassisi, P. Persans, and M. Aziz, "Extended infrared photoresponse and gain in chalcogen-supersaturated silicon photodiodes," *Applied Physics Letters*, vol. 99, p. 073503, 2011
- D. Recht, D. Hutchinson, T. Cruson, A. DiFranzo, A. McAllister, A. Said, J. Warrender, P. Persans, and M. Aziz, "Contactless microwave measurements of photoconductivity in silicon hyperdoped with chalcogens," *Applied Physics Express*, vol. 5, no. 4, p. 041301, 2012
- As yet unpublished work led by DR with major experimental contributions from David Hutchinson under the guidance of Professor Peter Persans, Joseph Sullivan under the guidance of Professor Tonio Buonassisi, and Aurore Said under the guidance of Professor Michael Aziz

Chapter 5 includes:

- A summary discussion of M. Winkler, D. Recht, M. Sher, A. Said, E. Mazur, and M. Aziz, "Insulator-to-metal transition in sulfur-doped silicon," *Physical Review Letters*, vol. 106, p. 178701, Apr 2011

- A summary discussion of E. Ertekin, M. Winkler, D. Recht, A. Said, M. Aziz, T. Buonassisi, and J. Grossman, "Insulator-to-metal transition in selenium-hyperdoped silicon: observation and origin," *Physical Review Letters*, vol. 108, p. 026401, Jan 2012
- D. Recht, J. Sullivan, R. Reedy, T. Buonassisi, and M. Aziz, "Controlling dopant profiles in hyperdoped silicon by modifying dopant evaporation rates during pulsed laser melting," *Applied Physics Letters*, vol. 100, no. 11, p. 112112, 2012
- As yet unpublished work led by DR with major experimental contributions from Matthew Smith under the guidance of Professor Silvija Gradecak and Supakit Charnvanichborikarn under the guidance of Professor James Williams.

References

[1] M. Schulz, "The end of the road for silicon," *Nature*, vol. 399, no. 6738, pp. 729–730, 1999.

[2] A. Lidow, "Is it the end of the road for silicon in power conversion?," in *Integrated Power Electronics Systems (CIPS), 2010 6th International Conference on*, pp. 1–8, IEEE, 2010.

[3] J. Markoff, "A high-stakes search continues for silicon's successor," *The New York Times*, December 11 2011.

[4] J. Shainline and J. Xu, "Silicon as an emissive optical medium," *Laser & Photonics Reviews*, vol. 1, no. 4, pp. 334–348, 2007.

[5] J. Bao, M. Tabbal, T. Kim, S. Charnvanichborikarn, J. Williams, M. Aziz, F. Capasso, *et al.*, "Point defect engineered Si sub-bandgap light-emitting diode," *Optics Express*, vol. 15, p. 6727, 2007.

[6] S. Cloutier, P. Kossyrev, and J. Xu, "Optical gain and stimulated emission in periodic nanopatterned crystalline silicon," *Nature Materials*, vol. 4, no. 12, pp. 887–891, 2005.

[7] E. Rotem, J. Shainline, and J. Xu, "Enhanced photoluminescence from nanopatterned carbon-rich silicon grown by solid-phase epitaxy," *Applied Physics Letters*, vol. 91, p. 051127, 2007.

[8] P. Giri, "Photoluminescence signature of silicon interstitial cluster evolution from compact to extended structures in ion-implanted silicon," *Semiconductor Science and Technology*, vol. 20, p. 638, 2005.

[9] G. Davies, H. Brian, E. Lightowlers, K. Barraclough, and M. Thomaz, "The temperature dependence of the 969 meV "G" optical transition in silicon," *Semiconductor Science and Technology*, vol. 4, p. 200, 1989.

[10] R. Pierret, *Semiconductor Device Fundamentals*. Addison-Wesley, 1996.

[11] A. Kenyon, "Erbium in silicon," *Semiconductor Science and Technology*, vol. 20, p. R65, 2005.

[12] B. Zheng, J. Michel, F. Ren, L. Kimerling, D. Jacobson, and J. Poate, "Room-temperature sharp line electroluminescence at λ= 1.54 μm from an erbium-doped, silicon light-emitting diode," *Applied Physics Letters*, vol. 64, no. 21, pp. 2842–2844, 1994.

[13] J. Zhang, X. Wang, B. Cheng, J. Yu, Q. Wang, J. Hau, L. Ding, and W. Ge, "Enhanced near-infrared photoluminescence from isoelectronic luminescent centers in sulfur-implanted silicon with copper or silver coimplantation," *Applied physics letters*, vol. 90, p. 081101, 2007.

[14] K. Homewood, M. Lourenco, and R. Gwilliam, "1.1 to 1.6 μm silicon light emitting diodes and optical gain," in *Group IV Photonics (GFP), 2010 7th IEEE International Conference on*, pp. 302–304, IEEE, 2010.

[15] M. Lourenco, L. Wong, R. Gwilliam, and K. Homewood, "Luminescence of Tm^{3+} in dislocation engineered silicon substrates," in *Group IV Photonics (GFP), 2010 7th IEEE International Conference on*, pp. 159–161, IEEE, 2010.

[16] W. Ng, M. Lourenco, R. Gwilliam, S. Ledain, G. Shao, and K. Homewood, "An efficient room-temperature silicon-based light-emitting diode," *Nature*, vol. 410, no. 6825, pp. 192–194, 2001.

[17] J. Sun, M. Helm, W. Skorupa, B. Schmidt, and A. Mücklich, "Highly efficient silicon light emitting diodes produced by doping engineering," *Frontiers of Optoelectronics in China*, pp. 1–6, 2012.

[18] D. Liang and J. Bowers, "Recent progress in lasers on silicon," *Nature Photonics*, vol. 4, no. 8, pp. 511–517, 2010.

[19] L. Pavesi, "A review of the various efforts to a silicon laser," *Photonics Packaging and Integration III*, vol. 4997, pp. 206–220, 2003.

[20] M. Giantomassi, M. Stankovski, R. Shaltaf, M. Grüning, F. Bruneval, P. Rinke, and G. Rignanese, "Electronic properties of interfaces and defects from many-body perturbation theory: Recent developments and applications," *Physica Status Solidi (b)*, vol. 248, no. 2, pp. 275–289, 2011.

[21] L. Yu and A. Zunger, "Identification of potential photovoltaic absorbers based on first-principles spectroscopic screening of materials," *Physical Review Letters*, vol. 108, no. 6, p. 068701, 2012.

[22] R. Potyrailo, K. Rajan, K. Stowe, I. Takeuchi, B. Chisholm, and H. Lam, "Combinatorial and high-throughput screening of materials libraries: Review of state of the art," *ACS Combinatorial Science*, 2011.

[23] B. Lee, S. Lee, H. Jeong, and K. Sohn, "Solid-state combinatorial screening of (Sr, Ca, Ba, Mg)$_2$Si$_5$N$_8$: Eu^{2+} phosphors," *ACS Combinatorial Science*, 2011.

[24] S. Charnvanichborikarn, B. Villis, B. Johnson, J. Wong-Leung, J. McCallum, J. Williams, and C. Jagadish, "Effect of boron on interstitial-related luminescence centers in silicon," *Applied Physics Letters*, vol. 96, p. 051906, 2010.

[25] J. Ziegler, M. Ziegler, and J. Biersack, "SRIM-the stopping and range of ions in matter (2010)," *Nuclear Instruments and Methods in Physics Research Section B: Beam Interactions with Materials and Atoms*, vol. 268, no. 11-12, pp. 1818–1823, 2010.

[26] N. Giammarco and G. Kaplita, "Reactive ion etching apparatus," June 1986. US Patent 4,595,484.

[27] D. Thomas, P. Southworth, M. Flowers, and R. Greef, "An investigation of the roughening of silicon (100) surfaces in Cl_2 reactive ion etching plasmas by in situ ellipsometry and quadrupole mass spectrometry," *Journal of Vacuum Science & Technology B: Microelectronics and Nanometer Structures*, vol. 7, no. 6, pp. 1325–1332, 1989.

[28] G. Oehrlein, J. Rembetski, and E. Payne, "Study of sidewall passivation and microscopic silicon roughness phenomena in chlorine-based reactive ion etching of silicon trenches," *Journal of Vacuum Science & Technology B: Microelectronics and Nanometer Structures*, vol. 8, no. 6, pp. 1199–1211, 1990.

[29] P. Carey, T. Sigmon, R. Press, and T. Fahlen, "Ultra-shallow high-concentration boron profiles for CMOS processing," *Electron Device Letters, IEEE*, vol. 6, no. 6, pp. 291–293, 1985.

[30] P. Carey, K. Bezjian, T. Sigmon, P. Gildea, and T. Magee, "Fabrication of submicrometer mosfet's using gas immersion laser doping (GILD)," *Electron Device Letters, IEEE*, vol. 7, no. 7, pp. 440–442, 1986.

[31] L. Goldman and M. Aziz, "Aperiodic stepwise growth model for the velocity and orientation dependence of solute trapping," *J. Mater. Res*, vol. 2, no. 4, p. 524, 1987.

[32] R. Reitano, P. Smith, and M. Aziz, "Solute trapping of group III, IV, and V elements in silicon by an aperiodic stepwise growth mechanism," *Journal of Applied Physics*, vol. 76, no. 3, pp. 1518–1529, 1994.

[33] J. Kittl, P. Sanders, M. Aziz, D. Brunco, and M. Thompson, "Complete experimental test of kinetic models for rapid alloy solidification," *Acta Materialia*, vol. 48, no. 20, pp. 4797–4811, 2000.

[34] T. Her, R. Finlay, C. Wu, S. Deliwala, and E. Mazur, "Microstructuring of silicon with femtosecond laser pulses," *Applied Physics Letters*, vol. 73, p. 1673, 1998.

[35] T. Her, R. Finlay, C. Wu, and E. Mazur, "Femtosecond laser-induced formation of spikes on silicon," *Applied Physics A: Materials Science & Processing*, vol. 70, no. 4, pp. 383–385, 2000.

[36] C. Wu, C. Crouch, L. Zhao, J. Carey, R. Younkin, J. Levinson, E. Mazur, R. Farrell, P. Gothoskar, and A. Karger, "Near-unity below-band-gap absorption by microstructured silicon," *Applied Physics Letters*, vol. 78, p. 1850, 2001.

[37] E. Janzen, R. Stedman, G. Grossmann, and H. Grimmeiss, "High-resolution studies of sulfur-and selenium-related donor centers in silicon," *Physical Review B*, vol. 29, no. 4, p. 1907, 1984.

[38] R. Younkin, J. Carey, E. Mazur, J. Levinson, and C. Friend, "Infrared absorption by conical silicon microstructures made in a variety of background gases using femtosecond-laser pulses," *Journal of Applied Physics*, vol. 93, p. 2626, 2003.

[39] M. Sheehy, L. Winston, J. Carey, C. Friend, and E. Mazur, "Role of the background gas in the morphology and optical properties of laser-microstructured silicon," *Chemistry of Materials*, vol. 17, no. 14, pp. 3582–3586, 2005.

[40] M. Winkler, *Non-Equilbrium Chalcogen Concentrations in Silicon: Physical Structure, Electronic Transport, and Photovoltaic Potential*. PhD thesis, Harvard University Cambridge, Massachusetts, 2009.

[41] C. Crouch, J. Carey, J. Warrender, M. Aziz, E. Mazur, and F. Génin, "Comparison of structure and properties of femtosecond and nanosecond laser-structured silicon," *Applied Physics Letters*, vol. 84, p. 1850, 2004.

[42] T. Kim, J. Warrender, and M. Aziz, "Strong sub-band-gap infrared absorption in silicon supersaturated with sulfur," *Applied Physics Letters*, vol. 88, p. 241902, 2006.

[43] M. Tabbal, M. Aziz, C. Madi, S. Charnvanichborikarn, J. Williams, and T. Christidis, "Excimer laser processing of novel materials for optoelectronic and spintronic applications," in *Proceedings of SPIE*, vol. 6458, p. 645803, 2007.

[44] M. Sheehy, B. Tull, C. Friend, and E. Mazur, "Chalcogen doping of silicon via intense femtosecond-laser irradiation," *Materials Science and Engineering: B*, vol. 137, no. 1-3, pp. 289–294, 2007.

[45] B. Tull, M. Winkler, and E. Mazur, "The role of diffusion in broadband infrared absorption in chalcogen-doped silicon," *Applied Physics A: Materials Science & Processing*, vol. 96, no. 2, pp. 327–334, 2009.

[46] M. Smith, M. Winkler, M. Sher, Y. Lin, E. Mazur, and S. Gradečak, "The effects of a thin film dopant precursor on the structure and properties of femtosecond-laser irradiated silicon," *Applied Physics A: Materials Science & Processing*, pp. 1–6, 2011.

[47] B. Bob, A. Kohno, S. Charnvanichborikarn, J. Warrender, I. Umezu, M. Tabbal, J. Williams, and M. Aziz, "Fabrication and subband gap optical properties of silicon supersaturated with chalcogens by ion implantation and pulsed laser melting," *Journal of Applied Physics*, vol. 107, no. 12, pp. 123506–123506, 2010.

[48] M. Tabbal, T. Kim, D. Woolf, B. Shin, and M. Aziz, "Fabrication and sub-band-gap absorption of single-crystal Si supersaturated with Se by pulsed laser mixing," *Applied Physics A: Materials Science & Processing*, vol. 98, no. 3, pp. 589–594, 2010.

[49] B. Newman, J. Sullivan, M. Winkler, M. Sher, M. Marcus, M. Smith, S. Gradecak, E. Mazur, and T. Buonassisi, "Illuminating the mechanism for subbandgap absorption in chalcogen doped silicon materials for PV applications," in *European Union Photovoltaic Solar Energy Conference,(Hamburg, Germany)*, 2009.

[50] C. Simmons, "Private communication." 2012.

[51] B. Newman, M. Sher, E. Mazur, and T. Buonassisi, "Reactivation of sub-bandgap absorption in chalcogen-hyperdoped silicon," *Applied Physics Letters*, vol. 98, p. 251905, 2011.

[52] I. Umezu, A. Kohno, J. M. Warrender, Y. Takatori, Y. Hirao, S. Nakagawa, A. Sugimura, S. Charnvanichborikarn, J. S. Williams, and M. J. Aziz, "Strong mid-infrared optical absorption by supersaturated sulfur doping in silicon," *AIP Conference Proceedings*, vol. 1399, no. 1, pp. 51–52, 2011.

[53] M. Sher, M. Winkler, and E. Mazur, "Pulsed-laser hyperdoping and surface texturing for photovoltaics," *MRS bulletin*, vol. 36, no. 06, pp. 439–445, 2011.

[54] K. Watanabe, M. Miyao, I. Takemoto, and N. Hashimoto, "Ellipsometric study of silicon implanted with boron ions in low doses," *Applied Physics Letters*, vol. 34, p. 518, 1979.

[55] T. Kim, M. Pillai, M. Aziz, M. Scarpulla, O. Dubon, K. Yu, J. Beeman, and M. Ridgway, "Heat flow model for pulsed laser melting and rapid solidification of ion implanted gaas," *Journal of Applied Physics*, vol. 108, no. 1, pp. 013508–013508, 2010.

[56] M. Aziz, J. Tsao, M. Thompson, P. Peercy, and C. White, "Solute trapping: Comparison of theory with experiment," *Physical review letters*, vol. 56, no. 23, pp. 2489–2492, 1986.

[57] R. Carlson, R. Hall, and E. Pell, "Sulfur in silicon," *Journal of Physics and Chemistry of Solids*, vol. 8, no. 0, pp. 81 – 83, 1959.

[58] R. Wilson, "Depth distributions of sulfur implanted into silicon as a function of ion energy, ion fluence, and anneal temperature," *Journal of Applied Physics*, vol. 55, no. 10, pp. 3490–3494, 1984.

[59] P. Schmid, "Optical absorption in heavily doped silicon," *Physical Review B*, vol. 23, no. 10, p. 5531, 1981.

[60] R. Swanepoel, "Determination of the thickness and optical constants of amorphous silicon," *Journal of Physics E: Scientific Instruments*, vol. 16, p. 1214, 1983.

[61] C. Herzinger and B. Johs, "Dielectric function parametric model, and method of use," August 1998. US Patent 5,796,983.

[62] C. Herzinger, B. Johs, W. McGahan, J. Woollam, and W. Paulson, "Ellipsometric determination of optical constants for silicon and thermally grown silicon dioxide via a multi-sample, multi-wavelength, multi-angle investigation," *Journal of Applied Physics*, vol. 83, p. 3323, 1998.

[63] R. Schropp and M. Zeman, *Amorphous and Microcrystalline Silicon Solar Cells: Modeling, Materials, and Device Technology*, vol. 5. Springer, 1998.

[64] R. Myers, R. Farrell, A. Karger, J. Carey, and E. Mazur, "Enhancing near-infrared avalanche photodiode performance by femtosecond laser microstructuring," *Applied Optics*, vol. 45, no. 35, pp. 8825–8831, 2006.

[65] J. Carey, C. Crouch, M. Shen, and E. Mazur, "Visible and near-infrared responsivity of femtosecond-laser microstructured silicon photodiodes," *Optics Letters*, vol. 30, no. 14, pp. 1773–1775, 2005.

[66] M. Pralle and J. Carey, "Black silicon enhanced thin film silicon photovoltaic devices," tech. rep., SiOnyx, Inc., http://www.osti.gov/bridge/servlets/purl/984305-lyoWxh/984305.pdf, 2010.

[67] M. Pralle, J. Carey, H. Homayoon, S. Alie, J. Sickler, X. Li, J. Jiang, D. Miller, C. Palsule, and J. McKee, "Black silicon enhanced photodetectors: a path to IR CMOS," in *Proceedings of SPIE*, vol. 7660, p. 76600N, 2010.

[68] M. Pralle, J. Carey, H. Homayoon, J. Sickler, X. Li, J. Jiang, D. Miller, C. Palsule, and J. McKee, "IR CMOS: ultrafast laser-enhanced silicon detection," in *Proceedings of SPIE*, vol. 8012, p. 801222, 2011.

[69] X. Li, J. Carey, J. Sickler, M. Pralle, C. Palsule, and C. Vineis, "Silicon photodiodes with high photoconductive gain at room temperature," *Optics Express*, vol. 20, no. 5, pp. 5518–5523, 2012.

[70] R. Young, J. Narayan, and R. Wood, "Electrical and structural characteristics of laser-induced epitaxial layers in silicon," *Applied Physics Letters*, vol. 35, no. 6, pp. 447–449, 1979.

[71] C. Chang, C. Hu, and R. Brodersen, "Quantum yield of electron impact ionization in silicon," *Journal of Applied Physics*, vol. 57, no. 2, pp. 302–309, 1985.

[72] C. Jacoboni, C. Canali, G. Ottaviani, and A. Alberigi Quaranta, "A review of some charge transport properties of silicon," *Solid-State Electronics*, vol. 20, no. 2, pp. 77–89, 1977.

[73] B. Kochman, A. Stiff-Roberts, S. Chakrabarti, J. Phillips, S. Krishna, J. Singh, and P. Bhattacharya, "Absorption, carrier lifetime, and gain in inas-gaas quantum-dot infrared photodetectors," *Quantum Electronics, IEEE Journal of*, vol. 39, no. 3, pp. 459–467, 2003.

[74] H. Lim, B. Movaghar, S. Tsao, M. Taguchi, W. Zhang, A. Quivy, and M. Razeghi, "Gain and recombination dynamics of quantum-dot infrared photodetectors," *Physical Review B*, vol. 74, no. 20, p. 205321, 2006.

[75] A. Chantre, "Introduction to defect bistability," *Applied Physics A: Materials Science & Processing*, vol. 48, no. 1, pp. 3–9, 1989.

[76] R. Czaputa, "Transition metal impurities in silicon: New defect reactions," *Applied Physics A: Materials Science & Processing*, vol. 49, no. 4, pp. 431–436, 1989.

[77] S. Deb and B. Nag, "Measurement of lifetime of carriers in semiconductors through microwave reflection," *Journal of Applied Physics*, vol. 33, no. 4, pp. 1604–1604, 1962.

[78] J. Holm and K. Champlin, "Microwave conductivity of silicon and germanium," *Journal of Applied Physics*, vol. 39, no. 1, pp. 275–284, 1968.

[79] J. Eikelboom, C. Leguijt, C. Frumau, and A. Burgers, "Microwave detection of minority carriers in solar cell silicon wafers," *Solar energy materials and solar cells*, vol. 36, no. 2, pp. 169–185, 1995.

[80] R. Ahrenkiel and S. Johnston, "Lifetime analysis of silicon solar cells by microwave reflection," *Solar Energy Materials and Solar Cells*, vol. 92, no. 8, pp. 830–835, 2008.

[81] J. Borrego, R. Gutmann, N. Jensen, and O. Paz, "Non-destructive lifetime measurement in silicon wafers by microwave reflection," *Solid-State Electronics*, vol. 30, no. 2, pp. 195–203, 1987.

[82] R. Sinton and A. Cuevas, "Contactless determination of current–voltage characteristics and minority-carrier lifetimes in semiconductors from quasi-steady-state photoconductance data," *Applied Physics Letters*, vol. 69, no. 17, pp. 2510–2512, 1996.

[83] M. Afsar and H. Chi, "Millimeter wave complex refractive index, complex dielectric permittivity and loss tangent of extra high purity and compensated silicon," *International Journal of Infrared and Millimeter Waves*, vol. 15, no. 7, pp. 1181–1188, 1994.

[84] M. Winkler, D. Recht, M. Sher, A. Said, E. Mazur, and M. Aziz, "Insulator-to-metal transition in sulfur-doped silicon," *Physical Review Letters*, vol. 106, p. 178701, Apr 2011.

[85] E. Ertekin, M. Winkler, D. Recht, A. Said, M. Aziz, T. Buonassisi, and J. Grossman, "Insulator-to-metal transition in selenium-hyperdoped silicon: observation and origin," *Physical Review Letters*, vol. 108, p. 026401, Jan 2012.

[86] J. Fossum, R. Mertens, D. Lee, and J. Nijs, "Carrier recombination and lifetime in highly doped silicon," *Solid-State Electronics*, vol. 26, no. 6, pp. 569 – 576, 1983.

[87] E. Antolin, A. Marti, J. Olea, D. Pastor, G. González-Diaz, I. Mártil, and A. Luque, "Lifetime recovery in ultrahighly titanium-doped silicon for the implementation of an intermediate band material," *Applied Physics Letters*, vol. 94, no. 4, p. 042115, 2009.

[88] J. Krich, B. Halperin, and A. Aspuru-Guzik, "Nonradiative lifetimes in intermediate band materials-absence of lifetime recovery," *Arxiv preprint arXiv:1110.5639*, 2011.

[89] A. Said, D. Recht, J. Sullivan, J. Warrender, T. Buonassisi, P. Persans, and M. Aziz, "Extended infrared photoresponse and gain in chalcogen-supersaturated silicon photodiodes," *Applied Physics Letters*, vol. 99, p. 073503, 2011.

[90] J. Burm and L. Eastman, "Low-frequency gain in msm photodiodes due to charge accumulation and image force lowering," *Photonics Technology Letters, IEEE*, vol. 8, no. 1, pp. 113–115, 1996.

[91] R. Bube, *Photoconductivity of Solids*, vol. 4. Wiley New York, 1960.

[92] F. Xie, H. Lu, X. Xiu, D. Chen, P. Han, R. Zhang, and Y. Zheng, "Low dark current and internal gain mechanism of gan msm photodetectors fabricated on bulk gan substrate," *Solid-State Electronics*, 2011.

[93] S. Soares, "Photoconductive gain in a schottky barrier photodiode," *Japanese Journal of Applied Physics*, vol. 31, pp. 210–216, 1992.

[94] D. Schroder, *Semiconductor Material and Device Characterization*. Wiley-IEEE press, 2006.

[95] J. Zhao, A. Wang, P. Altermatt, S. Wenham, and M. Green, "24% efficient PERL silicon solar cell: recent improvements in high efficiency silicon cell research," *Solar Energy Materials and Solar Cells*, vol. 41, pp. 87–99, 1996.

[96] A. Luque and A. Martí, "Increasing the efficiency of ideal solar cells by photon induced transitions at intermediate levels," *Physical Review Letters*, vol. 78, no. 26, pp. 5014–5017, 1997.

[97] W. Shockley and H. Queisser, "Detailed balance limit of efficiency of p-n junction solar cells," *Journal of Applied Physics*, vol. 32, no. 3, pp. 510–519, 1961.

[98] A. Martıand A. Luque, "Fundamentals of intermediate band solar cells," *Next Generation of Photovoltaics: New Concepts*, vol. 165, p. 209, 2012.

[99] M. Petroff and M. Stapelbroek, "Blocked impurity band detectors," February 1986. US Patent 4,568,960.

[100] A. Martí, N. López, E. Antolin, E. Canovas, C. Stanley, C. Farmer, L. Cuadra, and A. Luque, "Novel semiconductor solar cell structures: The quantum dot intermediate band solar cell," *Thin Solid Films*, vol. 511, pp. 638–644, 2006.

[101] A. Martí, D. Marrón, and A. Luque, "Evaluation of the efficiency potential of intermediate band solar cells based on thin-film chalcopyrite materials," *Journal of Applied Physics*, vol. 103, p. 073706, 2008.

[102] N. López, L. Reichertz, K. Yu, K. Campman, and W. Walukiewicz, "Engineering the electronic band structure for multiband solar cells," *Physical Review Letters*, vol. 106, no. 2, p. 28701, 2011.

[103] T. Tanaka, K. Yu, A. Levander, O. Dubon, L. Reichertz, N. Lopez, M. Nishio, and W. Walukiewicz, "Demonstration of $ZnTe_{1-x}O_x$ intermediate band solar cell," *Japanese Journal of Applied Physics*, vol. 50, no. 8, p. 2304, 2011.

[104] N. Mott, "Metal-insulator transition," *Reviews of Modern Physics*, vol. 40, pp. 677–683, 1968.

[105] B. Halperin and M. Lax, "Impurity-band tails in the high-density limit. I. minimum counting methods," *Physical Review*, vol. 148, no. 2, p. 722, 1966.

[106] M. Alexander and D. Holcomb, "Semiconductor-to-metal transition in n-type group IV semiconductors," *Reviews of Modern Physics*, vol. 40, no. 4, p. 815, 1968.

[107] J. Heremans, V. Jovovic, E. Toberer, A. Saramat, K. Kurosaki, A. Charoenphakdee, S. Yamanaka, and G. Snyder, "Enhancement of thermoelectric efficiency in PbTe by distortion of the electronic density of states," *Science*, vol. 321, no. 5888, pp. 554–557, 2008.

[108] W. Shockley and W. Read Jr, "Statistics of the recombinations of holes and electrons," *Physical Review*, vol. 87, no. 5, p. 835, 1952.

[109] R. Hall, "Electron-hole recombination in germanium," *Physical Review*, vol. 87, no. 2, p. 387, 1952.

[110] A. Luque, A. Martí, E. Antolín, and C. Tablero, "Intermediate bands versus levels in non-radiative recombination," *Physica B: Condensed Matter*, vol. 382, no. 1, pp. 320–327, 2006.

[111] J. Krich and A. Aspuru-Guzik, "Scaling and localization lengths of a topologically disordered system," *Physical Review Letters*, vol. 106, no. 15, p. 156405, 2011.

[112] P. Dai, Y. Zhang, and M. Sarachik, "Electrical conductivity of metallic Si:B near the metal-insulator transition," *Physical Review B*, vol. 45, no. 8, p. 3984, 1992.

[113] J. Sullivan, R. Wilks, M. Winkler, L. Weinhardt, D. Recht, A. Said, B. Newman, Y. Zhang, M. Blum, S. Krause, W. Yang, C. Heske, M. Aziz, M. Bär, and T. Buonassisi, "Soft X-ray emission spectroscopy studies of the electronic structure of silicon supersaturated with sulfur," *Applied Physics Letters*, vol. 99, no. 14, p. 142102, 2011.

[114] T. Kim, K. Alberi, O. Dubon, M. Aziz, and V. Narayanamurti, "Composition dependence of schottky barrier heights and bandgap energies of GaN_xAs_{1-x} synthesized by ion implantation and pulsed-laser melting," *Journal of Applied Physics*, vol. 104, no. 11, pp. 113722–113722, 2008.

[115] G. Jellison and D. Lowndes, "Measurements of the optical properties of liquid silicon and germanium using nanosecond time-resolved ellipsometry," *Applied Physics Letters*, vol. 51, no. 5, pp. 352–354, 1987.

[116] M. Morita, T. Ohmi, E. Hasegawa, M. Kawakami, and M. Ohwada, "Growth of native oxide on a silicon surface," *Journal of Applied Physics*, vol. 68, no. 3, pp. 1272–1281, 1990.

[117] B. Bob, "Unpublished notes." 2008.

[118] K. Sánchez, I. Aguilera, P. Palacios, and P. Wahnón, "Formation of a reliable intermediate band in Si heavily coimplanted with chalcogens (S, Se, Te) and group III elements (B, Al)," *Physical Review B*, vol. 82, no. 16, p. 165201, 2010.

[119] K. Graff, *Metal Impurities in Silicon-Device Fabrication*. Springer Berlin and New York, 2000.

[120] J. Narayan, "Interface instability and cell formation in ion-implanted and laser-annealed silicon," *Journal of Applied Physics*, vol. 52, no. 3, pp. 1289–1293, 1981.

[121] J. Narayan, "Development of morphological instability and formation of cells in silicon alloys during pulsed laser irradiation," *Journal of Crystal Growth*, vol. 59, no. 3, pp. 583–598, 1982.

[122] A. Cullis, D. Hurle, H. Webber, N. Chew, J. Poate, P. Baeri, and G. Foti, "Growth interface breakdown during laser recrystallization from the melt," *Applied Physics Letters*, vol. 38, no. 8, pp. 642–644, 1981.

[123] D. Hoglund, M. Aziz, S. Stiffler, M. Thompson, J. Tsao, and P. Peercy, "Effect of nonequilibrium interface kinetics on cellular breakdown of planar interfaces during rapid solidification of Si-Sn," *Journal of Crystal Growth*, vol. 109, no. 1-4, pp. 107–112, 1991.

[124] D. Hoglund, M. Thompson, and M. Aziz, "Experimental test of morphological stability theory for a planar interface during rapid solidification," *Physical Review B*, vol. 58, no. 1, p. 189, 1998.

[125] K. Tang, E. Øvrelid, G. Tranell, and M. Tangstad, "Critical assessment of the impurity diffusivities in solid and liquid silicon," *JOM Journal of the Minerals, Metals and Materials Society*, vol. 61, no. 11, pp. 49–55, 2009.

[126] A. Cullis, H. Webber, J. Poate, and A. Simons, "Segregation and increased dopant solubility in pt-implanted and laser-annealed si layers," *Applied Physics Letters*, vol. 36, no. 4, pp. 320–322, 1980.

[127] G. Foti, E. Rimini, W. Tseng, and J. Mayer, "Structure of crystallized layers by laser annealing of< 100> and< 111> self-implanted silicon samples," *Applied Physics A: Materials Science & Processing*, vol. 15, no. 4, pp. 365–369, 1978.

[128] A. Cullis, H. Webber, N. Chew, J. Poate, and P. Baeri, "Transitions to defective crystal and the amorphous state induced in elemental si by laser quenching," *Physical Review Letters*, vol. 49, no. 3, pp. 219–222, 1982.

[129] P. Baeri, J. Poate, S. Campisano, G. Foti, E. Rimini, and A. Cullis, "Dependence of trapping and segregation of indium in silicon on the velocity of the liquid-solid interface," *Applied Physics Letters*, vol. 37, no. 10, pp. 912–914, 1980.

[130] D. Recht, F. Capasso, and M. Aziz, "On the temperature dependence of point-defect-mediated luminescence in silicon," *Applied Physics Letters*, vol. 94, p. 251113, 2009.

[131] S. Pan, D. Recht, S. Charnvanichborikarn, J. Williams, and M. Aziz, "Enhanced visible and near-infrared optical absorption in silicon supersaturated with chalcogens," *Applied Physics Letters*, vol. 98, p. 121913, 2011.

[132] D. Recht, D. Hutchinson, T. Cruson, A. DiFranzo, A. McAllister, A. Said, J. Warrender, P. Persans, and M. Aziz, "Contactless microwave measurements of photoconductivity in silicon hyperdoped with chalcogens," *Applied Physics Express*, vol. 5, no. 4, p. 041301, 2012.

[133] D. Recht, J. Sullivan, R. Reedy, T. Buonassisi, and M. Aziz, "Controlling dopant profiles in hyperdoped silicon by modifying dopant evaporation rates during pulsed laser melting," *Applied Physics Letters*, vol. 100, no. 11, p. 112112, 2012.

Colophon

This thesis was typeset using LaTeX, originally developed by Leslie Lamport and based on Donald Knuth's TeX. The body text is set in 11 point Arno Pro, designed by Robert Slimbach in the style of Venitian and Aldine book types, and issued by Adobe in 2007.
A template that can be used to format a PhD thesis with this look and feel is freely available online at `https://github.com/suchow/`.